



TÉCNICO
LISBOA



POLITECNICO
DI TORINO



Aerothermodynamic Analysis of Aerocapture and Ballistic Entry Flows in Neptune's Atmosphere

João Alexandre Abreu Coelho

Thesis to obtain the Master of Science Degree in

Aerospace Engineering

Supervisors: Prof. Mário António Prazeres Lino da Silva
Prof. Domenic d'Ambrosio

February 2021

"No man is an island, entire of itself; every man is a piece of the continent, a part of the main (...)."

John Donne

Dedicated to my family and friends.

Acknowledgments

I want to thank those who are the most important thing in my life: my family. Mom, Dad, Sister, thank you for all that you have done for me: all the efforts, all the trips, all the calls, all the hugs, all the kisses, all the goodbyes and all the reunions. You made me grow in the best way possible, allowing me to have this opportunity to study what I love. I am so proud of having you, and I hope to make you proud, today and always. I also thank my grandmother Rita who always made sure to present her warm and beautiful smile whenever I returned to the island.

To Professor Mário Lino da Silva, to Duarte Gonçalves, to Beatriz Oliveira and Inês Cardoso, a sincere thank you for all the patience and help throughout these long months. You were always there whenever I needed some answers. It was hard, but without you, it would have been even worse.

To all the friendships born during this academic journey, particularly to Comitiva, but mainly to Pestes: you helped me believe that everything I had heard about the competitiveness in Técnico was untrue. As we learned from day one: We are a team! And thank you for being here, as a team, through these years. It would not have been the same without you.

I would also like to thank everyone from the university's Soccer Team - AEIST, who helped me conciliate the studies' effort, pushing me to organize myself to give the best of me inside and outside the pitch. You were a family, and as heard since the beginning: "From this team, nobody leaves. We only get in."; and is as a part of it I leave this Institute.

A thank you to everyone who accompanied me in the wonderful project that AeroLiga was (and is). It was amazing to bring to our course one of my passions: playing football.

Last but not least, a big thank you to my fellow countrymen from Madeira Island (from Bros da Ilha to Real Madeira), who helped me, making me always feel at home, even being far away from the island we so deeply love.

Thank you to everyone who was a part of this journey.

Resumo

Neptuno é um dos planetas do nosso Sistema Solar que ainda está por explorar, e o ser humano precisa de se preparar para estes novos desafios de engenharia que esta exploração acarreta. Atualmente, muitas são as parecenças assumidas entre as atmosferas de Neptuno e Júpiter; particularmente na composição em hidrogénio e hélio, considerados como os seus principais componentes, em proporções aproximadas de 80%/20%, respetivamente. Contudo, também se sabe que a atmosfera de Neptuno tem uma pequena quantidade de metano (CH_4), com percentagens estimadas à volta de 1.5%.

Este trabalho procura avaliar a influência da composição química exata da atmosfera de Neptuno (incluindo CH_4) no ambiente aerotérmico a que uma cápsula está sujeita aquando a entrada atmosférica neste planeta. São consideradas diferentes formas para a cápsula (60° e 45° *sphere-cones*), e dois pontos de trajetória para dois diferentes tipos de missão são estudados: um ponto de trajetória para entrada atmosférica balística (perto dos 80km de altitude a 18 km/s), e outro ponto de trajetória para uma manobra de aerocaptura (a 130km de altitude a 29 km/s). Para ambas as cápsulas, os diferentes pontos de trajetória e as diferentes composições químicas (com e sem CH_4) são considerados para a análise aerotermodinâmica, incluindo os fluxos de calor convectivos e radiativos ao longo parede da cápsula. Os resultados mostram que, quando a pequena percentagem de metano é considerada, os fluxos radiativos na parede aumentam significativamente, em especial para o ponto de trajetória de entrada balística.

Finalmente, uma pequena análise aerodinâmica é feita para o ponto de trajetória de aerocaptura, avaliando os coeficientes aerodinâmicos para cápsulas com superfícies de controlo (trim-tabs). A cápsula com um *cone angle* $\theta_c = 45^\circ$ parece apresentar uma melhor performance, enquanto que $\theta_c = 60^\circ$ é propícia a apresentar instabilidades aerodinâmicas.

Palavras-chave: Hipersónico, Neptuno, Fluxos de Calor, Aerotermodinâmica, Aerocaptura, Entrada Atmosférica

Abstract

Neptune is one of the Solar system's planets that are still unexplored, and mankind needs to be prepared for these new engineering challenges. For now, a lot of similarities are assumed between the atmospheres of Neptune and Jupiter. Specifically, both planets' main components are believed to be molecular hydrogen and helium (in an approximate proportion of 80%/20%). However, Neptune's atmosphere is also believed to have a small methane's (CH_4) percentage (1.5%).

This work aims to evaluate the exact Neptune chemical composition (including CH_4) influence in the aerothermal environment of a capsule entering this atmosphere. Different capsule's shapes are considered (60° and 45° sphere-cones), and two trajectory points for two different mission types are studied: an ballistic entry trajectory point (around 80km altitude at 18 km/s) and an aerocapture trajectory point (around 130km altitude at 29 km/s). For both capsules, different trajectory points and chemical compositions (with and without CH_4) are considered for the performed aerothermodynamic analysis, including both the convective and the radiative wall heat fluxes through the capsule's wall. The results show that, when the small methane's percentage is considered, the radiative wall heat fluxes increase significantly, particularly for the entry trajectory point.

Finally, a brief aerodynamic analysis is performed for the aerocapture trajectory point, evaluating the aerodynamic coefficients for capsules with trim tabs. The capsule with a cone angle $\theta_c = 45^\circ$ seems to present better performance, whereas $\theta_c = 60^\circ$ is prone to aerodynamic instabilities.

Keywords: Hypersonics, Neptune, Heat Fluxes, Aerothermodynamics, Aerocapture, Atmospheric Ballistic Entry

Declaration

I declare that this document is an original work of my own authorship and that it fulfills all the requirements of the Code of Conduct and Good Practices of the Universidade de Lisboa.

Contents

Acknowledgments	v
Resumo	vii
Abstract	ix
List of Tables	xvii
List of Figures	xix
Nomenclature	xxiii
Acronyms	xxix
Glossary	xxix
1 Introduction	1
1.1 Motivation	1
1.2 Atmospheric Entry Overview	2
1.3 Neptune Mission Overview	4
1.3.1 Mission	4
1.3.2 Aerocapture/Aerobraking	4
1.3.3 Capsule design	6
1.3.4 Trim tab design	7
1.4 Objectives	8
1.5 State of the Art	9
1.6 Thesis Outline	10
2 Governing Equations	11
2.1 Fluid Models	11
2.1.1 Governing Equations	11
2.1.2 Thermodynamic Models	12
2.1.3 Chemical Kinetics	14
2.1.4 Transport Properties	15
2.2 Aerodynamic Forces and Moments	20
2.2.1 Coordinate system	20
2.2.2 Forces and Moments	21
2.3 Radiation	22

2.3.1	Emission and Absorption Coefficients	22
2.3.2	Radiative Energy Transfer	24
3	Numerical Modeling	29
3.1	CFD Solver - SPARK	29
3.2	SPARK Line by Line Code	30
3.2.1	Ray Tracing - Ray Distribution	31
3.3	Trajectory Point	31
3.3.1	Aerocapture Trajectory Point	32
3.3.2	Ballistic atmospheric Entry Trajectory Point	33
3.3.3	Atmosphere	33
3.4	Chemical Model Database	34
3.5	Transport Models Database	34
3.6	Radiation Models Database	35
3.7	Mesh Study	37
3.7.1	Mesh Boundary Conditions	37
3.7.2	Mesh Convergence Study	38
3.7.3	Mesh Refinement	41
3.7.4	Numerical Issues	43
4	Results	45
4.1	Problem Description	45
4.1.1	Test case 1 - Aerothermodynamic analysis of Entry Trajectory Point and Aerocapture Trajectory Point	45
4.1.2	Test case 2 - Aerodynamic analysis of Aerocapture Trajectory Point	46
4.2	Computational framework	46
4.2.1	Computational Domain	47
4.2.2	Ray Tracing Convergence	49
4.3	Run Time Considerations	50
4.3.1	CFD Solver - SPARK	50
4.3.2	Radiative Solver - SPARK LbL	50
4.4	Test Case 1	51
4.4.1	Entry Trajectory Point	51
4.4.2	Aerocapture Trajectory Point	53
4.4.3	Wall Heating	60
4.5	Test Case 2	72
4.5.1	Aerodynamic coefficients	72
5	Conclusions	75
5.1	Achievements	75

5.2 Future Work	76
Bibliography	77
A Forces on the capsule	83
A.1 Pressure Forces	83
A.2 Viscous Forces	86
B Chemical Dataset	89
C Database from NASA's Neptune GRAM	91
D Numerical Problems	93
E Results Aerothermodynamic Analysis	94

List of Tables

1.1	Parametric values for the different capsules	8
2.1	Most common multi-temperature models.	14
2.2	Transport properties.	16
3.1	Aerocapture TP properties used in simulations.	32
3.2	Ballistic atmospheric entry point properties used in simulations.	33
3.3	Chemical compositions.	33
3.4	Species involved for each composition.	34
3.5	Radiative Database.	36
4.1	Test Matrix for Test Case 1.	45
4.2	Test Matrix for Test Case 2.	46
4.3	Convergence Study for Ray Tracing for Stagnation Line - Error compared to 1500 rays case.	49
4.4	Run Time for the Radiative Solver for the different Modules for 50x60 Meshes and 50 rays (worst case scenario).	50
4.5	Comparison with the literature for Entry TP $\theta = 45^\circ$	69
4.6	Comparison with the literature for Aerocapture TP $\theta = 45^\circ$	70
B.1	Chemical Dataset; $K_f = A \cdot T^n \cdot \exp(-\theta_R/T)$ [$\text{cm}^3 \text{mol}^{-1} \text{s}^{-1}$]	89

List of Figures

1.1	Illustration of high-temperature effects along the stagnation streamline for Neptune reentry. Adapted and based on [6–8]	3
1.2	Neptune’s orbit and Kuiper Belt.	4
1.3	Aerobraking and aerocapture.	5
1.4	Ballistic entry vs Lifting Entry.	6
1.5	Dimensions definitions.	7
1.6	The two capsule configurations.	7
1.7	Example of different cant angle configurations for a 60° sphere-cone capsule.	8
1.8	Examples of configurations used ($\eta = 40^\circ$, $\eta = 60^\circ$ and $\eta = 80^\circ$; for $\theta = 60^\circ$ and $\theta = 45^\circ$).	8
1.9	Capsule shapes examples considered by Lockwood <i>et al.</i>	10
2.1	Different energy modes (diatomic molecules case).	12
2.2	Body-fixed (X_B, Y_B, Z_B) and Aerodynamic coordinate system (X_A, Y_A, Z_A).	20
2.3	Elementary radiative processes, from left to right: spontaneous emission, absorption and induced emission.	23
2.4	Tangent-slab model representation.	26
2.5	Rays Representation with 50 rays per hemisphere - Example for $\theta = 45^\circ$.	27
2.6	Representation of Linear Interpolation in the Ray Tracing at a given cell.	28
3.1	Spark LbL Structure with several Modules.	30
3.2	Representation of the generation of Fibonacci lattice points.	31
3.3	Latitude-Longitude lattice vs Fibonacci lattice.	31
3.4	Different regimes and equations/conditions applicable for different K_n .	32
3.5	Mesh boundaries.	37
3.6	Mesh convergence study results for $\theta = 60^\circ$.	39
3.7	Mesh convergence study results for $\theta = 45^\circ$.	40
3.8	Mesh Refinement Example.	41
3.9	Relation of aspect ratio of the cell and probability of carbuncle occurrence according to [52].	43
3.10	Carbuncle representation before and after correction.	44
4.1	Sonic lines and shock line.	47
4.2	Meshes for all cases.	48

4.3	Convergence study on number of rays per hemisphere for Radiative Study - Entry TP for $\theta = 60^\circ$ with CH_4 .	49
4.4	Chemical species along Stagnation Line for Entry TP.	51
4.5	Radiative Power along Stagnation Line for Entry TP.	53
4.6	Stagnation Line Temperature - Entry TP.	53
4.7	Chemical species along Stagnation Line for Aerocapture TP.	54
4.8	Radiative Power along Stagnation Line for Aerocapture TP.	55
4.9	Stagnation Line Temperature - Aerocapture TP.	55
4.10	Comparison based on Trajectory Point - Stagnation Line Temperature.	56
4.11	Abnormal results for Aerocapture TP $\theta = 60^\circ$ (with CH_4).	57
4.12	Sequential distancing of the sonic line from the nose cap towards the shoulder.	59
4.13	Mars Pathfinder Mach field.	59
4.14	Comparison Convective Heat Flux based on Chemical Compositions.	60
4.15	Comparison Convective Heat Flux based on Trajectory Point.	61
4.16	Radiative and Convective Wall Heating for Entry TP.	62
4.17	Radiative and Convective Wall Heating for Aerocapture TP.	62
4.18	Radiative Powers for Entry TP ($\theta = 45^\circ$ with CH_4) - Total and 2 most dominant.	63
4.19	Molar Fraction of C_2 , H_2 and H for Entry TP ($\theta = 45^\circ$) in different chemical compositions.	63
4.20	Spectral Radiative Heating for Entry TP ($\theta = 45^\circ$ with CH_4) - Stagnation Point and Shoulder.	64
4.21	Spectral Radiative Heating for Entry TP ($\theta = 45^\circ$ no CH_4) - Stagnation Point and Shoulder.	64
4.22	Radiative Powers for Aerocapture TP ($\theta = 45^\circ$ with CH_4) - Total and 2 most dominants.	65
4.23	Temperature Fields for $\theta = 45^\circ$ with CH_4 .	65
4.24	Spectral Radiative Heating for Aerocapture TP ($\theta = 45^\circ$ w CH_4) - Stagnation Point and Shoulder.	66
4.25	Spectral Radiative Heating for Aerocapture TP ($\theta = 45^\circ$ no CH_4) - Stagnation Point and Shoulder.	66
4.26	Radiative Model Analysis - Linear Interpolation - $\theta = 45^\circ$ with CH_4 .	67
4.27	Radiative Model influence in Entry TP.	68
4.28	Radiative Model influence in Aerocapture TP.	68
4.29	Chemical evolution in Stagnation Line from Park.	70
4.30	Aerodynamic Coefficients for different Sweep Angles η for zero angle of attack.	72
4.31	Pressure forces projections example.	73
4.32	Aerodynamic efficiency C_L/C_D vs. η .	73
4.33	Pressure distribution computed in CFD vs Modified Newtonian theory (NM).	73
A.1	Pressure Forces.	84
A.2	Disturbed zone on trim tab lateral edge with Mach angle μ .	85
A.3	Trim tab width - distance D	85
A.4	Pressure correction function.	85

A.5	Distances l , \bar{t} and d	85
A.6	Viscous Forces.	86
C.1	Atmospheric properties from NASA's Neptune GRAM and equivalent points for entry trajectory point from ESA's CDF Study data as well as Aerocapture trajectory point.	91
D.1	Cant angle configurations with non physical solutions (Pressure field).	93
E.1	Total Radiative Power Comparison along Stagnation Line based on Chemical Composition.	94
E.2	Total Radiative Power Comparison along Stagnation Line based on Trajectory Point.	94
E.3	Temperature fields for Entry TP.	95
E.4	Temperature fields for Aerocapture TP.	96
E.5	Electron mass fraction fields for Entry TP.	97
E.6	Electron mass fraction fields for Aerocapture TP.	98
E.7	Sonic Line for Entry TP.	99
E.8	Sonic Line for Aerocapture TP.	100
E.9	Sonic Lines for Aerocapture TP Study from §4.4.2.2.	101
E.10	Specific Heat Ratios for Aerocapture TP Study from §4.4.2.2.	102
E.11	Extrapolation values for θ_s from South [55].	103

Nomenclature

Physical Constants

h	Planck's constant	$6.6260702 \times 10^{-34}$ [J s]
k_B	Boltzmann's constant	1.380649×10^{-23} [J K ⁻¹]
N_A	Avogadro's constant	6.022140×10^{23} [mol ⁻¹]
π	Pi number	3.141594... [-]
\mathcal{R}_u	Universal gas constant	8.134459 [J mol ⁻¹ K ⁻¹]

Greek symbols

α	Angle of attack [°]
α_{ij}	Coefficient in Gupta/Yos formulation for interaction (i, j) [-]
β	Angle of side-slip [°]
Δn	Height of first mesh cell at the wall [m]
$\Delta_{ij}^{(1)}$	First collision term for interaction (i, j) [m s]
$\Delta_{ij}^{(2)}$	Second collision term for interaction (i, j) [m s]
η	Flap's sweep angle [°]
ε	Particle energy [J]
ε_J	Energy level [-]
ε_0	Zero-point particle energy [J]
ε_k	Particle energy associated with k^{th} thermal mode [J]
ε_{tot}	Total particle energy [J]
κ	Thermal conductivity coefficient [W m ⁻¹ K ⁻¹]
κ_ν	Spectral absorption coefficient [m ⁻¹ Hz ⁻¹]
κ_k	Thermal conductivity coefficient of k^{th} thermal mode [W m ⁻¹ K ⁻¹]

μ	Dynamic viscosity coefficient [Pa s]
ν	Electromagnetic radiation frequency [Hz]
$\nu''_{s,r}$	Stoichiometric coefficient associated with product s of reaction r [-]
$\nu'_{s,r}$	Stoichiometric coefficient associated with reactant s of reaction r [-]
ν_s	Fundamental vibration frequency of species s [Hz]
$\bar{\nu}$	Electromagnetic radiation wavenumber [cm^{-1}]
$\dot{\Omega}$	Energy-exchange source term [W m^{-3}]
$\dot{\Omega}_k$	Energy-exchange source term associated with thermal mode k [W m^{-3}]
ϕ	Azimuthal angle [$^\circ$]
ϕ_{ul}	Spectral distribution function [Hz^{-1}]
$\pi\bar{\Omega}_{ij}^{(m,n)}$	Average collision cross section (m, n) for interaction (i, j) employed by Gupta <i>et al.</i> [m^2]
ρ	Mass density [kg m^{-3}]
$[\tau]$	Viscous stress tensor [$\text{kg m}^{-1} \text{s}^{-2}$]
τ_ν	Optical thickness to radiation of frequency [-]
τ_e	Characteristic time for energy exchanges [s]
τ_f	Characteristic flow time [s]
τ_{vib}	Vibrational relaxation times [s]
θ	Zenith angle [$^\circ$]
θ_c	Capsule's cone angle [$^\circ$]
θ_R	Reaction characteristic temperature [K]

Roman symbols

a	Speed of sound [m s^{-1}]
A_i	Coefficient for species i in Gupta-Yos formulation [m s kg^{-1}]
a_{av}	Coefficient in Gupta-Yos formulation [m s kg^{-1}]
A_{flap}	Frontal area covered by the flap/trim-tab [m^2]
A_{main}	Frontal area covered by the capsule main body [m^2]
A_{ul}	Einstein coefficient for spontaneous emission [s^{-1}]
A_{ij}^κ	Thermal conductivity coefficient for interaction (i, j) in Gupta-Yos formulation [m s kg^{-1}]

a_{ij}^{κ}	Thermal conductivity coefficient for interaction (i, j) in Gupta-Yos formulation [m s kg ⁻¹]
A_{ij}^{μ}	Viscosity coefficient for interaction (i, j) in Gupta-Yos formulation [m s kg ⁻¹]
a_{ij}^{μ}	Viscosity coefficient for interaction (i, j) in Gupta-Yos formulation [m s kg ⁻¹]
B_{ij}^*	Third collision term for interaction (i, j) [-]
B_{lu}	Einstein coefficient for absorption [m ² J ⁻¹ s ⁻¹]
B_{ul}	Einstein coefficient for induced emission [m ² J ⁻¹ s ⁻¹]
C_D	Drag coefficient [-]
C_F	Force coefficient [-]
C_L	Lift coefficient [-]
C_M	Moment coefficient [-]
c_s	Mass fraction of species s [-]
C_v	Total specific heat at constant volume [J kg ⁻¹ K ⁻¹]
$C_{v,k}$	Specific heat at constant volume associated with k^{th} thermal mode [J kg ⁻¹ K ⁻¹]
D	Diffusion coefficient [m ² s ⁻¹]
D_{ij}	Binary mass diffusion coefficient for pair of species (i, j) [m ² s ⁻¹]
D	Capsule diameter [m]
E	Total internal energy or energy [J]
e	Total specific internal energy [J kg ⁻¹]
e_k	Specific internal energy associated with k^{th} thermal mode [J kg ⁻¹]
E_{ion}	Ionization energy [J]
$e_{k,s}$	Specific internal energy associated with k^{th} thermal mode of individual s species [J kg ⁻¹]
F	Force [N]
g_i	Energy level i degeneracy [-]
h	Total specific enthalpy or height [J kg ⁻¹] or [km]
h_k	Specific enthalpy associated with k^{th} thermal mode [J kg ⁻¹]
$h_{s,k}$	Individual s species' specific enthalpy associated with k^{th} thermal mode [J kg ⁻¹]
h_s	Individual s species' specific enthalpy [J kg ⁻¹]
$I_{\nu}^{\theta,\phi}$	Spectral directional radiative intensity [W m ⁻² sr ⁻¹ Hz ⁻¹]

\mathbf{J}_s	Mass diffusion flux vector of species s [$\text{kg m}^{-2} \text{s}^{-1}$]
j_ν	Spectral emission coefficient [$\text{W m}^{-3} \text{sr}^{-1} \text{Hz}^{-1}$]
$k_{b,r}$	Backwards reaction rate of reaction r [$\text{mol m}^3 \text{s}^{-1}$]
$k_{f,r}$	Forward reaction rate of reaction r [$\text{mol m}^3 \text{s}^{-1}$]
$K_{eq,r}$	Reaction equilibrium constant [-]
l_{flap}	Length of the flap/trim-tab [m]
\mathcal{M}	Molar mass [kg mol^{-1}]
M	Moments [N m]
m_i	Mass of species i [kg]
n	Number of particles [mol]
N_j^*	Boltzmann's population distribution function on J^{th} energy level [-]
p	Pressure [Pa]
\mathbf{q}_C	Convective heat flux vector [W m^{-2}]
\mathbf{q}_D	Diffusive heat flux vector [W m^{-2}]
\mathbf{q}_R	Radiative heat flux vector [W m^{-2}]
\mathbf{Q}	Transformation matrix [-]
\mathbf{q}	Heat flux vector [W m^{-2}]
q_ν	Spectral radiative energy flux [$\text{W m}^{-2} \text{Hz}^{-1}$]
$q_{c,k}$	Convective heat flux of k^{th} thermal mode [W m^{-2}]
r_n	Capsule nose radius [m]
Re	Reynolds number [-]
T	Temperature [K]
t	Time [s]
T_c	Controlling Temperature [K]
T_k	Temperature associated with k^{th} thermal mode [K]
U	Velocity [m s^{-1}]
u, v, w	Velocity Cartesian components
\mathbf{V}	Velocity vector [m s^{-1}]

\dot{w}_s	Mass source term of species s [$\text{kg m}^{-3} \text{s}^{-1}$]
$[X]$	Species' concentration [mol m^{-3}]
$X''_{s,r}$	Product [-]
$X'_{s,r}$	Reactant [-]
X, Y, Z	Cartesian components

Subscripts

∞	Free-stream condition
i, j, k	Computational indexes
n	Normal component
x, y, z	Cartesian components
A	Aerodynamic reference frame
atom	Atomic species
B	Body-fixed reference frame
e	Electron
exc	Electronic excitation mode
i	Species i
ion	Ion
j	Species j
k	k^{th} thermal mode
l	Lower energy level
mol.	Molecular species
ref	Reference condition
r	Reaction
rot	Rotational mode
s	Species s
tra	Translational mode
u	Lower energy level
vib	Vibrational mode

wall or w Conditions on the wall mesh cells

Superscripts

* Adjoint

a Ambipolar correction

P Pressure related property

T Transpose

V Viscous related property

x_s Molar fraction of species s [-]

Acronyms

CCS Collision Cross Section.

CDF Concurrent Design Facility.

CFD Computational Fluid Dynamics.

EAST Electric Arc Shock Tube.

ESA European Space Agency.

IPFN Instituto de Plasmas e Fusão Nuclear.

IST Instituto Superior Técnico.

LAURA Langley Aerothermodynamic Upwind Relaxation Algorithm.

NASA National Aeronautics and Space Administration.

Neptune GRAM Neptune's Global Reference Atmospheric Model.

RMS Root Mean Square.

SPARK Software Package for Aerothermodynamics, Radiation and Kinetics.

SPARK LbL SPARK Line-by-Line.

TP Trajectory Point.

TPS Thermal Protection Systems.

TRL Technology Readiness Level.

Chapter 1

Introduction

This chapter gives some context regarding this thesis subject, specifically an interplanetary mission to Neptune. A simple explanation regarding generic atmospheric entries and aerocapture maneuvers is provided. A small introduction regarding previous works on the heating environment on Neptune's atmosphere is also roughly described.

1.1 Motivation

Since the night of times, mankind has always had the desire to explore and to fulfill its curiosity. In the middle of the past century, we started shooting for the stars, wanting to get to Space. We started with a Space race to the Moon, and these days space exploration is more than just a Spartan race between countries. It is a way to enrich our understanding of the Universe and a tool that allows us to make our lives easier, with Space being present in almost every daily technology and responsible for many of our technological developments.

To learn more about our Solar system, one should know how most of its celestial bodies are made of and how they were formed. The human race has already (indirectly) visited a few asteroids, moons, and planets with this in mind. Many of them were even studied more in depth. However, there are still some doubts about many of our Solar system's celestial bodies, specifically the so-called Ice-Giants: Uranus and Neptune. Visiting them would most likely bring new information about their characteristics, giving us a more in-depth insight into our Solar system as a whole.

It is known that Uranus and Neptune have an atmosphere composed of Helium, Hydrogen, with traces of Methane. Methane is responsible for the planets bluish color since it absorbs light in the wavelength corresponding to the red color in the visible spectrum. Neptune presents a darker blue tone compared to Uranus' greener tone (close to cyan), and the reason for this difference is not entirely known for now [1]. This color difference is just one of many examples of the open questions about these planets. For these reasons, Neptune is already a strong candidate for a joint class-M NASA/ESA mission, aimed for 2030-2040 [2].

Multidisciplinary studies have already been made to assess the feasibility of a mission of this kind.

Some of them consider aerocapture as the most efficient way of putting a spacecraft in a desired closed orbit around this blue planet [2].

1.2 Atmospheric Entry Overview

Due to a planet's strong gravitational well, an object entering through a planetary atmosphere like the one pictured in this work usually does so at very high entry velocities, with freestream Mach numbers well beyond Mach 5. The flow is hypersonic with the gas's internal energy being much smaller compared with its kinetic energy [3].

The dynamics associated with this flight regime are very distinct from those considered in subsonic and supersonic flows. In this case, the flow can reach very high temperatures, allowing several physical-chemical phenomena to occur, such as dissociation and ionization of chemical species, non-equilibrium thermochemistry, and radiative emission due to atomic and molecular de-excitation.

There is some ambiguity regarding Mach number definition at these high speeds, where non-equilibrium phenomena come into play, and this dimension loses some significance as it becomes more common to speak in terms of pure velocities [4].

As will be discussed later, the capsules studied in this work will have a blunt body sphere-cone shape, which produces a near-normal shock at the nose region. This high-drag shape, induces a strong bow-shock wave which will convert the coherent energy of the flow in thermal agitation energy. In turn, some of this agitation energy will be transferred to the species internal modes, leading to the onset of dissociation and ionization reactions.

An advantage of the capsules' blunt-nose geometry is to allow for a certain amount of distance between the hot shock wave and the spacecraft surface, leading to decreased temperature gradients and, minimizing as much as possible the necessary Thermal Protection Systems (TPS).

In this shock layer, endothermic chemical reactions, specifically dissociation reactions, start to occur as the temperature increases, forming a partially ionized plasma around the capsule after the bow shock. All these chemical reactions emit/absorb radiation, a phenomena that may also be of great importance regarding the sizing of the capsule's TPS. We will study how much heat this radiation produces on the wall and if it is essential or not to try to mitigate this phenomenon.

Chemistry model

The Chemistry model in consideration has a freestream composition of 79.75% H_2 , 18.71% He and 1.54% CH_4 . Based on [5, 6], some of the phenomena present on the stagnation line is schematically present in Figure 1.1. More complex phenomena such as pre-ionization upstream of the shockwave, as a result of radiative absorption, is neglected here, as our fluiddynamic and radiative models are uncoupled, as in to what is encountered in the literature. ¹

There is a strong translational, rotational, and vibrational excitation through the shockwave, being

¹Since full fluiddynamic-radiative coupling remains computationally prohibitive to this day.

the latter more intense right after the shock. This excitation leads to dissociation, both for H_2 and CH_4 , generating many H atoms, the most dominant species in the post shock flow. CH_4 first dissociates into CH_3 , then CH_2 , CH, and finally C and H (CH_3 and CH_2 are created and almost immediately destroyed). Electronic excitation also occurs, which usually leads to ionization of H, CH, C and He (the latter in small quantity), generating a so-called entry plasma.

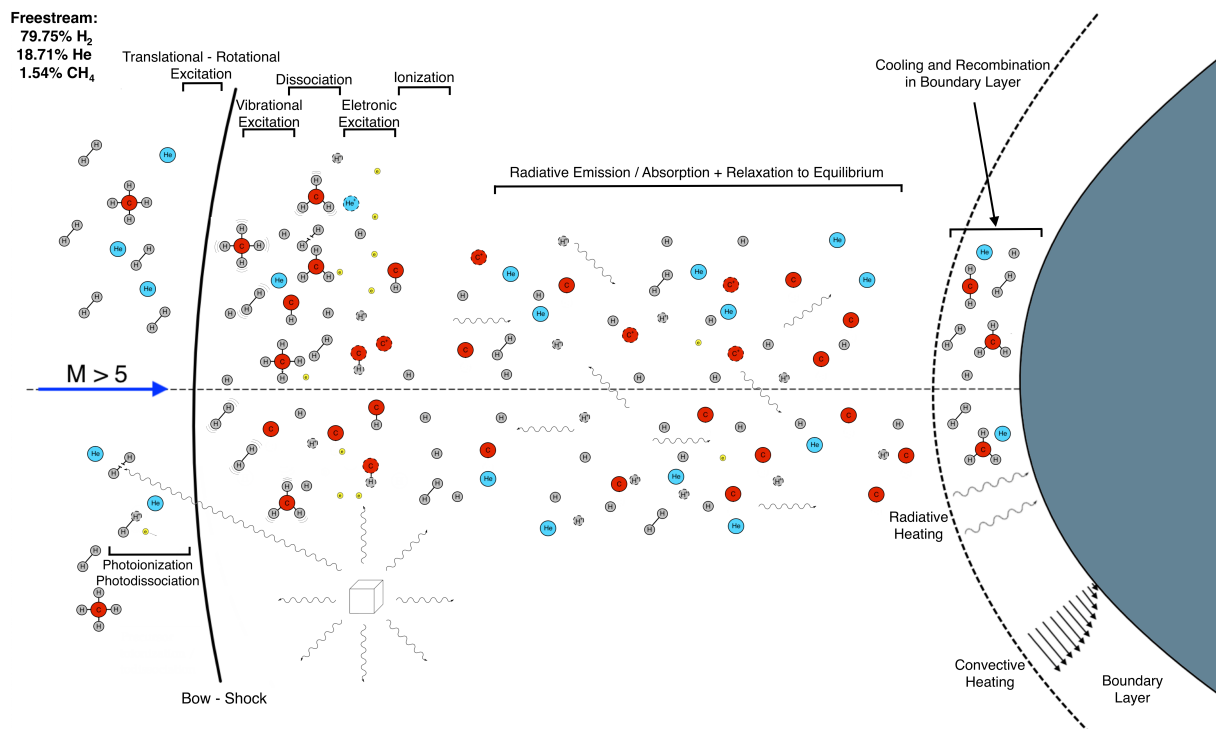


Figure 1.1: Illustration of high-temperature effects along the stagnation streamline for Neptune reentry. Adapted and based on [6–8]

Many chemical reactions change the gas composition until an equilibrium region is eventually established when enough collisional relaxation occurs.

Downstream the equilibrium region, boundary layer and isothermal wall further cools the flow, allowing the recombination of several species. The environment is still severe though, and leads to the TPS erosion phenomena with a formation of an ablation layer of species constituted mostly by carbon. (This phenomenon was omitted from Figure 1.1 as this work will not cover its influence. Check §3.7.1 for more details regarding aforementioned wall catalytic phenomena.)

All the chemical reactions emit/absorb electromagnetic radiation, which will reflect on the radiative heating at the wall. The shock itself is, consequently, a major source/sink for electromagnetic radiation.

More details regarding the radiative phenomena are presented on §2.3.

1.3 Neptune Mission Overview

1.3.1 Mission

Visiting Neptune is a challenging task mainly because of its remote location in the Solar system. Minimum energy trajectories from Earth translate into a flight time of more than 30 years. There are ways to shorten this time, but this increases the entry velocity on Neptune's atmosphere. Reducing the trip time to 12-10 years could be possible and would reflect in entry velocities ranging from 29 to 32 km/s. [9]

As mentioned in [5], Neptune's aerocapture mission would aim to place a spacecraft into an elliptic orbit around Neptune, which would include regular flybys near Triton, one of Neptune's satellites. Since this satellite has a retrograde orbit direction, the entry trajectory would also include a retrograde entry path. This mission was also previously proposed by Jits *et al.* [9] and Hollis *et al.* [10]. Visiting Neptune (and Triton) is of great interest thanks to its proximity to Kuiper Belt, Figure 1.2, which could increase our knowledge regarding the formation of the Solar system and the origin of life.

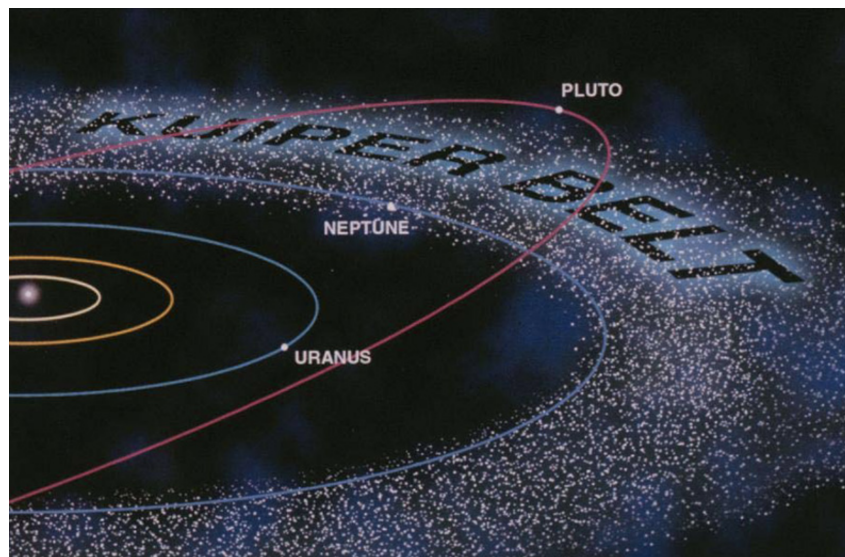


Figure 1.2: Neptune's orbit and Kuiper Belt. [11]

1.3.2 Aerocapture/Aerobraking

The associated orbital maneuvers are not so easy to perform. The main goal is to reduce velocity, transferring the vehicle from an elliptical interplanetary orbit into a new desired orbit (also elliptical) around the planet.

Usually, the necessary ΔV is achieved through reverse propulsion, slowing down the spacecraft. However, this option requires burning/ejecting a significant amount of propellant and is undesirable in terms of mission design.

One may instead take advantage of planetary atmospheres, with the spacecraft skimming their upper layers and being decelerated by aerodynamic drag. This deceleration may be carried out slowly over a

series of passes (aerobraking), or in a steep single maneuver (aerocapture). Both techniques require less fuel than the direct use of any all-propulsive maneuver. Some studies suggest that this type of approach may increase the mission's useful mass by at least 140% [12].

Aerobraking (Figure 1.3a) is performed continuously with several revolutions around the planet. It is safer and requires TPS since the passes are typically done on the upper atmospheric layers, reducing the wall's pressure and heat fluxes. However, this procedure is mostly recommended for orbit adjustments, namely decreasing the apoapsis of an elliptical orbit after the planet's gravity capture the spacecraft. This maneuver is also slowly carried out over long times (up to a few months) requiring constant monitoring from mission control.

Aerocapture (Figure 1.3b) is based on only a one-shot maneuver, with the spacecraft descending deeper into the planet atmosphere with increased drag and aerodynamic heating, but also a very narrow flight corridor, increasing the risk of the mission. Up to this day, only a Lunar return aerocapture maneuver has been (successfully) carried out by the former Soviet Union, and as such the Technology Readiness Level (TRL) for this technique remains very low.

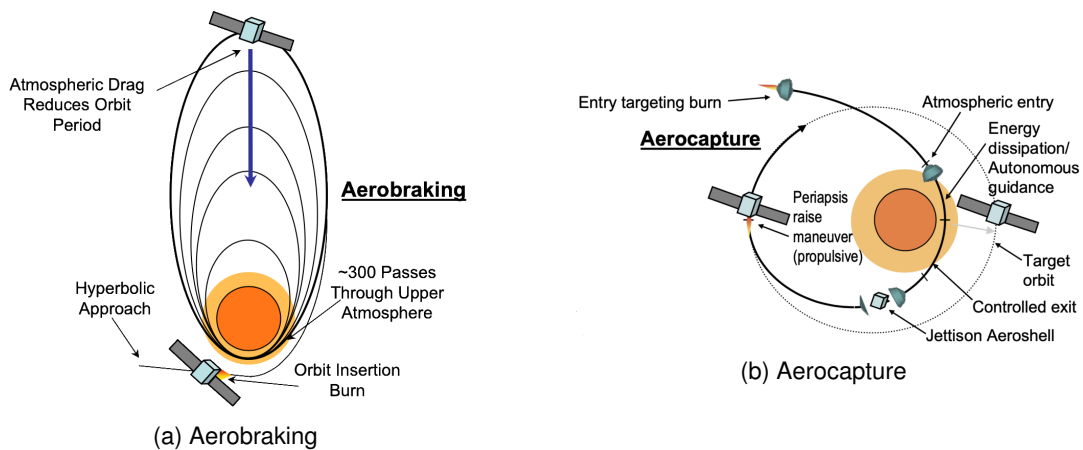


Figure 1.3: Aerobraking and aerocapture. [13]

This type of procedure implies a significant level of active control, and since the distance from the Earth for the information to travel at the speed of light is relatively high, it would not be possible to carry out real-time control. One could try to incorporate automated control algorithms, but this would require excellent computation capabilities, difficult to include on the current generation of on-board computers. In addition to this, the uncertainties of Neptune's atmospheric profile, and the possible presence of storms, makes it even harder to predict what could be encountered during such an aerocapture trajectory. In contrast, aerobraking maneuvers are more attractive, since the atmospheric profiles may be measured and updated in between successive passes. However, the next decade's technological and scientific developments may decrease the uncertainties for this maneuver in the years to come.

1.3.2.1 Aerocapture

For an Aerocapture maneuver, the goal is to decelerate the spacecraft and achieve insertion orbit, instead of a direct ballistic entry. This is performed as a lifting entry, which requires a non-zero angle of

attack (Figure 1.4).

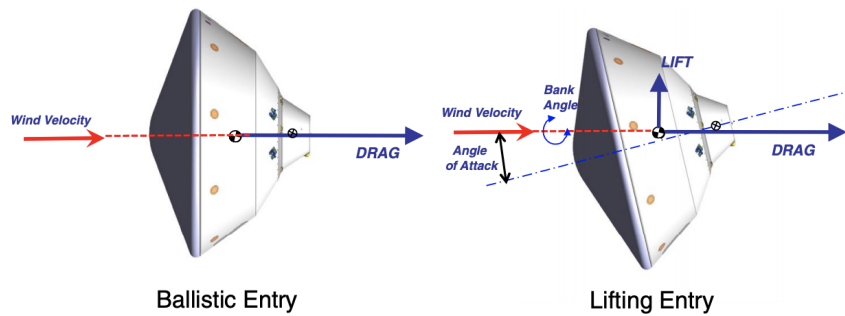


Figure 1.4: Ballistic entry vs Lifting Entry. [14]

This controlled entry may be performed in several different ways:

- Using a **ballast mass** that shifts the center of gravity in a certain way, which in combination with the aerodynamic forces, produces an entry attitude with a non-zero angle of attack, as desired.
- Using **Reaction Control Systems (RCS)** that eject mass in specific directions producing forces and moments that allow the spacecraft to enter with a non-zero angle of attack.
- Using **flaps (trim-tabs)** that distribute aerodynamic forces non symmetrically along with the capsule, shifting the aerodynamic center and allowing the spacecraft to enter with an angle of attack, as desired.

The first two require a considerable amount of extra mass (ballast or propellant mass respectively), reducing the spacecraft useful mass. Even though the flaps also have an associated weight, it is still negligible compared with the previously referred ones. With this approach, useful mass increases in excess of 140% may even be achieved.

In this work, the implementation of trim tabs will be studied to analyze their possible incorporation on the capsule and their efficiency to perform a lifting entry.

1.3.3 Capsule design

Since the first Space missions, the design adopted has been the sphere-cone blunt-body profile for these atmospheric entry missions. The main reason is that this is the shape that maximizes drag, allowing the spacecraft to decelerate as desired. But another important factor is related to wall heating.

Wall heating is inversely proportional to the curvature radius's square root on the stagnation line.

In this work, two capsule configurations will be studied. Both of the capsules will have a blunt-nose conical (sphere-cone) outer model line, similar to the Galileo probe (as suggested on [2]), with two different cone-angles (60° and 45°). As mentioned in [15–17], typical Mars/Earth entry capsules with $60^\circ / 70^\circ$ half-cones are considered whereas 45° capsules are rather favored for gas giants. This work will focus on how these different configurations may affect the flow field, specially regarding wall heating, for this specific mission.

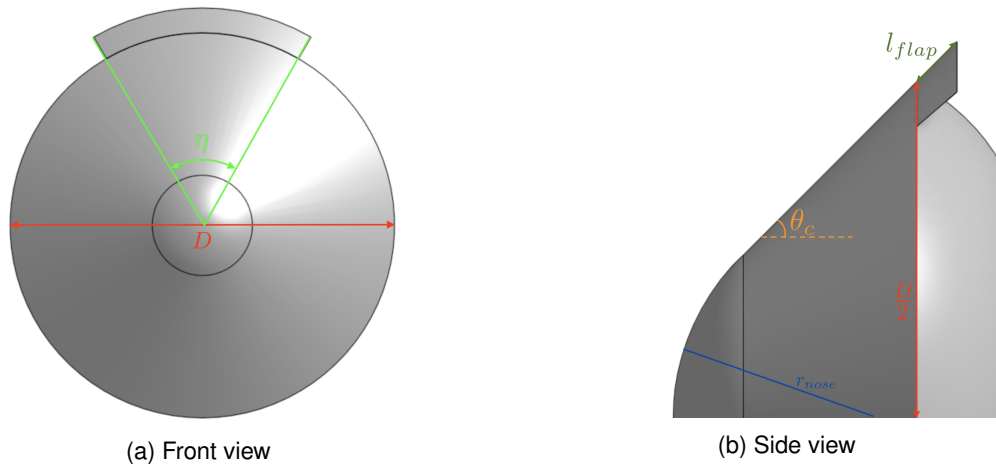


Figure 1.5: Dimensions definitions.

It is also necessary to define additional dimensions to fully freeze capsule geometry, as represented in Figure 1.5. Firstly, a constant frontal area of the main body is defined ². Here, the capsule diameter shall be kept constant to $D = 1.50 m$, slightly similar to the one from [2] ($D = 1.35 m$). The next dimension is the nose radius, r_n . Comparing to the ones reported on [2, 15, 16], ratios of nose radius over diameter of $(\frac{r_n}{D})_{60^\circ} = 0.333$ and $(\frac{r_n}{D})_{45^\circ} = 0.205$ were used respectively $\theta = 60^\circ$ and $\theta = 45^\circ$ configurations.

Both capsules side view are represented in Figure 1.6. The afterbody was not designed accurately and is represented in these figures only for the sake of completeness.

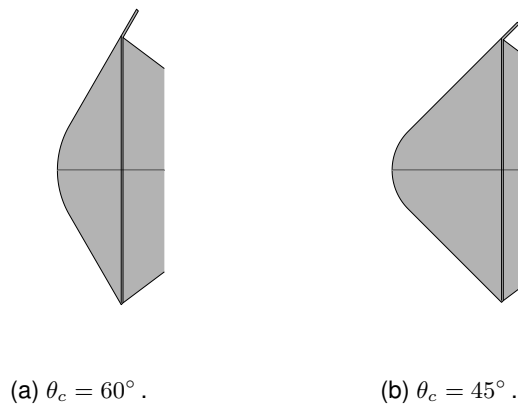


Figure 1.6: The two capsule configurations.

1.3.4 Trim tab design

One of the initial aims for this work was to study the influence of the trim tab cant angle, using several cant angle geometries, like the ones represented in Figure 1.7. However, computational difficulties led us to pursue only solutions with a zero cant angle. This will be addressed later on §3.7.4.1.

²This is constrained by launchers fairing sizes

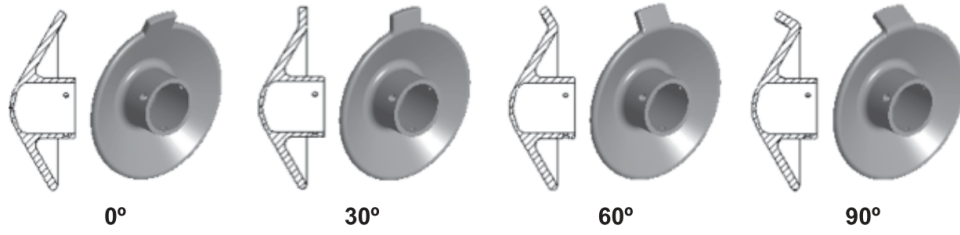


Figure 1.7: Example of different cant angle configurations for a 60° sphere-cone capsule. [18]

For the full design of the full capsule, one must also define the sweep angle of the trim tab η and the ratio between the fraction areas covered by the main body and the trim-tab. The different configurations used to compare these parameters' influence are pictured in Table 1.1 and Figure 1.8.

Table 1.1: Parametric values for the different capsules

θ_c	60°					45°				
D [m]	1.50					1.50				
r_{nose} [m]	$0.333 \cdot D = 0.500$					$0.205 \cdot D = 0.308$				
A_{flap}/A_{main}	5%					5%				
η	40°	50°	60°	70°	80°	40°	50°	60°	70°	80°
l_{flap} [cm]	17.68	14.39	12.14	10.50	9.24	21.66	17.63	14.86	12.85	11.32

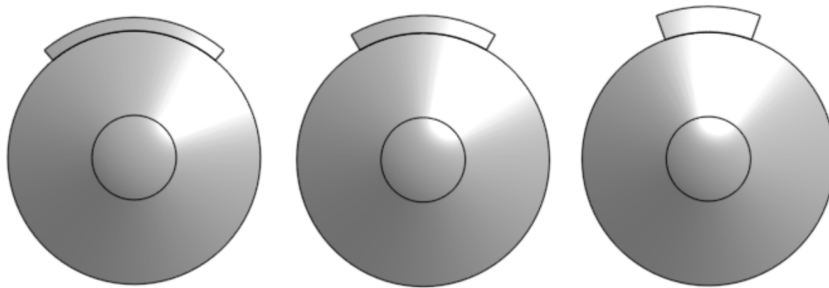


Figure 1.8: Examples of configurations used ($\eta = 40^\circ$, $\eta = 60^\circ$ and $\eta = 80^\circ$; for $\theta = 60^\circ$ and $\theta = 45^\circ$).

1.4 Objectives

This work is divided in two main parts. Firstly, an aerothermodynamic analysis of two trajectory points (Ballistic Entry Trajectory Point (TP) and Aerocapture Trajectory Point (TP)) in Neptune's atmosphere will be done, where the influence of capsule geometry and atmospheric composition will be analyzed in regard to the wall convective and radiative heat fluxes. The obtained data will consider the trajectories defined in ESA's CDF Study and will complement the conclusions therein.

The second part of this thesis will focus on the aerodynamic analysis of both capsule shapes for an aerocapture maneuver: we will analyze the aerodynamic coefficients for Aerocapture TP, examine the

flap's sweep angle influence and analyze which capsule design yields the more favorable aerodynamic coefficients.

1.5 State of the Art

The literature regarding Neptune atmospheric entry remains sparse to this day. Most of the published work is related to Jupiter's entry since there is available data to be compared from the Galileo entry probe which successfully entered Jupiter in 1995. An example of this is legacy is the preliminary studies from ESA's CDF which consider a Galileo-like shape for the capsule and the same atmospheric composition from Jupiter. The influence of the trace components (CH_4) is not accounted for.

Some works do account for a more realistic atmospheric composition. In 2011, Park analyzed the stagnation region of the flow from a blunt body performing an aerocapture in an atmosphere composed of a mixture of 81% H_2 , 17.5 % He , and 1.5 % CH_4 (molar fractions). The aerocapture trajectory point used was based on Hollis *et al.* [10] and Jits *et al.* [9], similar to those presented in the present work. Park considered the flow inviscid (without boundary layer), and focused on an analysis of chemical and radiative processes only for the stagnation line. A few years later, in 2014, Park [6] continued this work, but this time considering viscous phenomena with the presence of a boundary layer.

In this paper, the chemical dataset used considers C_3 and C_2H (neglected in the present work) and neglects the presence of C_2^+ , H_2^+ , He^+ (considered in the present work). Similar to this work, Park neglects the phenomenon of ablation. An assumption of constant pressure is further used, which overestimates the shock standoff distance by nearly 20% for a given nose radius. To correct this overestimation, the nose radius used in the computation is smaller than the actual nose radius, yielding to the correct shock standoff distance.

Hollis *et al.* [10] and Jits *et al.* [9] presented multidisciplinary studies regarding the convective and radiative heating for a Neptune Aerocapture Mission, which focused on topics such as aerothermodynamics, trajectory analysis, atmospheric modeling, aerodynamics, and structural design. In both these papers, although the capsule design is very different from the one used in the present work, there are a few results regarding the heating in the stagnation point which may be useful for comparison. The considered nose radius was 0.3m, which is similar to the 45° capsule from this work (0.308m). The trajectory points considered in these works were gathered for establishing a ground base helping to choose the aerocapture trajectory point used in this thesis.

Finally, in ESA's Concurrent Design Facility, yields a baseline analysis for a ballistic entry trajectory.

Even though different capsule shapes are suggested in the literature for aerocapture missions, this work only analyzed the sphere-cone configuration to simultaneously make an analysis to both aerocapture and atmospheric entry trajectory points. Figure 1.9 shows different configurations suggested in [12] for an aerocapture mission analysis for a Neptune mission.

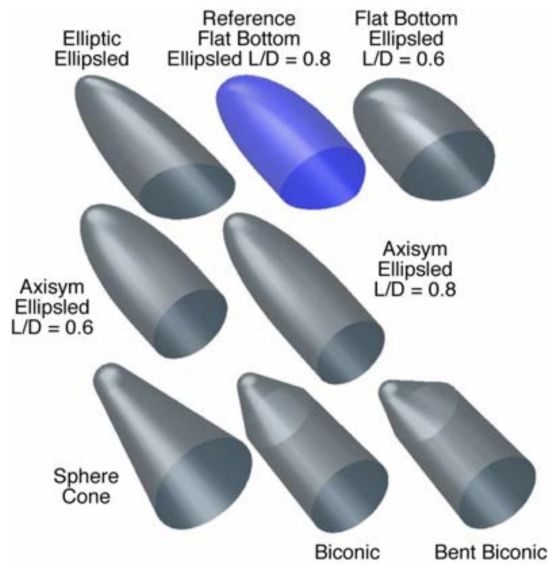


Figure 1.9: Capsule shapes examples considered by Lockwood *et al.* [12].

1.6 Thesis Outline

This document is separated in five main chapters:

The current chapter introduced some baseline concepts for Neptune missions, namely aerothermodynamics, and the fundamentals for aerobraking/aerocapture maneuvers. The baseline geometric configurations for the capsules of this study are also provided.

Chapter 2 presents the physical-chemical models applicable to this kind of hypersonic flows, including fluid dynamics, thermodynamics, chemistry and radiation. A brief explanation on how the flow produces the forces along the capsule and how the aerodynamic coefficients are computed. Finally some details on radiative heat transfer are briefly presented.

Chapter 3 discusses the numerical implementation of the models presented in Chapter 2, alongside with a presentation of the numerical codes and simulation strategies deployed in this work.

Chapter 4 presents the numerical results followed by a discussion of their relevance. The verification of the accuracy of the obtained results is discussed alongside with a comparison with the somewhat limited data available from the literature.

Chapter 5 concludes this work with a brief summary of this work's main findings and achievements, their impact on capsule geometry design and recommendations for future numerical simulations and experiments for cross-checking the conclusions.

Chapter 2

Governing Equations

This chapter presents the theoretical framework for superorbital entry flows characteristic of a Neptune ballistic entry/aerocapture, and discusses their associated high-temperature and non-equilibrium phenomena.

The governing fluid equations, in the framework of a high-temperature, non-equilibrium chemically reacting flow, are firstly presented. A discussion of the resulting aerodynamic forces follows, and the chapter concludes with some details on radiative heat transfer phenomena, which is a consequence of the high temperature effects.

2.1 Fluid Models

2.1.1 Governing Equations

Under the assumption of the continuum flow regime, applying the equation of continuity to the conserved quantities of the flow yields the so-called Navier-Stokes equations.

Conserved quantities are mass, momentum, and energy. When thermal non-equilibrium is at play, an additional conservation equation must be accounted for, regarding the internal energy mode(s).

Mass (for each species), momentum and energy conservation equations are here presented:

$$\frac{\partial(\rho c_s)}{\partial t} + \nabla \cdot (\rho c_s \mathbf{V}) = \nabla \cdot \mathbf{J}_s + \dot{w}_s \quad (2.1a)$$

$$\frac{\partial(\rho \mathbf{V})}{\partial t} + \nabla \cdot (\rho \mathbf{V} \otimes \mathbf{V}) = \nabla \cdot [\boldsymbol{\tau}] - \nabla p \quad (2.1b)$$

$$\frac{\partial(\rho e)}{\partial t} + \nabla \cdot (\rho \mathbf{V} e) = \nabla \cdot (\mathbf{V} \cdot [\boldsymbol{\tau}]) - \nabla \cdot (p \mathbf{V}) - \nabla \cdot \mathbf{q} \quad , \quad (2.1c)$$

with the heat flux vector being a sum of diffusive heat, convective heat and radiative heat.

$$\begin{aligned}\mathbf{q} &= \mathbf{q}_D + \mathbf{q}_C + \mathbf{q}_R \\ &= \sum_s \mathbf{J}_s h_s - \sum_k \kappa_k \nabla T_k + \mathbf{q}_R\end{aligned}$$

For each non-equilibrium thermal mode the addition of an equation reads:

$$\frac{\partial(\rho e_k)}{\partial t} + \nabla \cdot (\rho \mathbf{V} h_k) = \nabla \cdot \left(-\kappa_k \nabla T_k + \sum_s \mathbf{J}_s h_{s,k} \right) + \dot{\Omega}_k \quad (2.1d)$$

In these equations (2.1a - 2.1d) ρ is density, c_s is the species' mass fraction, \mathbf{V} is the velocity vector, \mathbf{J}_s is the mass diffusion flux vector, \dot{w}_s is the source term for production or destruction of the species s , $[\boldsymbol{\tau}]$ is the viscous stress tensor, p is the pressure, e is the specific mixture's internal energy, κ_k and T_k are the thermal conductivity and temperature associated with the k thermal mode, h_s is the species' enthalpy, \mathbf{q}_R is the radiative heat flux vector, and, finally, e_k and $\dot{\Omega}_k$ are the internal energy and energy-exchange source term of the k thermal energy mode.

2.1.2 Thermodynamic Models

High-temperature, non-equilibrium reactive flows need detailed thermodynamic models that accounts for the flow species internal structure as a quantum level.

Particles (atoms, molecules, ions, and electrons) may store energy in different degrees of freedom. The so-called energy modes are represented in Figure 2.1. These differ depending on the species type (atomic, diatomic, polyatomic, or electron).

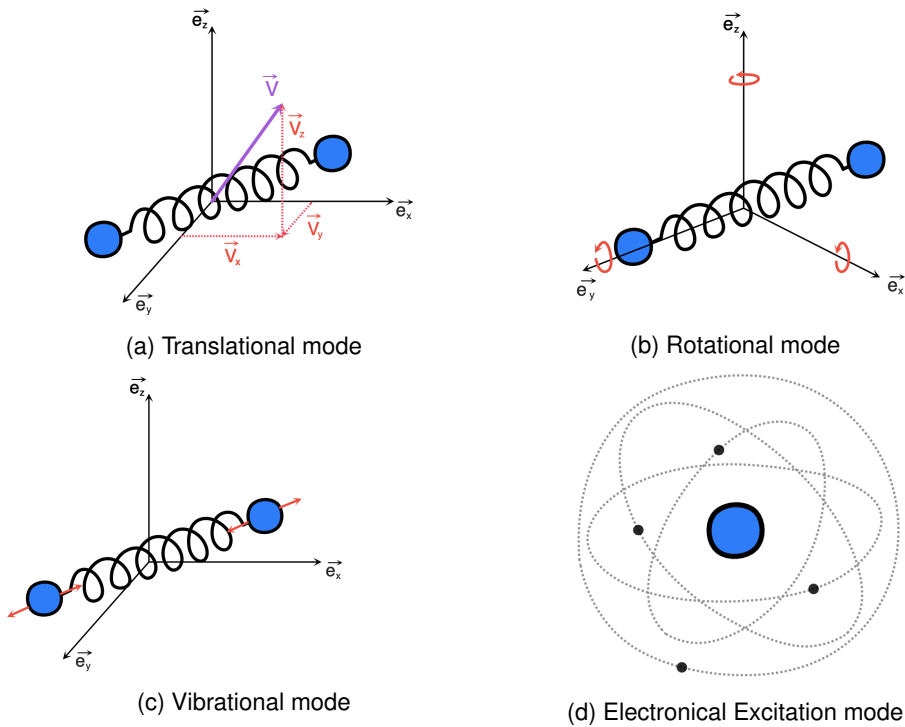


Figure 2.1: Different energy modes (diatomic molecules case).

Atoms may only store energy on translational and electric modes, while molecules may store energy in all four forms of thermal energy modes ($\varepsilon_{rot} = \varepsilon_{vib} = 0$).

Depending on the geometry of the species, the rotational and vibrational degrees of freedom can differ. For example, diatomic and linear polyatomic molecules only possess two degrees of freedom on the rotational modes.

Lastly, free electrons only have the translational degree of freedom.

Summarily, the total energy stored in a particle may be represented as:

$$\varepsilon_{tot} = \varepsilon_{tra} + \varepsilon_{rot} + \varepsilon_{vib} + \varepsilon_{exc} + \varepsilon_0 \quad (2.2)$$

Where ε_k is the energy associated with each thermal mode and ε_0 is the zero-point energy of the species.

For a gas composed by a mixture of different chemical species, each species internal energy level is populated accordingly to a given distribution. Having the same energy level does not imply having the same microscopic arrangement, as different states arrangements can result in the same energy level ¹.

Macroscopically, one may add the contributions of all energy levels over the population distribution, obtaining the internal energy of a single-species:

$$E = \sum_J \varepsilon_J N_J^*(\varepsilon_J) \quad (2.3)$$

The population distribution N_J^* itself depends on the energy levels ε_J which makes this sum not so easy to obtain.

Nevertheless, one may sum the different energy modes of each species, so that the internal energy of a single species is obtained:

$$e_s = \varepsilon_{tra,s} + \varepsilon_{rot,s} + \varepsilon_{vib,s} + \varepsilon_{exc,s} + \varepsilon_{0,s} \quad (2.4)$$

2.1.2.1 Thermodynamic Non-Equilibrium

When the population of the intended degree of freedom follows a Boltzmann Distribution, the gas is considered to be in equilibrium, and all energy modes temperature characteristics are identical $T_k = T$ for all k^{th} mode.

For a reacting flow, the equilibrium state is not achieved instantly, and some areas of the flow experience thermal non-equilibrium. The equilibrium is then achieved through the collisions and radiative energy exchange processes taken place at the microscopic level. This usually takes place over a so-called relaxation time represented by τ_e . If τ_e is much greater than the flow characteristic time τ_f , the flow region is considered in non-equilibrium since the flow that crosses the domain does not have enough time to perform the required energy exchanges to achieve equilibrium. This is typical the case in the region of the shock layer.

¹This phenomenon is described as degeneracy.

For a reacting, non-equilibrium flow, each species s may have its set of internal temperatures $T_{k,s}$.

The different temperatures for each mode can be described using different Multi-temperatures approaches. The most common ones are the so-called 2T and 3T Model, and are presented in Table 2.1.

The two temperature (2T) model, first proposed by Park [19], assumes an equilibrium between the molecules' translational and rotational modes, at a single temperature $T_{tra-rot}$. That is a plausible assumption since these two modes are the ones that require fewer collisions to achieve equilibrium. The molecular vibrational, electron translational, and electronic excitation energies are then lumped at equilibrium at a temperature $T_{vib-exc}$ under the assumption that the energy exchange between the free electrons, the heavy particles' vibrational motion, and the bounded electrons in the electronic levels of atoms and molecules are very efficient.

The three temperature (3T) model is an extension of the 2T model and considers the equilibrium of the electrons' translational energy mode and vibrational modes separately. There are different approaches to this model, depending on the assumption of the equivalence of the two modes at equilibrium (either being the vibrational and electronic excitation of heavy molecules at equilibrium, $T_{vib-exc}$, or being the translational mode of electrons and electronic excitation of molecules at equilibrium at a temperature T_e).

Table 2.1: Most common multi-temperature models.

Model	Energy mode				
	Translational		Rotational	Vibrational	Electronic Excitation
	(e ⁻)	(heavy)	(molecule)	(molecule)	(heavy)
1T (Equilibrium) Model	T	T	T	T	T
2T Model	$T_{vib-exc}$	$T_{tra-rot}$	$T_{tra-rot}$	$T_{vib-exc}$	$T_{vib-exc}$
3T Model	T_e	$T_{tra-rot}$	$T_{tra-rot}$	$T_{vib-exc}$	$T_{vib-exc}$
	T_e	$T_{tra-rot}$	$T_{tra-rot}$	T_{vib}	T_e

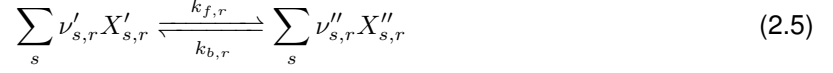
At a higher level on complexity, state-to-state models consider each internal energy level as an individual pseudo-species, capturing individual non-Boltzmann distributions for the different thermal energy modes. Although being considered state-of-the-art, this model is overly complex. As the complexity increases, the computational effort also increases, and furthermore such models may not be physically relevant except in some specific situations.

2.1.3 Chemical Kinetics

Chemical reactions may be in balance when the gas does not present any abrupt change in its chemical composition and may be described by two thermodynamic properties, such as density, pressure, or temperature. When there are changes in the pressure or temperature field, like the ones presented in shock layers, the chemical equilibrium properties change, promoting the reactions that seek this new equilibrium through molecular collisions. Hypersonic flows have low characteristic flow times $\tau_f \ll \tau_e$

not allowing the mixture to reach the equilibrium, leading to a region within the shock layer which is in a chemical non-equilibrium even at a steady state.

Since the mixture is not in equilibrium, the gas state variables are not enough to model the gas, and finite chemistry models need to be added. To do so, one must solve the mass conservation equation for each species present in the mixture. The reactions must be appropriately modeled to find the source term in the mass conservation equation. A general chemical reaction r is given as:



where $\nu'_{s,r}$ and $\nu''_{s,r}$ represent the stoichiometric coefficients of the reactants ($X'_{s,r}$) and products ($X''_{s,r}$) respectively, $k_{f,r}$ and $k_{b,r}$ represent the rate constant for the forward and backward process respectively. The net rate of formation of a species s involved in the reaction r is given by

$$\left\{ \frac{d[X_s]}{dt} \right\}_r = (\nu''_{s,r} - \nu'_{s,r}) \left\{ k_{f,r} \prod_s [X_s]^{\nu'_{s,r}} - k_{b,r} \prod_s [X_s]^{\nu''_{s,r}} \right\} \quad (2.6)$$

Considering all reactions, the net rate of formation of a species s is given by

$$\frac{d[X_s]}{dt} = \sum_r \left\{ \frac{d[X_s]}{dt} \right\}_r \quad (2.7)$$

where $[X_s]$ represents the number of moles of species s per unit of volume of the mixture.

Using the relation above, the forward rate $k_{f,r}$, the backward rate can be calculated

$$\frac{k_{f,r}}{k_{b,r}} = K_{eq,r} \quad (2.8)$$

where $K_{eq,r}$ is the equilibrium constant for concentrations for the reaction r that may be calculated from statistical thermodynamics.

Finally, the mass source term present in (2.1a) is

$$\dot{w}_s = \mathcal{M}_s \frac{d[X_s]}{dt} \quad (2.9)$$

where \mathcal{M}_s represents the molar mass of the species.

2.1.4 Transport Properties

Solving Equations (2.1a) - (2.1d) require the computation of diffusion, viscosity, and thermal conduction. These fluxes are fundamental when modeling the mass, momentum, and energy fluxes due to concentration, velocity, and temperature gradients, respectively. They are explicitly present on the Navier-Stokes equations through the mass diffusion flux vector \mathbf{J}_s , the viscous stress tensor $[\tau]$ and the conduction heat flux associated with each thermal mode $\mathbf{q}_{c,k} = \kappa_k \nabla T_k$.

There are several models to calculate these properties. All of them are a function of the respective property gradient and are depicted in Table 2.2.

Table 2.2: Transport properties.

Dissipative Flux	Symbol	SI Units	Expression	Transport Coefficient	Gradient	Model
Mass Diffusion	J_s	m^2s^{-1}	$J_s = \rho D \nabla c_s$	D	∇c_s	Fick's Law
Moment Diffusion	$[\tau]$	$\text{kg m}^{-1}\text{s}^{-1}$	$[\tau] = \mu (\nabla \mathbf{V} + (\nabla \mathbf{V})^T) - 3/2 \cdot \mu (\nabla \mathbf{V})[I]$	μ	$\nabla \mathbf{V}$	Newtonian Fluid
Heat Conduction	$q_{c,k}$	$\text{J m}^{-1}\text{s}^{-1}\text{K}^{-1}$	$q_{c,k} = \kappa_k \nabla T_k$	κ_k	∇T_k	Fourier's Law

Depending on the transport model used, different ways are used to compute the transport coefficients. SPARK can compute these properties in several different mixing rules, and in §2.1.4.1 different models will be outlined.

2.1.4.1 Transport Models

Wilke/Blottner/Eucken Model

This model dated back to the '50s and was firstly proposed by Wilke. It is an application of kinetic theory to the first order Chapman-Enskog solution [20], combined with curve fits proposed by Blottner *et al.* in [21] for the species viscosities and Eucken's relation [22] for each species' thermal conductivity. This model assumes that all binary interactions have the same cross-section (based on hard-sphere geometry). Wilke's model computes the viscosity and thermal conductivity from a generic expression as a function of mole fractions and each species' viscosity and thermal conductivity [20]. However, this work does not rely on this model since it is not recommended for super-orbital entry regimes as the ones presented in this work [23, 24]. For this reason no further details will be given regarding this model, yet these can be found in [20, 21].

Gupta-Yos/Collision Cross Section Model

This model, first implemented by Gupta *et al.* [25], is a simplification of the Chapman-Enskog solution and provides the transport properties for using an approximate mixing rule. For this calculation, the cross-section for each collision in the multi-component gas mixture is taken into account which makes it more physically accurate than Wilke's model, which considers this cross-section to be constant to all interactions.

The transport coefficients appear as function of the collision terms $\Delta_{ij}^{(1)}$ and $\Delta_{ij}^{(2)}$, defined as

$$\Delta_{ij}^{(1)} = \frac{8}{3} \left[\frac{2\mathcal{M}_i\mathcal{M}_j}{\pi\mathcal{R}_u T_c(\mathcal{M}_i + \mathcal{M}_j)} \right]^{\frac{1}{2}} \pi\bar{\Omega}_{ij}^{(1,1)}$$

$$\Delta_{ij}^{(2)} = \frac{16}{5} \left[\frac{2\mathcal{M}_i\mathcal{M}_j}{\pi\mathcal{R}_u T_c(\mathcal{M}_i + \mathcal{M}_j)} \right]^{\frac{1}{2}} \pi\bar{\Omega}_{ij}^{(2,2)}$$

where \mathcal{R}_u is the universal gas constant. These expressions define the collision strength between each pair of species (i,j) as a function of the controlling temperature T_c which is taken to be electrons' translational temperature T_e - if the interaction involves an electron, or the heavy species' translational temperature T_{tra} otherwise. Finally, $\pi\bar{\Omega}_{ij}$ represents the average collision cross section in m^2 computed using Gupta's curve fits [25].

This model is divided into two main categories, the more common model - 1st Order Model, and the more accurate model proposed by Yos - referred as 2nd Order Model (even though it relies on the same first order Chapman-Enskog approximation).

- 1st Order Model

For the 1st Order Model, the mixture's viscosity is computed as

$$\mu = \sum_i \frac{x_i m_i}{\sum_j x_j \Delta_{ij}^{(2)}} \quad (2.10)$$

with m_i being the particle mass of the species i , obtained with

$$m_i = \frac{\mathcal{M}_i}{N_A} \quad (2.11)$$

where N_A is the Avogadro constant.

The translational mode and electron's thermal conductivities, κ_{ktra} and κ_{ke} , respectively, are computed as

$$\kappa_{ktra} = \frac{15}{4} k_B \sum_{i \neq e} \frac{x_i}{\sum_j \alpha_{ij} x_j \Delta_{ij}^{(2)}} \quad \text{and} \quad \kappa_{ke} = \frac{15}{4} k_B \sum_{i \neq e} \frac{x_e}{\sum_j \alpha_{ej} x_j \Delta_{ej}^{(2)}} \quad (2.12)$$

with α_{ij} being a coefficient function of the species molar masses:

$$\alpha_{ij} = 1 + \frac{\left(1 - \frac{\mathcal{M}_i}{\mathcal{M}_j}\right) \left[0.45 - 2.54 \frac{\mathcal{M}_i}{\mathcal{M}_j}\right]}{\left(1 - \frac{\mathcal{M}_i}{\mathcal{M}_j}\right)^2} \quad (2.13)$$

- 2nd Order Model

This model proposed by Yos [26] is more computationally expensive, although physically more accurate. The model computes the viscosity and translational thermal conductivity using:

$$[\mu \text{ OR } \kappa_{tra}] = \frac{\sum_i \frac{x_i}{A_i + a_{av}}}{1 - a_{av} \sum_i \frac{x_i}{A_i + a_{av}}} \quad (2.14)$$

with a_{av} being an average of the non diagonal matrix allowing to find the solution of the Chapman-Enskog, defined as

$$a_{av} = \frac{\sum_i \sum_j x_i x_j \left(\frac{1}{A_i} - \frac{1}{A_j} \right)^2 a_{ij}}{\sum_i \sum_j x_i x_j \left(\frac{1}{A_i} - \frac{1}{A_j} \right)^2} \quad (2.15)$$

The coefficients A_i and A_j computed from

$$A_i = \sum_j x_j A_{ij} \quad (2.16)$$

and A_{ij} and a_{ij} are defined differently for the computation of viscosity or translational thermal conductivity.

– For the viscosity terms:

$$a_{ij}^\mu = \frac{N_A}{\mathcal{M}_i + \mathcal{M}_j} \left[2\Delta_{ij}^{(1)} - \Delta_{ij}^{(2)} \right] \quad (2.17)$$

$$A_{ij}^\mu = \frac{N_A}{\mathcal{M}_i} \Delta_{ij}^{(2)} \quad (2.18)$$

– For the translational thermal conductivity

$$a_{ij}^\kappa = \left(\frac{2}{15k_B} \right) \frac{\mathcal{M}_i \mathcal{M}_j}{(\mathcal{M}_i + \mathcal{M}_j)^2} \left\{ \left(\frac{33}{2} - \frac{18}{5} B_{ij}^* \right) \Delta_{ij}^{(1)} - 4\Delta_{ij}^{(2)} \right\} \quad (2.19)$$

$$A_{ij}^\kappa = \frac{2}{15k_B (\mathcal{M}_i + \mathcal{M}_j)^2} \left\{ 8\mathcal{M}_i \mathcal{M}_j \Delta_{ij}^{(2)} + (\mathcal{M}_i - \mathcal{M}_j) \left[9\mathcal{M}_i - \frac{15}{2} \mathcal{M}_i + \frac{18}{5} B_{ij}^* \mathcal{M}_j \right] \Delta_{ij}^{(1)} \right\} \quad (2.20)$$

with

$$B_{ij}^* = \frac{5\bar{\Omega}_{ij}^{(1,2)} - 4\bar{\Omega}_{ij}^{(1,3)}}{\bar{\Omega}_{ij}^{(1,1)}} \quad (2.21)$$

For the remaining energy modes, the thermal conductivities are computed as

$$\kappa_{rot} = \sum_{i=\text{mol.}} \frac{x_i m_i C_{vrot,i}}{\sum_i x_i \Delta_{ij}^{(1)}} \quad (2.22)$$

$$\kappa_{vib} = \sum_{i=\text{mol.}} \frac{x_i m_i C_{vvib,i}}{\sum_i x_i \Delta_{ij}^{(1)}} \quad (2.23)$$

$$\kappa_{exc} = \sum_{i=e^-} \frac{x_i m_i C_{vel,i}}{\sum_i x_i \Delta_{ij}^{(1)}} \quad (2.24)$$

The total thermal conductivity in thermal equilibrium is the sum of all contributions:

$$\kappa = \kappa_{tra} + \kappa_{rot} + \kappa_{vib} + \kappa_{exc} \quad (2.25)$$

If the gas is in thermal non-equilibrium, each component κ_k is obtained from every species' individual contributions in the equations above.

Finally, the mixture diffusion coefficient is given by

$$\mathcal{D} = \frac{1 - x_i}{\sum_{j \neq i} \frac{x_j}{D_{ij}}} \quad (2.26)$$

with D_{ij} being the binary diffusion coefficient involving two particles:

$$D_{ij} = \frac{k_B T_c}{p \Delta_{ij}^{(1)}} \quad (2.27)$$

In this Gupta's model, the viscosity coefficient for a **single individual species** is determined as

$$\mu_i = \frac{5}{16} \frac{\sqrt{\pi m_i k_B T_c}}{\pi \bar{\Omega}_{ii}^{(2,2)}} \quad (2.28)$$

and the thermal conductivities for **single individual species** are given by

$$\kappa_{ktra,i} = \frac{75}{64} k_B \frac{\sqrt{\pi k_B T_c / m_i}}{\pi \bar{\Omega}_{ii}^{(2,2)}} \quad (2.29)$$

$$\kappa_{krot,i=\text{mol.}} = \frac{8}{3} k_B c_{vrot,i} \frac{\sqrt{\pi k_B T_c m_i}}{\pi \bar{\Omega}_{ii}^{(1,1)}} \quad (2.30)$$

$$\kappa_{kvib,i=\text{mol.}} = \frac{8}{3} k_B c_{vvib,i} \frac{\sqrt{\pi k_B T_c m_i}}{\pi \bar{\Omega}_{ii}^{(1,1)}} \quad (2.31)$$

$$\kappa_{kexc,i=e^-} = \frac{8}{3} k_B c_{vexc,i} \frac{\sqrt{\pi k_B T_c m_i}}{\pi \bar{\Omega}_{ii}^{(1,1)}} \quad (2.32)$$

Ambipolar Diffusion

There is also an influence of the electric field present in plasmas, contributing to the mass diffusion fluxes [27]. This contribution is particularly important in ions since the more mobile electrons pull these ions. Consequently, these electrons are also slowed down by the ions. Since the conservation equations referred along this section do not account for these electrostatic forces, there is a possible correction to the diffusion mass fluxes of ions - the ambipolar diffusion corrections.

The expressions for this correction (the superscript a represents the corrected diffusion coefficient) are given:

- For ions, proposed by Chen [28]:

$$D_{ion}^a = \left(1 - \frac{T_e}{T_{ion}} \right) D_{ion} \quad (2.33)$$

where D_{ion} is the non-corrected diffusion flux of the ion, and T_e and T_{ion} are the translational temperatures of the electrons and ions, respectively. Note that in thermal equilibrium conditions, $T_e = T_{ion}$, $D_{ion}^a = 2D_{ion}$.

- For electrons, proposed by Lee [29]

$$\mathcal{D}_e^a = \mathcal{M}_e \frac{\sum_{i=\text{ion}} \mathcal{D}_i^a x_i}{\sum_{i=\text{ion}} \mathcal{M}_i x_i} \quad (2.34)$$

Which results in $\mathcal{D}_e^a = \mathcal{D}_i^a$ when there is only one species present.

2.2 Aerodynamic Forces and Moments

2.2.1 Coordinate system

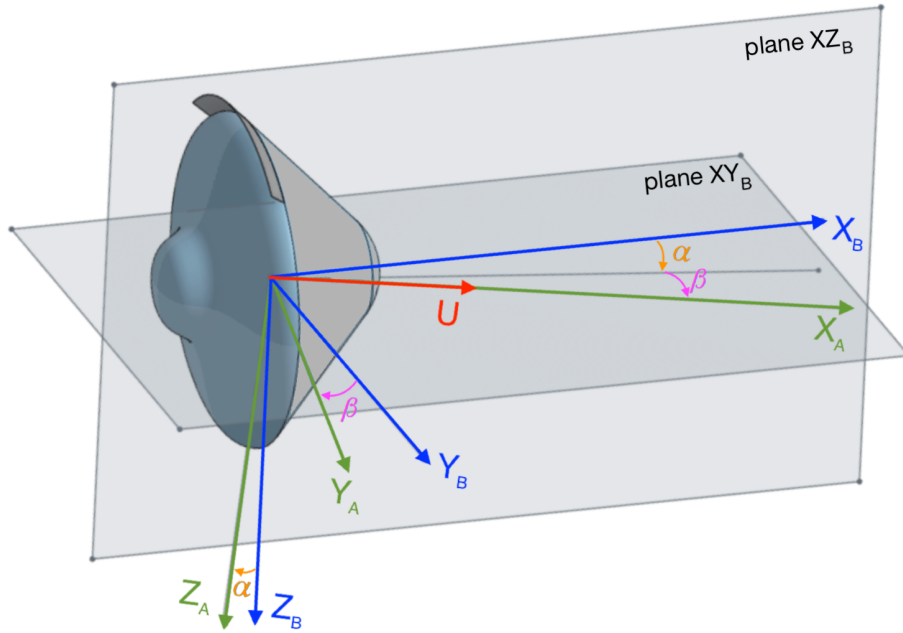


Figure 2.2: Body-fixed (X_B, Y_B, Z_B) and Aerodynamic coordinate system (X_A, Y_A, Z_A).

Forces, moments and velocities are examples of coordinate system dependent properties. Therefore, one must firstly define the coordinate systems. In cases like the one described in this work, two different coordinate systems are usually used: body-fixed (X_B, Y_B, Z_B) and aerodynamic coordinate systems (X_A, Y_A, Z_A). These are schematically reported in Figure 2.2.

These two coordinate systems differ in regard of two particular angles: angle of attack (α , positive nose up), and sideslip angle (β).

Once the forces are known on one of these coordinate systems, it is easy to find the equivalent ones on the other. To do so, we need to multiply them by the transformation matrix given by:

$$\begin{aligned}
\mathbf{Q}^{A/B} &= \begin{bmatrix} \cos \beta & \sin \beta & 0 \\ -\sin \beta & \cos \beta & 0 \\ 0 & 0 & 1 \end{bmatrix} \begin{bmatrix} \cos \alpha & 0 & \sin \alpha \\ 0 & 1 & 0 \\ -\sin \alpha & 0 & \cos \alpha \end{bmatrix} \\
&= \begin{bmatrix} \cos \beta \cos \alpha & \sin \beta & \cos \beta \sin \alpha \\ -\sin \beta \cos \alpha & \cos \beta & -\sin \beta \sin \alpha \\ \sin \alpha & 0 & \cos \alpha \end{bmatrix} \tag{2.35}
\end{aligned}$$

One just needs to transpose the matrix to have the opposite transformation (from body-fixed to aerodynamic system).

$$\mathbf{Q}^{B/A} = [\mathbf{Q}^{A/B}]^T \tag{2.36}$$

2.2.2 Forces and Moments

When the flow goes along the body, it changes its direction due to the pressure exerted from the body's presence. According to Newton's second law, the body will also experience an equal reverse force from the flow.

Since we are considering a viscous flow, there is friction between the flow and the capsule's wall produced by the flow viscosity and the continuous decrease in speed, ideally achieve no-slip condition at the wall.

Taking this into account, both pressure and viscous shear stress produce the forces on the body. Integrating these properties along the body's surface gives us the equivalent forces exerted on the body.

Separating the forces in terms of pressure and viscous forces (F^P and F^V), we can also have the respective coefficients. Considering ρ_∞ and p_∞ as the density and the pressure of the freestream, and A_{ref} the reference area used to compute the forces and moments:

$$F = F^P + F^V \tag{2.37}$$

$$F^P = - \int \int_S (p - p_\infty) \hat{\mathbf{n}} dS \quad \text{and} \quad F^V = \int \int_S \boldsymbol{\tau} dS \tag{2.38}$$

Yields

$$C_F = C_F^P + C_F^V \tag{2.39}$$

$$F^P = - \frac{1}{A_{ref}} \int \int_S C_p \hat{\mathbf{n}} dS \quad \text{and} \quad C_F^V = \frac{1}{\frac{1}{2} \rho_\infty U_\infty^2 A_{ref}} \int \int_S \boldsymbol{\tau} dS \tag{2.40}$$

$$\text{with} \quad C_p = \frac{p - p_\infty}{\frac{1}{2} \rho_\infty U_\infty^2} \tag{2.41}$$

Further details on this integration along the capsule wall are presented in Appendix A.

One obtains the aerodynamic coefficients in the aerodynamic coordinate system, and as mentioned before. Finally the transformation is done by simply multiplying the vector by the matrix:

$$\begin{bmatrix} -C_D \\ C_Y \\ -C_L \end{bmatrix} = \begin{bmatrix} \cos \beta \cos \alpha & \sin \beta & \cos \beta \sin \alpha \\ -\sin \beta \cos \alpha & \cos \beta & -\sin \beta \sin \alpha \\ \sin \alpha & 0 & \cos \alpha \end{bmatrix} \begin{bmatrix} C_{FX_B} \\ C_{FY_B} \\ C_{FZ_B} \end{bmatrix} \quad (2.42)$$

2.3 Radiation

In this section, some fundamental concepts regarding the radiative transfer computations are presented.

As briefly discussed before, in these high temperature regimes, there is an additional energy exchange in the form of electromagnetic radiation due to transitions from upper to lower internal energy levels of atoms/molecules (emission) or vice-versa (absorption).

The radiation emitted or absorbed may have a significant contribution regarding surface heating of the capsule and the flow field itself since it directly affects the energy equations through the source term explicitly present in the equations.

In this work, the flow field's solution is decoupled from radiation, with the radiative properties of the flow calculated over a converged CFD solution.

2.3.1 Emission and Absorption Coefficients

Atomic and molecular energy levels are quantized, and consequently, emission and absorption of radiative energy are also quantized.

Photons, particles traveling at the speed of light, carry *packets* of energy, equal to the product of Planck's constant and the photon frequency:

$$E = h\nu \quad (2.43)$$

Radiative transitions may take place between discrete levels and/or continuum energy levels with only the translational motion of the particle differing².

1. Bound-bound transitions

These take place between two quantized energy levels of an atom/molecule. The energy level quantization is reflected in the spectrum as sharp peaks at a specific frequency (diracs), corresponding to the energy gap between upper and lower energy levels, broadened into Gaussian/Lorentz shapes.

Atomic bound-bound transitions are related to the electronic states of the atom. As to molecular bound-bound transitions, these can relate to individual ro-vibronic states³ of the molecule. As a result, the emission and absorption spectra are systems of bands of closely spaced lines corresponding to individual vibrational and electronic transition groups [8, 30, 31].

²Although strictly speaking, the translational motion is also quantized, however the energy gaps are small enough that in practice, these levels appear as a continuum.

³defined by a particular set of vibrational, rotational and electronic quantum numbers

2. Bound-free transitions

Atom or molecules can expel an electron, and since this free electron is allowed to have any velocity and, consequently, any value of kinetic energy, these transitions reflect in continuum radiation.

3. Free-free transitions

This phenomenon gives rise to continuum radiation phenomena same as Bound-free transitions, but this time, the electron is accelerated/decelerated due to an interaction with an electric field.

Discrete radiation

We start by introducing the relevant Einstein coefficients which are the probability of particular bound-bound transitions between two energy levels l and u : A_{ul} for spontaneous emission, B_{ul} for induced emission and B_{lu} for absorption. These three fundamental radiative transitions are presented in Figure 2.3.

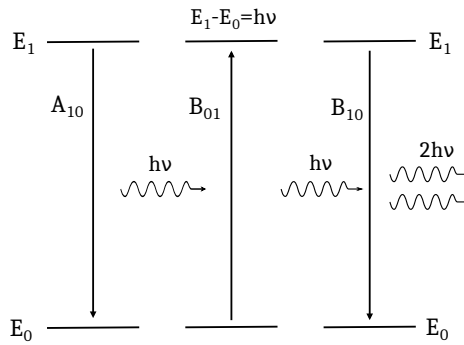


Figure 2.3: Elementary radiative processes, from left to right: spontaneous emission, absorption and induced emission.

The spectral emission $j_{\nu,ul}$ and absorption $\kappa_{\nu,ul}$ coefficients for an atomic or molecular bound transition with energy $h\nu_{ul}$ are

$$j_{\nu,ul} = \frac{N_u h \nu_{ul}}{4\pi} A_{ul} \phi_{ul}(\nu) \quad (2.44)$$

$$\kappa_{\nu,ul} = (N_l B_{lu} - N_u B_{ul}) h \nu_{ul} \phi_{ul}(\nu) \quad (2.45)$$

with N_u and N_l the number densities of upper and lower energy levels, respectively, and $\phi_{ul}(\nu)$ is the spectral distribution function of the $u \rightleftharpoons l$ line transition due to broadening mechanisms. The spectral lines are not truly monochromatic (at a precise $h\nu_{ul}$) but instead appear smeared over a finite frequency range. Therefore these broadening mechanisms, such as Doppler broadening or Stark broadening, are beyond the scope of this work and can be consulted in the relevant literature [8, 32, 33] for example.

The three Einstein coefficients can be related through the Detailed Balance Principle, which means only one of the coefficients need to be computed.

Using the so-called Generalized Krichhoff-Planck Law (2.46), the other coefficient can be found as

$$\frac{j_{\nu,ul}}{\kappa_{\nu,ul}} = \frac{2h\nu_{ul}^3}{c^2} \left(\frac{g_u N_l}{g_l N_u} - 1 \right)^{-1} \quad (2.46)$$

where g_l and g_u are the degeneracies of the lower and upper states, respectively.

N_u and N_l can be computed assuming either Boltzmann distributions at one specific temperature (either a global temperature T or individual non-equilibrium temperatures, T_{tra} , T_{vib} , T_{rot} or T_{exc}) or considering state-to-state description or even a simplified collision-radiative model.

Continuum radiation

The bound-free or free-free transitions may include emission or absorption of a free electron. From energy conservation,

$$h\nu = E_{ion} + \frac{1}{2}v_e^2 \quad (2.47)$$

with E_{ion} as the ionization energy of the atom/molecule. Below this energy, these transitions cannot occur since the electron is not emitted (there is no ionization process). As a consequence, this reflects in a limitation to higher frequency ranges in the spectrum.

The absorption coefficient is computed taking into account the population of the absorbing states and the corresponding emission coefficient is calculated using a slightly different expression for the aforementioned Kirchhoff-Planck's Law (2.46). This absorption coefficient is determined from computed or measured level-dependent absorption cross-sections $\sigma_i(\nu)$. An example of calculation of this coefficient for cases of bound-free transitions follows:

$$\kappa_{\nu}(\nu) = \left(\sum_i N_i \sigma_i(\nu) \right) \left[1 - \exp\left(-\frac{h\nu}{k_B T_{el}}\right) \right] \quad (2.48)$$

2.3.2 Radiative Energy Transfer

Once the absorption and emission coefficients for the flow are known, the global radiative transfer process may be described as follows.

We start by defining the spectral radiative energy flux q_{ν} at a point P:

$$q_{\nu} = \int_{4\pi} I_{\nu}^{\theta,\phi} \mathbf{s} \cdot \mathbf{n} d\Omega = \int_{4\pi} I_{\nu}^{\theta,\phi} \cos\theta d\Omega = \int_0^{2\pi} \int_0^{\pi} I_{\nu}^{\theta,\phi} \cos\theta \sin\theta d\theta d\phi \quad (2.49)$$

where θ_c and ϕ are the azimuthal and zenithal angles of an arbitrary direction defined by the vector s . $I_{\nu}^{\theta,\phi}$ is the spectral directional radiative intensity and is defined as the radiative energy transferred in the s direction across a unit area perpendicular to s per unit frequency, per unit time, per unit solid angle. The spectral surface radiative heating q_{ν}^- is obtained by integrating θ_c between 0 and $\frac{\pi}{2}$ instead of π , as we consider radiation coming from an hemisphere above the point under consideration.

Integrating q_{ν} over all frequencies, we obtain the magnitude of q_R .

$$q_R = \int_0^\infty \int_\Omega q_\nu d\Omega d\nu \quad (2.50)$$

This is useful for computing fluxes in physical boundaries but to solve the radiative source term appearing in the total energy equation (2.1c), one must estimate the divergence of the local radiative heat flux vector.

To perform the same approach in a vector form, we remove the dot product with n in the equation (2.49):

$$-\nabla \cdot \mathbf{q}_R = -\nabla \cdot \int_0^\infty \int_{4\pi} I_\nu^{\theta,\phi} \mathbf{s} d\Omega d\nu \quad (2.51)$$

The radiative transfer equation (Beer-Lambert law) represents the change in the radiative intensity $I_\nu^{\theta,\phi}$ as a ray travels along a path s defined by θ_c and ϕ through an emitting and absorbing gas, and may be written as [30, 34]:

$$\mathbf{s} \cdot \nabla I_\nu^{\theta,\phi} = \frac{dI_\nu^{\theta,\phi}}{ds} = j_\nu - \kappa_\nu I_\nu^{\theta,\phi} \quad (2.52)$$

with j_ν and κ_ν the emission and absorption coefficients. Introducing the optical thickness τ_ν , defined by

$$\tau_\nu(s) = \int_{s'=0}^{s'=s} \kappa_\nu ds' \quad (2.53)$$

and introducing the relation $d\tau_\nu = \kappa_\nu ds$, equation (2.52) can be rewritten as

$$\frac{dI_\nu^{\theta,\phi}}{d\tau_\nu} = \frac{j_\nu}{\kappa_\nu} - I_\nu^{\theta,\phi} \quad (2.54)$$

Using the radiative transfer equation, we may rewrite the equation (2.51) as

$$-\nabla \cdot \mathbf{q}_R = \int_0^\infty \int_{4\pi} \kappa_\nu I_\nu^{\theta,\phi} d\Omega d\nu - 4\pi \int_0^\infty j_\nu d\nu \quad (2.55)$$

If we assume $I_\nu^{\theta,\phi}$ in the form of $I_\nu^{\theta,\phi} = c(\tau_\nu)e^{-\tau_\nu}$ with $\tau_\nu(0) = 0$, the solution to equation (2.54) is expressed as

$$I_\nu^{\theta,\phi}(\tau_\nu(L)) = I_\nu^{\theta,\phi}(0)e^{-\tau_\nu(L)} + \int_0^{\tau_\nu(L)} \frac{j_\nu}{\kappa_\nu} e^{-(\tau_\nu(L)-\tau_\nu(s))} d\tau_\nu \quad (2.56)$$

This expression may be divided into two terms with distinct physical meanings regarding its contribution to the local radiative intensity $I_\nu^{\theta,\phi}$. The first term, similar to a Beer-Lambert's Law, stands for the incoming intensity $I_\nu^{\theta,\phi}(0)$ attenuated by the absorption between $s = 0$ and $s = L$; The second term stands for the emitted radiation at any point between 0 and L , attenuated by the remainder of the integration path between s and L .

Depending on how the equation (2.56) is solved, several models can be employed, being the most common models:

- Tangent-slab model
- Ray-tracing model

A brief explanation of these models are given in the next subsections. For more details regarding these models, namely a more detailed mathematical formulation can be found in [7].

2.3.2.1 Tangent-slab Model

This model has been widely used in the past. It is the simplest among the ones presented and has reasonable accuracy. Its main advantage is the low computational cost compared with the other models. This model's accuracy decreases significantly while moving from the stagnation region to the shoulder/forebody region.

This model's primary assumption is that the flow is considered as being constant along a line of sight normal to the body. This is the same as saying that the properties do not suffer variation tangentially to the body's local point being analyzed. Consequently, the radiative field's azimuthal direction dependency is dropped, and the integration over the solid angle may be expressed analytically (2.56). This geometric approach is represented in Figure 2.4 where the transparent color represents the real temperature field and solid colors represent the temperature field considered for tangent slab calculations extended to infinity (only represented for one side) for the point represented in red (in this case, the stagnation point).

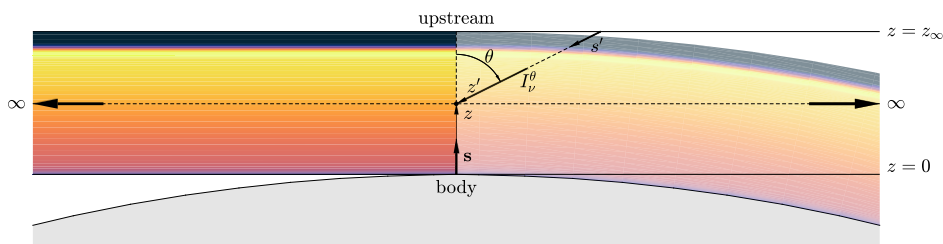


Figure 2.4: Tangent-slab model representation (Adapted from [7]).

For each wall cell, the only computation needed is from the adjacent cells, normal to the wall, which is why this model is computationally less expensive.

Also, on the stagnation region, the assumption of the flow properties distribution as being constant tangentially to the body is more reasonable than in other regions, explaining its better accuracy in this zone.

2.3.2.2 Ray-Tracing Model

This model is becoming more widespread for estimating radiative heating, especially for designing TPS systems, around the scientific community, owing to its improved accuracy particularly for being a better alternative to the tangent-slab model near the shoulder, where the accuracy of the latter decreases significantly. Its application to the calculation of the radiative source term in the energy equation is usually neglected, as the radiative computation is usually fully or partially decoupled from the field computation.

This model bases its approach on the spatial integration of equation (2.56) along a given ray between each point located inside the domain and a point located on its boundary, followed by integration on all rays with different directions. Each ray is then analyzed, taking into account the cells in which it goes

through, solving the radiative equation (2.56) along each ray path, accounting for the length of the ray crossing each grid cell.

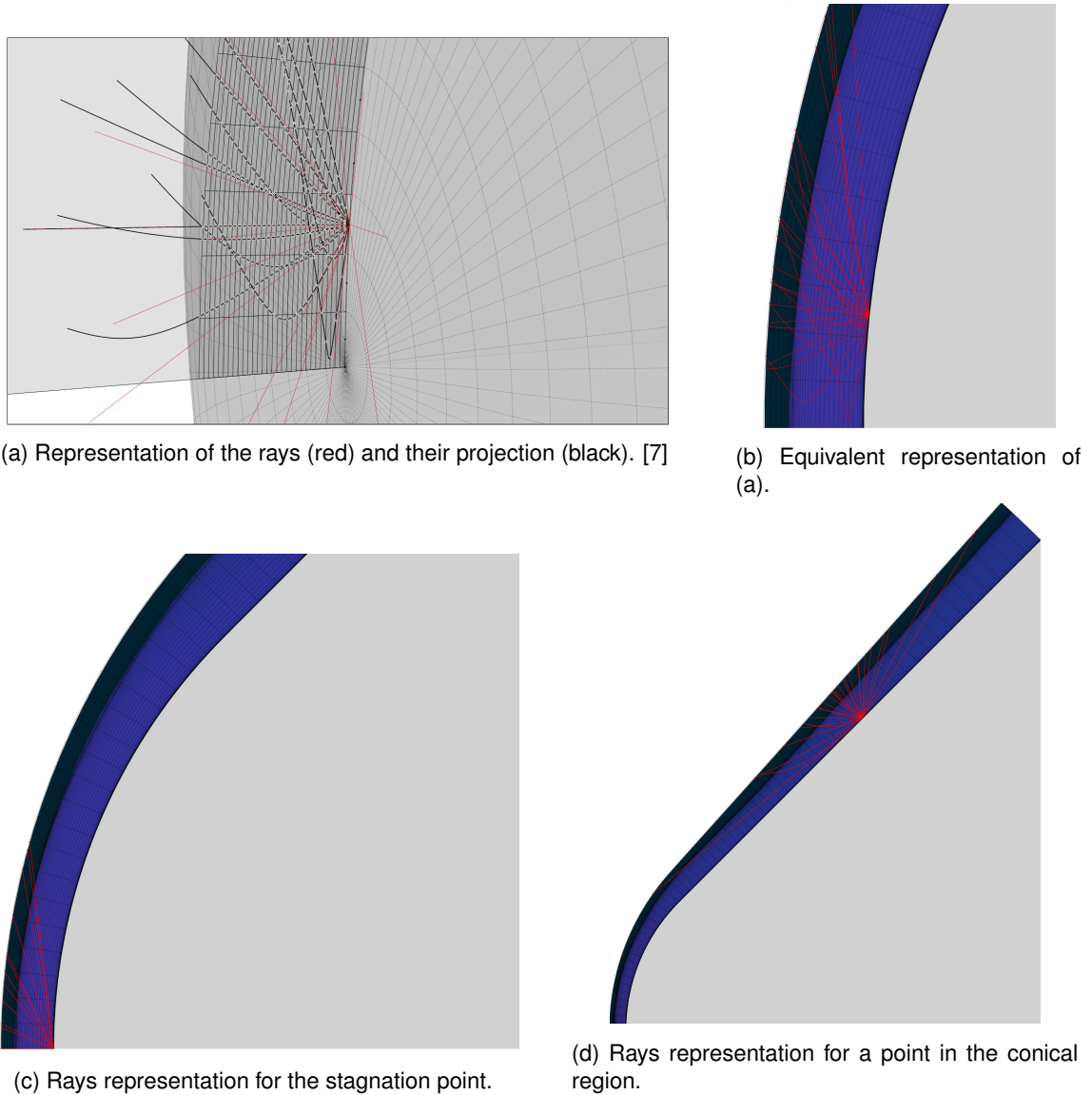


Figure 2.5: Rays Representation with 50 rays per hemisphere - Example for $\theta = 45^\circ$.

Since each ray will not be aligned with every cell center, there is the need to define how the integration will be made along each ray path. One option is to consider constant parameters throughout the cell, with resulting discontinuities in the cell boundaries. This can reduce the accuracy of the resulting radiative intensity of a ray while integrating through coarse cells.

Another option is to linearly interpolate the radiative coefficients, considering the adjacent cells. Figure 2.6 outlines this linear interpolation approach. For each cell, there are two points where a ray intercepts the cell borders, and this method considers a linear change of the relevant variables used for computing $I_{\nu}^{\theta, \phi}$ along this ray slice. This is a feature already available in SPARK LbL.

A check must be made to confirm the influence and feasibility of this interpolating method. More details on this methods will be provided on §4.4.3.3.

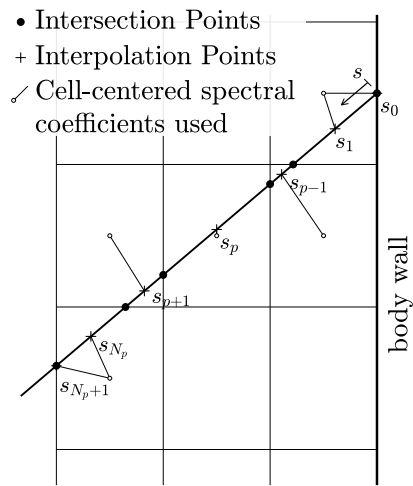


Figure 2.6: Representation of Linear Interpolation in the Ray Tracing at a given cell. Adapted from [7].

Chapter 3

Numerical Modeling

This chapter outlines the numerical implementation of the physical/chemical models presented in Chapter 2. This includes the description of the CFD and radiative transfer codes utilized in this work, and their associated Chemical, Transport and Radiative databases. We also provide details on the domain discretization, and discuss numerical convergence analysis.

Both trajectory points (ballistic entry and aerocapture) used in the simulations are fully described, with some reasoning for the assumptions that were made.

3.1 CFD Solver - SPARK

Software Package for Aerothermodynamics, Radiation and Kinetics (SPARK) [35], is the CFD code used for this work. It is used to simulate high-entropy hypersonic multi-dimensional flows and offers excellent flexibility and extendability since it allows the implementation of new physical models, numerical solvers, and mesh routines, thanks to its object-oriented configuration. This software is coded in Fortran 03/08 and maintained by Instituto de Plasmas e Fusão Nuclear (IPFN) from Instituto Superior Técnico (IST).

SPARK is capable of carrying 0D (temporal relaxation), 1D (post-shock relaxation) or 2D (cylindrical or asymmetric flow) simulations, multi-temperature or state-to-state with frozen or perfect gas conditions, and also allows the input of kinetic models for complex chemical reaction mixture [35].

The current version of the code does not account for turbulence. Typically turbulence is disregarded for the simulation of the shock layers of entry flows, since the flow has favorable pressure gradients and may be considered as laminar. Furthermore, the physics of hypersonic flow turbulence is poorly known to these days [36].

Regarding the numerical solver, either implicit or explicit time-discretization is available in SPARK. The solver uses cell-centered time-dependent finite volume with Second-Order Harten-Yee scheme discretization for the convective fluxes together with a minmod flux limiter that avoids numerical instabilities.

This code is in constant development, with an associated framework including git versioning and project management (redmine). A custom framework for regression testing is also implemented.

The results presented in this work were simulated within the branch developed by Luís Fernandes while working on his Thesis [7]. This branch focused on implementing detailed transport models for high temperature light species neutral and ionized (H_2 , H_2^+ , H , H^+ , He) characteristic for Gas Giants.

Since we used this custom branch, some routines that required some changes (mesh refinement, for example) were not able to be done on SPARK and were carried out externally. Specifically, the mesh refinement routines will be discussed later in §3.7.

3.2 SPARK Line by Line Code

SPARK Line-by-Line (SPARK LbL) [37] is a line-by-line radiative solver maintained at IPFN that computes the spectrally-dependent emission and absorption coefficients of a gas mixture in non-equilibrium. It is a libre code written in MATLAB.

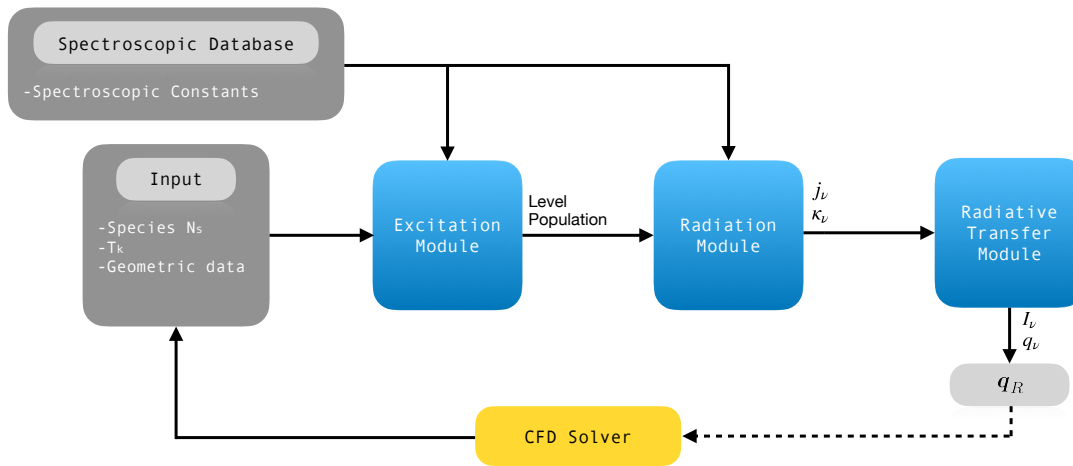


Figure 3.1: Spark LbL Structure with several Modules.

The code relies on the results from the SPARK CFD Solver. This routine considers the temperature associated with each thermal energy mode and each species' number density and generates an input file for every cell, containing several details, including geometric details about the cell location and shape. Both this input file (for each cell) and a spectroscopic database containing species' electronic levels, level degeneracies, spectroscopic constants, and other parameters are fed into an Excitation Module responsible for computing the internal level populations. Conversely, this level population and the database already referred are fed into another module (Radiation Module), which computes the spectral emission and absorption coefficients from specific quantum-mechanical models selected *a priori*. After the computation of j_ν and κ_ν , there is a radiative transfer module which allows the calculation of spectral radiative intensity, I_ν , and spectral radiative energy flux, q_ν . In this case, since the desired properties being computed are the radiative heating fluxes, this module is indeed used. Note that the Radiative Transfer Module was redesigned in Fortran by Fernandes [7] as the rest of the modules described are used in MATLAB software. A simple representation of the SPARK LbL Structure is presented in Figure 3.1.

3.2.1 Ray Tracing - Ray Distribution

Discretizing the space through the rays can be more or less accurate depending not only on the amount of rays used, but also on the way these are generated.

Particularly, using a Fibonacci Lattice is one of the best ways to evenly distribute the rays to appropriately cover a spherical region (with an array of points with similar solid angles). This lattice's generation of points relies on the golden ratio (Φ) and this process is represented in Figure 3.2 for a number of 21 points. The resulting points are generated based on overlapping two spirals. Consecutive points present a specific turning angle defined by the golden angle ($360^\circ \Phi^{-2} \approx 137.5^\circ$) in the first spiral (red) and its complementary angle ($360^\circ \Phi^{-1} \approx 222.5^\circ$) in the second spiral (blue).

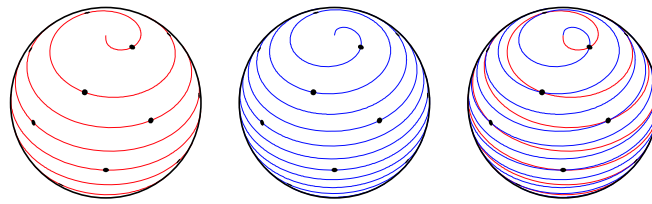


Figure 3.2: Representation of the generation of Fibonacci lattice points. [38]

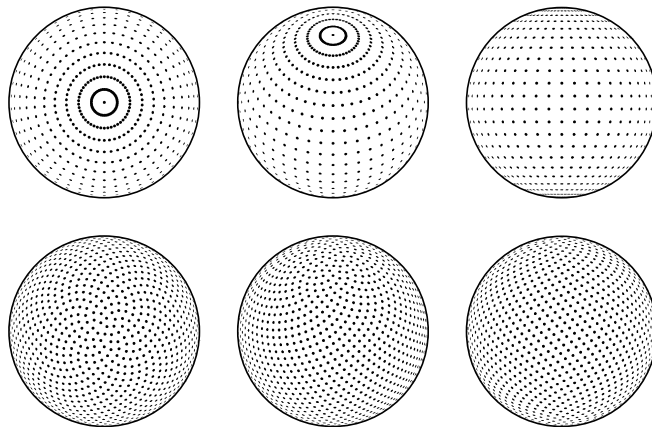


Figure 3.3: Latitude-Longitude lattice (top) vs Fibonacci lattice (bottom). (Adapted from [38]).

This distribution, and a comparison with a simple Latitude-Longitude distribution (azimuthal and polar angles distributed evenly) can be visualized in Figure 3.3. One can clearly point out the improvements, as the Fibonacci Lattice method avoids the clustering of the rays near the polar region, finding this method an obvious choice for best distributing the rays used for this Ray Tracing procedure.

3.3 Trajectory Point

Depending on the trajectory point used in the simulations, several physical models may or may not be implemented. To confirm if the partial differential Navier Stokes equations can be used, one may verify a dimensionless property that evaluates how accurate the assumption of the flow being a continuum is: the Knudsen Number K_n [4]. This property is particularly important for the accuracy of the hypothesis

of the no-slip condition assumed at the wall. Depending on the body geometry, at certain conditions of pressure, density, and temperature (and thus, altitude), this condition may no longer stand. Figure 3.4 splits the possible solutions in different regimes according to the Knudsen Number.

The following equation describes this dimensionless number:

$$K_n = \frac{k_B T_\infty}{p_\infty \sqrt{2} \sigma l} \quad (3.1)$$

where k_B is the Boltzmann's constant, T_∞ and p_∞ are the temperature and pressure at the freestream and σ and l represent the effective collision cross section (assumed 0.2 nm^2 - considering only the H_2 molecule - as a conservative approach) and l a characteristic dimension of the reentry body, here assumed as the capsule diameter (3m).

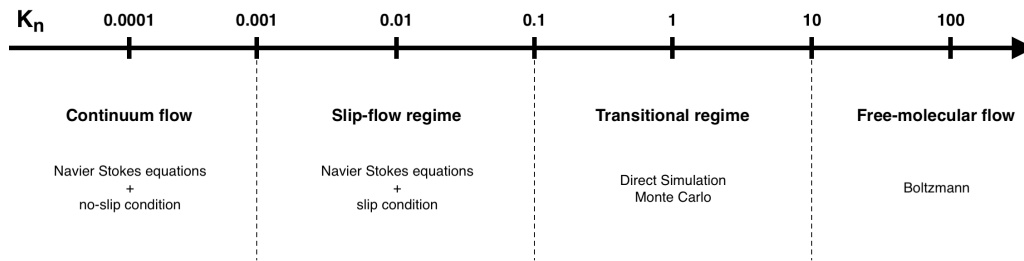


Figure 3.4: Different regimes and equations/conditions applicable for different K_n .

3.3.1 Aerocapture Trajectory Point

Preliminary studies showed that a successful aerocapture would start with an entry velocity of 29 km/s at an altitude of around 100-300 km (above one-bar pressure level) [12]. Using Hollis *et al.* [10] and Jits *et al.* [9] range of trajectories points, a velocity of 29 km/s and an altitude of 130 km were chosen. Using the database available in NASA's software Neptune's Global Reference Atmospheric Model (Neptune GRAM), correspondent density, temperature and pressure at this point were found. Considering the same trajectory point for both capsule designs, we can construct Table 3.1.

Lunine *et al.* [39] describe Neptune's atmosphere and at this altitude provide values of 1 mbar (100 Pa) and 130 K for pressure and temperature, which is close to the values retrieved from Neptune GRAM.

Table 3.1: Aerocapture TP properties used in simulations.

V [km/s]	29
p [Pa]	145
ρ [kg/m ³] ($\times 10^{-3}$)	0.378
T [K]	120.3
h (from 1 bar) [km]	130

For the remaining of this work, this trajectory point will be simply referred to as Aerocapture TP (Trajectory Point) for simplicity.

3.3.2 Ballistic atmospheric Entry Trajectory Point

One may also study a ballistic atmospheric entry instead of an aerocapture to gather useful information for future missions and compare it with ESA's Concurrent Design Facility (CDF) Study.

Using this ESA's CDF Study on The Mission to the Ice Giants [2] accurate values can be found (velocity, pressure, and density) for the point where it is estimated the wall heat fluxes to hit maximum values in a ballistic atmospheric entry, which is the most critical point of the mission. These are presented in Table 3.2. Note that these values differ for both capsule configurations (60° and 45°).

Using the database available in the NASA's software Neptune's Global Reference Atmospheric Model (Neptune GRAM), we were able to interpolate these values to an equivalent height of 82.3 km for $\theta = 60^\circ$ and 77.3 km for $\theta = 45^\circ$ (check Appendix C, Figure C.1).

Table 3.2: Ballistic atmospheric entry point properties used in simulations.

Cone angle θ	60°	45°
V [km/s]	18.05	18.27
p [Pa]	698	892
ρ [kg/m ³] ($\times 10^{-3}$)	2.996	4.229
T [K]	74.5	66.5
h (from 1 bar) [km]	82.3	77.3

At the three trajectory points used (aerocapture and atmospheric entry for both configurations), the equivalent Knudsen numbers are between 1×10^{-5} and 1×10^{-6} , which confirms the validity of using the NS equations mentioned before.

For the remaining of this work, this trajectory point will be simply referred to as Entry TP (Trajectory Point) for simplicity.

3.3.3 Atmosphere

There are some doubts regarding Neptune's atmospheric composition. What is known is that it is mainly composed of Hydrogen (H_2) and Helium (He), with a small fraction of methane (CH_4). For this work, two different compositions were considered: one with methane and another without it.

The compositions used for the molar fractions are represented on Table 3.3. In composition B, the presence of CH_4 was ignored, and the values were adapted from A. These values were based on the information (density and pressure) gathered from the already mentioned ESA's CDF Study [2], and using NASA's Neptune GRAM Software database to find the correspondent chemical composition at these specific heights (82.3 km and 77.3 km). For these altitudes, the compositions are very similar, and thus they were considered the same for both $\theta = 60^\circ$ and $\theta = 45^\circ$. (check Appendix C, Figure C.1)

Table 3.3: Chemical compositions.

	x_{H_2}	x_{He}	x_{CH_4}
A (with CH_4)	79.75 %	18.71 %	1.54 %
B (no CH_4)	81.00 %	19.00 %	0.00 %

3.4 Chemical Model Database

Different chemical kinetic models may be used for representing the reactions on H₂-He-CH₄ mixtures. Some species may be neglected in some approaches, and other species considered in different approaches. The present work considers a chemical model with 16 or 7 species (A and B compositions respectively). Both options are represented in Table 3.4.

Table 3.4: Species involved for each composition.

	H ₂	H ₂ ⁺	H	H ⁺	He	He ⁺	CH ₄	CH ₃	CH ₂	CH	CH ⁺	C ₂	C ₂ ⁺	C	C ⁺	e ⁺
A	•	•	•	•	•	•	•	•	•	•	•	•	•	•	•	•
B	•	•	•	•	•	•										•

The reactions considered for both compositions and each respective coefficients to calculate constant equilibrium constant K_f are found in §Appendix B, Table B.1.

As recommended in the literature, [40], for the reactions between the seven non-carbonaceous species (H, H₂, He, H⁺, H₂⁺, He⁺, and e⁻) of H₂-He mixtures the rates employed were from Leibowitz and Kuo [41]. This data was retrieved in 1972 from experimental data using shock tube experiments at velocities ranging from 13 to 20 km/s. Recently, in NASA Ames Research Center, most precisely in Electric Arc Shock Tube (EAST) facilities, several shock tube experiments were performed for H₂-He mixtures with velocities in the 20-30 km/s range [42]. Radiance phenomena started to be noticeable with velocities around 25 km/s. For the velocities for Entry TP referred to in this work (~ 18 km/s) radiance is expected to be negligible for the H₂-He mixture alone. However, the presence of CH₄ may bring this assumption into question. However, for the Aerocapture TP, the velocity is beyond the 25 km/s (29 km/s), and although the pressure and density are shallow compared to atmospheric entry values, a cross-check regarding the radiative influence will be made.

The rates for the reactions involving the carbonaceous species were retrieved from the work done by Lino da Silva [43] for a fast Titan's atmospheric entry, which focused on validating rates from Gökçen's work [44], who updated Nelson's chemical model [45]. Although this work from Lino da Silva focused on N₂-CH₄ mixtures, the reactions between carbonaceous and hydrogenous species may still be used for the present work.

3.5 Transport Models Database

Using the framework implemented by Fernandes [7], the SPARK version used for this work can apply several Collision Cross Section (CCS) databases available in the literature.

For the model considered - Gupta/Yos Model - it is required to provide all CCSs for all possible species interactions. For the H₂-He interactions, the database was already implemented and provided on [46]. Some charge exchange corrections and phenomenological approaches are applied in some interactions, but their specifics are beyond this work's scope. Detailed information can be found in [7].

For the remaining interactions (the ones with species composed of Carbon elements - CH₄, CH₃,

CH_2 , CH , CH^+ , C , C_2 , C_2^+ , C^+), extensive research was done, but there was not enough information regarding these CCSs at high temperatures. As an approximation, the integral coefficients were copied from H_2 and H CCSs, depending on the type of interaction:

- Molecule - molecule interactions: CCSs copied from H_2 - H_2 interaction
- Molecule - atom interactions: CCSs copied from H_2 - H interaction
- Molecule - ion interactions: CCSs copied from H_2 - H^+ interaction
- Molecule - electron interactions: CCSs copied from H_2 - e^- interaction
- Atom - ion interactions: CCSs copied from H - H^+ interaction
- Atom - electron interactions: CCSs copied from H - e^- interaction

Although this is physically inaccurate, it still adds more accuracy than Wilke/Blottner/Eucken Model since, contrarily to the latter, it does not consider the same CCSs for all species. Also, as the flow is mostly composed of He and H_2 , the inaccuracies from these approximations are not expected to significantly impact the overall properties, and hence the obtained results.

3.6 Radiation Models Database

Regarding the transitions used for the spectral database, most of the validation work was already done by Fernandes [7], making this step easier.

Following the work already done, the only difference relied on the influence of carbonaceous species. Only the transitions of C and C_2 (and their ions) were considered, with transitions from hydrocarbons being neglected. These transitions were also in the database considered by Fernandes [7], owing to the analysis carried regarding radiative blockage from carbonaceous ablation products.

For decreasing computational calculation times of the emission coefficients and radiative power, a few assumptions were brought to split the cells into three main groups according to the cell's vibrational temperature, as shown in Table 3.5. For example, at high temperatures, the presence of H_2 and C_2 would probably be very marginal due to them being already dissociated, which would reflect in a meager influence in radiation if it was to be computed. This way, we ignore some species that, although present in the flow, have a shallow radiative impact in specific cells since their number density is very low locally.

An exercise was done to confirm this hypothesis, and there was less than 0.5% difference (from 4213.3 W/cm^2 to 4215.6 W/cm^2) in the results when splitting the Database into these three groups. This split was more important for the Aerocapture TP since only in this point there were sufficiently high temperatures ($T_v > 10000 \text{ K}$) that allowed this "High Temp" model to be applied. Regarding low temperatures, they were not even achieved since the temperatures did not go below the wall temperature of 1200 K and the "Low Temp" model were defined for $T_v < 500 \text{ K}$.

Table 3.5: Radiative Database.

Species	Comp A - With CH ₄			Comp B - Without CH ₄		
	Low Temp	High Temp	Nominal	Low Temp	High Temp	Nominal
Atomic Lines						
H	•	•	•	•	•	•
He	•	•	•	•	•	•
He ⁺	•	•	•	•	•	•
C	•	•	•			
C ⁺	•	•	•			
Atomic Photoionization						
H	•	•	•	•	•	•
He	•	•	•	•	•	•
He ⁺	•	•	•	•	•	•
C	•	•	•			
C ⁺	•	•	•			
Molecular Photoionization						
H ₂	•		•	•		•
Molecular Photodissociation						
H ₂	•		•	•		•
H ₂ ⁺	•		•	•		•
Atomic Photodetachment						
H ⁻	•	•	•	•	•	•
He ⁻	•	•	•	•	•	•
C ⁻	•	•	•			
Bremsstrahlung						
H	•	•	•	•	•	•
He	•	•	•	•	•	•
He ⁺	•	•	•	•	•	•
C	•	•	•			
C ⁺	•	•	•			
H ₂ ⁻	•		•	•		•

Species	System	Comp A - With CH ₄			Comp B - Without CH ₄		
		Low Temp	High Temp	Nominal	Low Temp	High Temp	Nominal
Molecular Band Systems							
H ₂	Lyman		•		•	•	•
	Werner		•		•	•	•
	Fulcher				•		•
	B ¹ - X		•		•	•	•
	D - X		•		•	•	•
	B ⁰ B - X		•		•	•	•
	D ¹ - X		•		•	•	•
C ₂	Freymark			•			
	Phillips			•			
	Mulliken			•			
	Herzberg - F		•		•		
	Herzberg - g		•		•		
	Herzberg - f		•		•		
	Deslandres-d'Azambuja		•		•		
	Fox Herzberg		•		•		
	Ballik Ramsay		•		•		
Swan		•		•			

3.7 Mesh Study

The mesh considered in this work consists on a structured mesh of 70x60 cells: 60 cells on the tangential direction of the wall and 70 on the normal direction of the wall. However, for some procedures, to achieve results in a realistic time-frame, some solutions were computed with meshes of 50x60 cells, as was the case for the radiative study. Increasing by a factor of 140% the number of cells was enough for the computational times to increase by more than a factor of 2, which would make difficult to reach solutions in time for this thesis' deadline.

3.7.1 Mesh Boundary Conditions

The mesh boundaries are depicted in Figure 3.5.

There were different possibilities for the wall boundary, mainly regarding its catalycity. This catalycity is related to how the flow interacts chemically with the wall. Although at these large speeds and temperatures typical of hypersonic flight, the capsule's wall usually reacts with the flow while being consumed (ablation), this phenomenon will not be considered in this work.

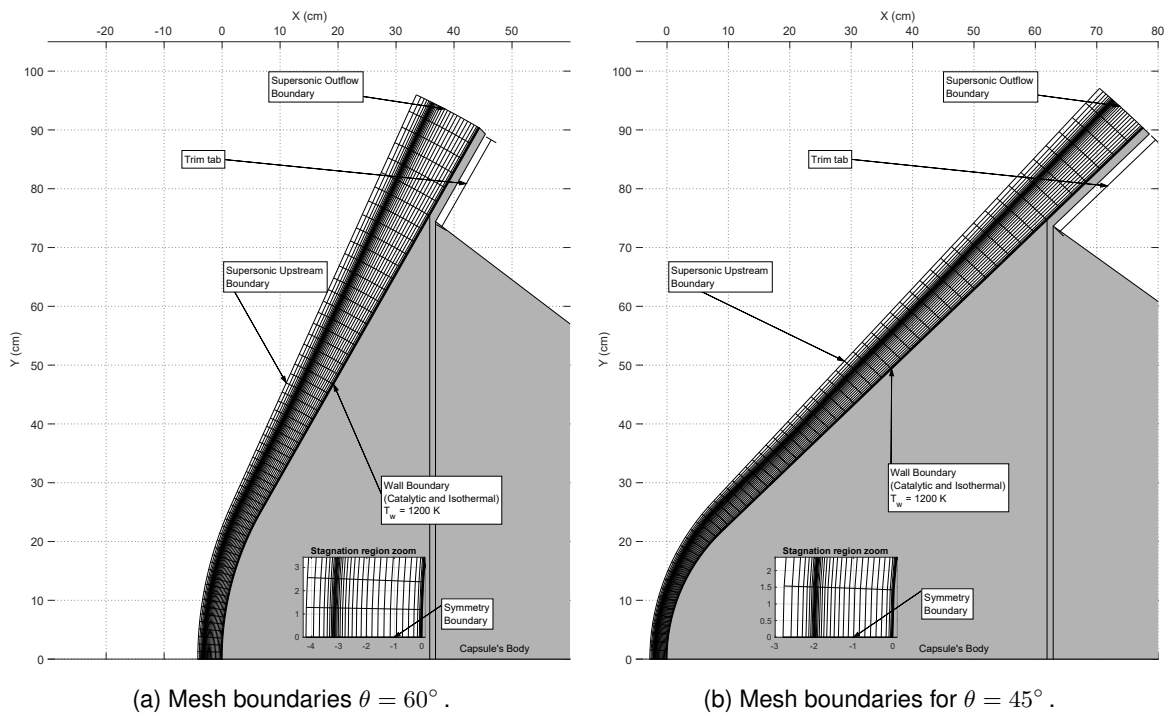


Figure 3.5: Mesh boundaries.

When chemical species hit the wall at these high speeds and temperatures, they may interact with each other. The wall material may enhance this phenomenon, and this is characterized as the wall catalycity. Catalycity is the capability of a material to enhance a chemical reaction rate or change its equilibrium constant.

We can define the wall as:

- Non-catalytic: no atom/ion recombination resulting in the wall not being affected by the flow;

- Partially catalytic: There is some atom/ion recombination;
- Fully catalytic: Full atom/ion recombination.

The fully catalytic option is the one that maximizes the wall heating, since the recombination process is an exothermic reaction, and thus, it is the one that will be adopted in this work in a conservative fashion.

The wall boundary is set to be fully catalytic and kept at a constant temperature (Isothermal wall) of $T_w = 1200 K$.

Note that the trim tab include the wall fraction located at $y \leq 0.75m$. The mesh boundary is considered as an extension of the wall aforementioned.

3.7.2 Mesh Convergence Study

To study the grid convergence of the problem, three types of meshes were considered for all capsule configurations (50x60, 70x60 and 90x60) for a specific trajectory point and chemical reaction. The choice was to use the chemical composition B (without CH_4) and the Entry TP.

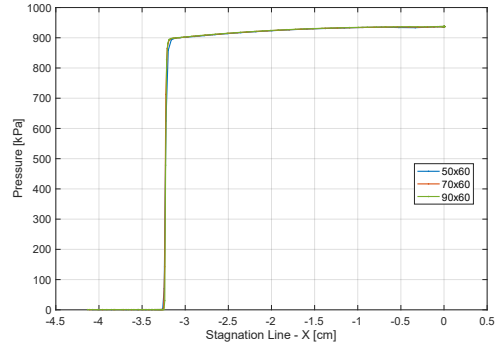
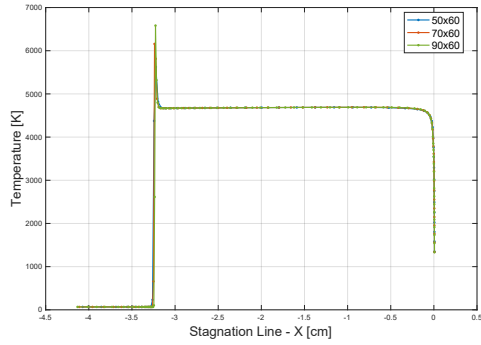
Firstly, for both capsules, a converged solution without refinement was achieved for both 50x60 meshes. After that, the refinement procedures mentioned on §3.7.3 were implemented and all the refined meshes (50x60, 70x60, and 90x60) were generated. After interpolating the converged non-refined field for all the new refined meshes, the solutions for all the meshes were achieved. This interpolating process reduces the computational effort since it does not require both non-refined meshes of 70x60 and 90x60 to be computed from scratch, and can start from the solution of the 50x60 non refined mesh.

The simulations were considered individually converged for each mesh when the Root Mean Square (RMS) of the residuals across all equations dropped below 10^{-4} , although for some of them, further iterations were performed to evaluate the convergence of the individual solution, with most cases dropping its RMS below 10^{-5} .

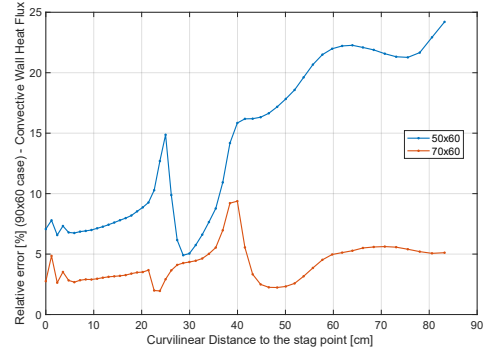
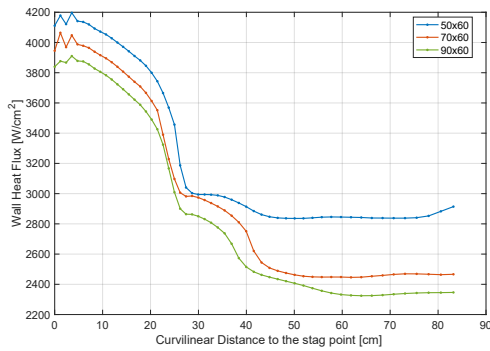
One can evaluate local convergence by checking the fields for the Stagnation Line represented in Figures 3.6a, 3.6b, 3.7a, and 3.7b. There is a good fit between the different meshes for the properties represented. Since all of these meshes were refined to better capture either the shock and the boundary layer, it does not come as a surprise that the shock position and the boundary layer are well defined for all options. However, there are still some differences regarding the peak temperature achieved in the shock, showing an error of -14.5% and -6.5% for 50x60 and 70x60 grids respectively for the $\theta = 60^\circ$ case. As for the $\theta = 45^\circ$ case the differences are of -5.5% and +5.0% in peak temperature for 50x60 and 70x60 grids respectively.

Regarding the global convergence, one must take a look into the different properties along the wall. For this work the most important properties will be the heat flux (for the aerothermodynamic analysis) and the pressure (for the aerodynamic coefficients analysis). There are some discrepancies regarding the convective heat flux along the wall for the different meshes. The errors are significantly larger for the 50x60 meshes in both cases ($\theta = 60^\circ$ and $\theta = 45^\circ$).

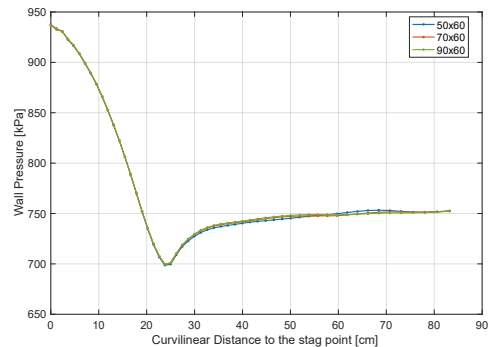
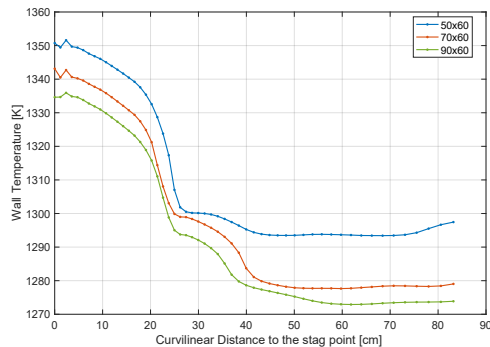
Although there is a significant error in considering 70x60 meshes instead of 90x60 meshes, when studying the influence of CH4 in convective heat, a 90x60 mesh would be computationally very expensive, since not only there are 1200 additional cells (compared to considering 70x90), but there are also 9 more species interacting by several added chemical reactions for each of the cells which slows down the code.



(a) Temperature field in the Stagnation Line for $\theta = 60^\circ$. (b) Pressure field in the Stagnation Line for $\theta = 60^\circ$.



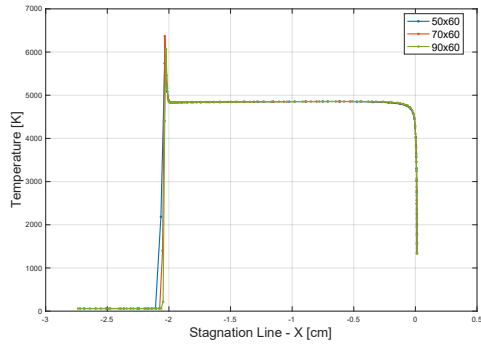
(c) Convective Heat Flux along the wall for $\theta = 60^\circ$. (d) Error in Heat Flux along the wall for $\theta = 60^\circ$.



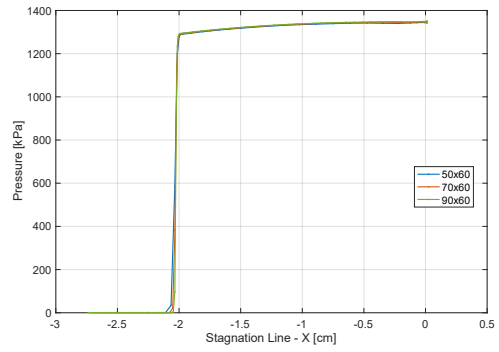
(e) Temperature along the wall for $\theta = 60^\circ$. (f) Pressure along the wall for $\theta = 60^\circ$.

Figure 3.6: Mesh convergence study results for $\theta = 60^\circ$.

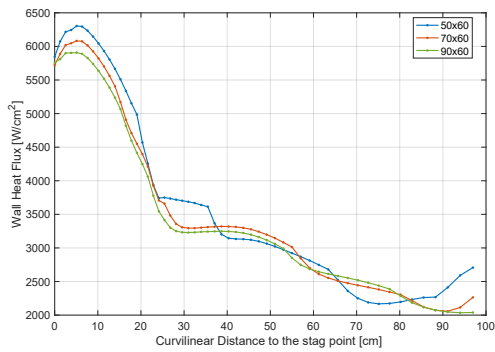
On the other hand, the wall pressure does not suffer significant changes for the different meshes. This is explained by the low influence of the boundary layer on the pressure, contrasting to the important influence of this layer in the temperature. Since the pressure is not very sensible to the mesh choice, the 50x60 meshes will be used for the aerodynamic coefficients analysis as this relies mainly on the pressure field (although there is still a marginal influence from the viscosity).



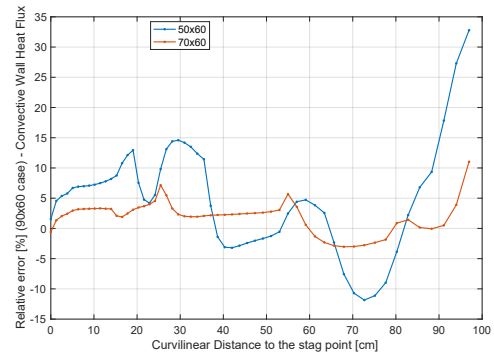
(a) Temperature field in the Stagnation Line for $\theta = 45^\circ$.



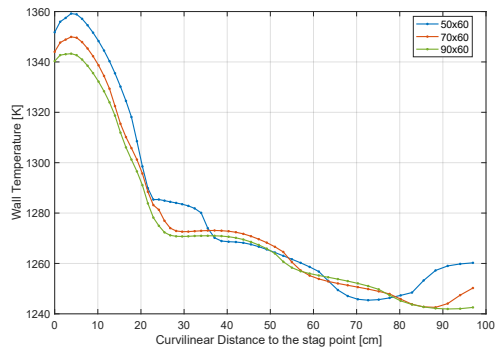
(b) Pressure field in the Stagnation Line for $\theta = 45^\circ$.



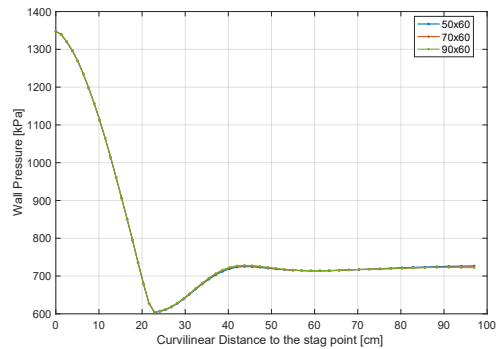
(c) Convective Heat Flux along the wall for $\theta = 45^\circ$.



(d) Error in Heat Flux along the wall for $\theta = 45^\circ$.



(e) Temperature along the wall for $\theta = 45^\circ$.



(f) Pressure along the wall for $\theta = 45^\circ$.

Figure 3.7: Mesh convergence study results for $\theta = 45^\circ$.

A few comments must be made regarding the heat profile plots for both capsule configurations.

- Analyzing Figure 3.6c, there are some instabilities in the first points. This can be explained by the presence of small carbuncles (further details in §3.7.4) that may still be not completely solved.
- For both configurations, but especially in Figure 3.7c one can realize that the maximum value for the wall heat flux does not correspond to the stagnation point. This is a non-physical phenomenon and can be explained as having locally a singularity. This singularity is neither from the physical model nor the geometric shape of the wall. It may be however, a singularity due to the CFD model which presents an symmetry axis which may alter the results.
- There is a sudden change in the heat flux profiles near $S=0.25$ m for both cases. This is not a

physical phenomena, but instead a grid-related issue. The mesh generator does not implement the continuity for the second derivative on the capsule's geometry, which leads to distortions in the calculated flow. This phenomenon is presented for the convective heat flux, wall pressure, and wall temperature profiles. Prabhu *et al.* [47] present a detailed study on this topic, which should be consulted for reference and for the identification of future mitigation actions (essentially enforcing the second derivative continuity between the sphere and cone sections).

3.7.3 Mesh Refinement

The mesh refinement was performed in an external routine (in MATLAB) that refined the mesh considering either the temperature or the pressure field. Two main regions needed refinement: the shock and boundary layer. Figure 3.8 presents an example of the refinement, showing the mesh previously and after the refinement.

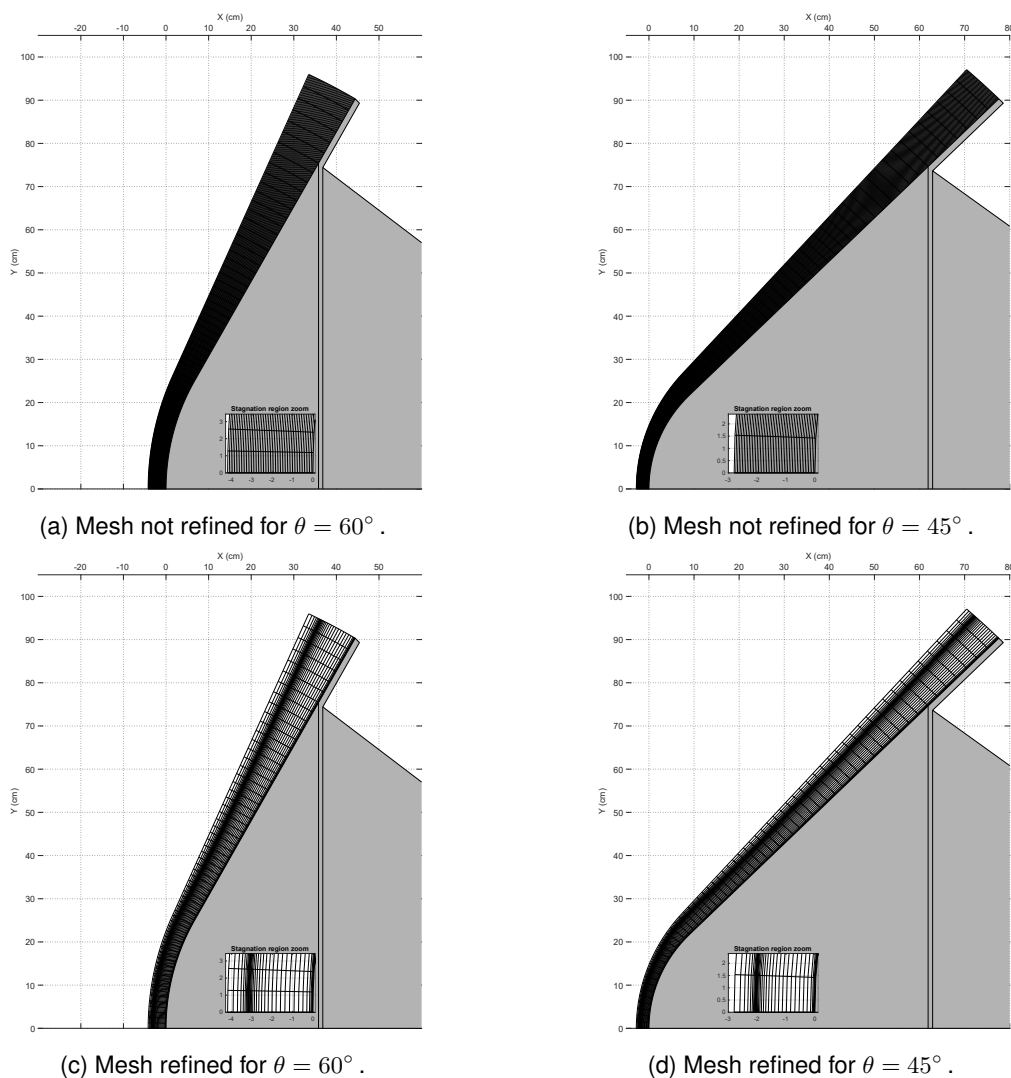


Figure 3.8: Mesh Refinement Example.

For the shock refinement, a routine searched abrupt (but significant) changes in these properties, and there was a clustering of the cells around this region. A clustering factor introduced *a priori* as an

input defined how much clustered the cells were.

To compute accurate values of properties inside the boundary layer, which allows the correct estimation of the wall heating, one must correctly estimate the first cell's height adjacent to the wall (Δn). This estimation can be done by taking into account the definition of cell Reynolds number, given by (3.2)

$$Re_{wall} = \frac{\rho a \Delta n}{\mu} \quad (3.2)$$

with ρ , a and μ being the density, speed of sound and viscosity, respectively, computed on the cell.

Some references on the literature ([48], [49]) argue that this value for the cell adjacent to the wall, Re_{wall} given by (3.3), should be lower than 5, being as close as possible to 1. However, some other references, simply state this is an ideal situation and that the boundary layer can be accurately depicted even for values higher than these. Thompson *et al.* [50] for example, present some studies using Langley Aerothermodynamic Upwind Relaxation Algorithm (LAURA) code, from NASA, with Re_{wall} of 2, 20 and 200. For $Re_{wall} = 200$, there was insufficient information that allowed the boundary layer to be well defined. For the other cases ($Re_{wall} = 2$ or 20), the boundary layer was well represented and there were no significant changes in the field, with errors less than 5% for wall heating.

$$Re_{wall} = \frac{\rho_w a_w \Delta n}{\mu_w} \quad (3.3)$$

In this work, both values of $Re_{wall} = 20$ and $Re_{wall} = 2$ were used at first to test the compromise between accuracy and computational effort needed for converge the flow field on the very refined cells near the wall. The choice of $Re_{wall} = 2$ was immediately discarded since the resulting time step was very small¹, and consequently an enormous time would be needed to find a converged solution. Later, some heat flux profiles seemed inaccurate for $Re_{wall} = 20$ for RMS already very low, which probably meant the flow was not yet converged into a correct solution. The alternative choice used was to increase the value of Re_{wall} and keep a first-cell height constant along the capsule's wall. This alternative uses the input of a desired Re_{wall} for searching the minimum height needed, and this height is applied to every "row" of cells normal to the wall. This procedure would avoid discontinuities and abrupt changes in first height cells, which sometimes occurred since the wall's properties (and consequently the Re_{wall}) suffer significant changes. Although the Re_{wall} was not kept constant, this procedure at least guarantees that the Re_{wall} would not increase more than the input value.

Note that several repetitions of these processes were required since the ρ_w , a_w and μ_w computed after each converged solution is updated, reflecting in the final Re_{wall} varying from the desired input value.

Also, in [7], when using the Gupta-Yos transport model, it was shown that these discrepancies in the first wall cell's height were not significant, compared to when Wilke's model was used. Not only was it desirable to represent the boundary layer accurately, but also it was essential to find these solutions in a realistic time-frame which is why this approach with the Re_{wall} was just used just as an auxiliary method. The minimum first cell's height used in the several meshes was kept between $0.2 \mu\text{m} - 2 \mu\text{m}$

¹Smaller cells are needed for smaller Re_{wall} and this yields in smaller Δt from the CFL constrains

(depending on the case) which seemed enough to correctly capture the boundary layer even though this was equivalent to a $Re_{wall} > 20$.

3.7.4 Numerical Issues

3.7.4.1 Trim Tab cant angle limitations

As already mentioned in §1.3.4, we initially intended to study the cant angle influence on the flow solution and how this would change the pressure distribution and wall heating on the trim tab. However, some numerical problems were encountered.

At first, this was thought to be an error related to the mesh boundary influence on the flow solution, but after some increases on the mesh limits, widening the domain, the same problem kept occurring, with the solution converging always to a non-physical one, with the oblique shock located in a non-physical position, see Figure D.1 in Appendix D.

In view of this, the cant angle study for the aerodynamic coefficients was not performed in this work, and all the simulations were made only with a zero cant angle.

3.7.4.2 Carbuncle

When solving the flow for the capsule with $\theta = 60^\circ$, some numerical issues also raised, particularly one regarding the presence of a carbuncle near the blunt nose region, represented in Figure 3.10a and Figure 3.10c. This phenomenon locally distorts the CFD flow solutions, and it is more common on blunt nose regions on axisymmetric grids [51]. This distortion represents a non-physical phenomenon and must be corrected.

Firstly, the leading cause for this numerical instability is believed to rely on the Euler part of the continuity equations of compressible flows, specifically the convective terms. The diffusive terms presented in the Navier-Stokes equations are then not enough to damp this instability. To solve this problem, Pandolfi and D'Ambrosio [52] advise adapting the aspect ratio of the cells in contact with the "normal shock wave" (near the nose, the bow shock is approximately a normal shock), as shown in Figure 3.9.

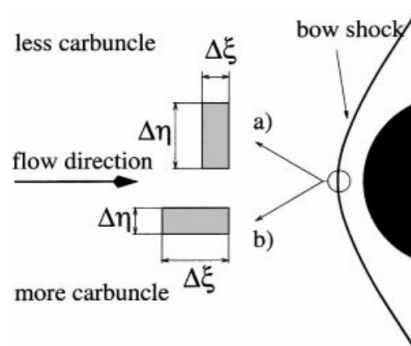


Figure 3.9: Relation of aspect ratio of the cell and probability of carbuncle occurrence according to [52].

If the cell is exaggeratedly elongated, the time step used to solve this cell's conservation equations is smaller than necessary. Reducing the tangential refinement in the nose region is a possible way to avoid

this numerical instability. However, the aspect ratio of the cells from the mesh being considered was already too big, making them very elongated in the tangential direction. For this reason, the opposite of what is represented the Figure 3.9 was done: making the cells less elongated by reducing the clustering in the shock. This phenomenon was probably born due to non-gradual mesh refinement, as the flow restarted from a coarse grid to a well-refined grid. This rough refinement may also result in a poorly estimated shock position.

Figure 3.10 presents the pressure and temperature fields before and after correcting this numerical instability. The correction procedure seems successfully performed.

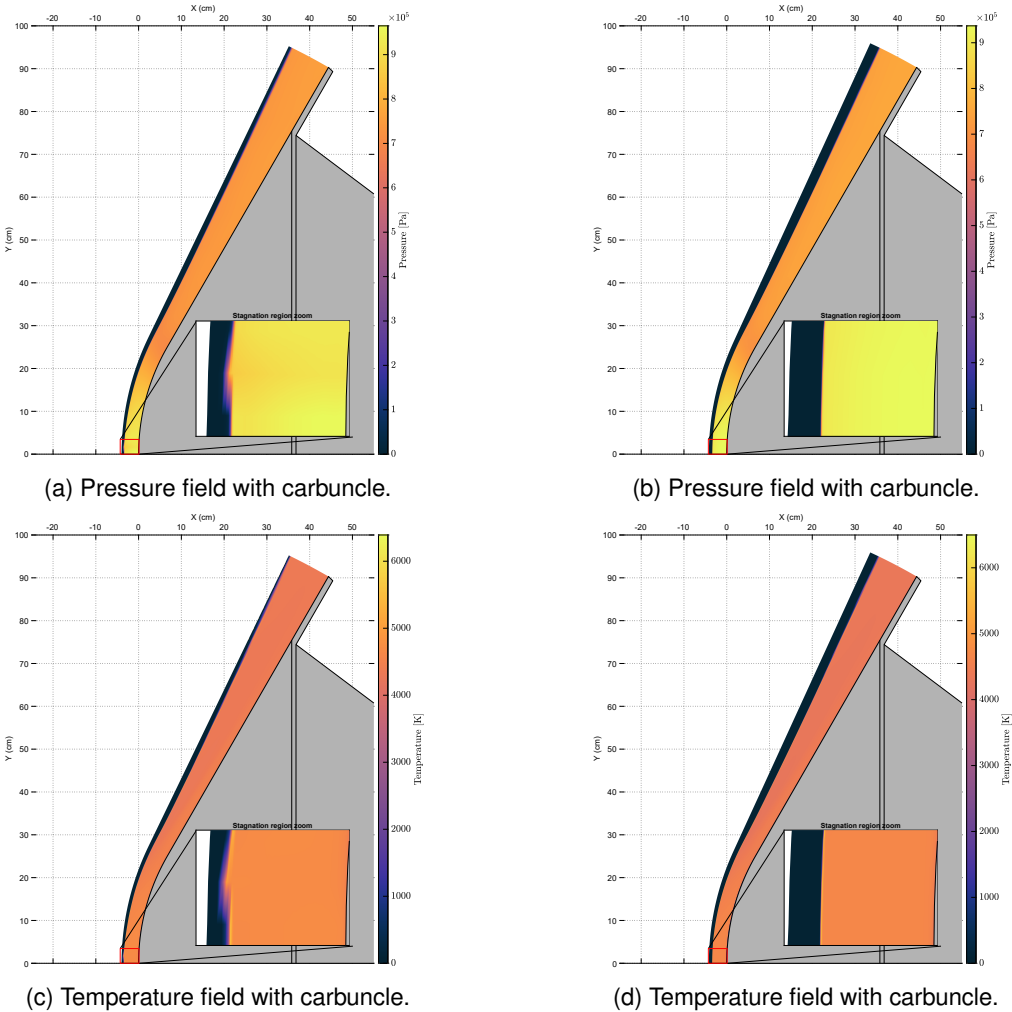


Figure 3.10: Carbuncle representation before and after correction.

Chapter 4

Results

In this chapter, results regarding both test cases are presented. For the first one, both trajectory points will be analyzed, with the main focus on aerothermodynamic analysis, particularly regarding the radiative and convective heat fluxes. Comparison with the literature results in some cases will also be carried out. Finally, the results for the second test case, where the aerodynamic coefficients are analyzed, are displayed.

4.1 Problem Description

The present work is divided in two different problems: Test Case 1 and Test Case 2.

4.1.1 Test case 1 - Aerothermodynamic analysis of Entry Trajectory Point and Aerocapture Trajectory Point

An aerothermodynamic analysis for two different trajectory points (Entry Trajectory Point (TP) and Aerocapture Trajectory Point (TP)) and for the two capsule geometries is carried out. In each of these trajectory points, both chemical compositions will be analyzed, studying the influence of the marginal presence of CH_4 in the results. This aerothermodynamic analysis will focus on computing convective and radiative heating at the wall for all the different cases of study. It will also include an analysis on the stagnation line, specifically on the evolution of the chemical species as well as the radiative power.

Table 4.1 summarizes all the cases that will be analyzed in this test case.

Table 4.1: Test Matrix for Test Case 1.

θ_c [°]	Chemical Comp.	Trajectory Point	Altitude [km]	Velocity [km/s]	Temperature [K]	Pressure [Pa]	Density [g/m ³]
60	A/B	Entry TP	82.3	18.05	75	698	2996
45	A/B	Entry TP	77.3	18.27	67	892	4339
60	A/B	Aerocapture TP	130	29	120.3	145	378
45							

4.1.2 Test case 2 - Aerodynamic analysis of Aerocapture Trajectory Point

Secondly, an aerodynamic analysis will be performed on the Aerocapture TP, studying the influence of the capsule design ($\theta = 60^\circ$ and $\theta = 45^\circ$), the influence of considering the presence of CH_4 and finally, the influence of the sweep angle η under the assumption of a constant area ratio. The main goal will be to compute the aerodynamic coefficients and describe how these parameters behave for all different scenarios. Table 4.2 summarizes all the cases that will be analyzed in this test case.

Table 4.2: Test Matrix for Test Case 2.

θ_c [°]	Chemical Comp.	η [°]	$\frac{A_{flap}}{A_{main}}$ [%]	Altitude [km]	Velocity [km/s]	Temperature [K]	Pressure [Pa]	Density [kg/m ³]
60	A/B	40	5	130	29	120.3	145	378
		50						
		60						
		70						
		80						
45	A/B	40	5	130	29	120.3	145	378
		50						
		60						
		70						
		80						

4.2 Computational framework

For both these test cases different meshes will be considered for the two different capsule designs studied. However, since the flow around the body differs depending on either the capsule's geometry or the trajectory point being studied, not all meshes (for the same geometry) will have the same upstream boundary. Depending on whether the shock front is closer or farther from the wall, the mesh is chosen to be distant enough to capture this shock, but also not too distant as to not have unnecessary cells computed in the freestream, and thus, reducing the code's efficiency.

As mentioned before, the chosen mesh consisted on a structured mesh of 70x60, yielding 4200 cells. This layout allowed achieving sufficient accuracy for computing the convective wall heat fluxes. However, for the radiative study using Spark LbL, this layout is too memory intensive, which is why every solution was also computed for a 50x60 mesh with 3000 cells. This layout will only be used for computing the radiative heat flux. Before adopting this option, an exercise was made to confirm the low influence of the number of normal cells to the final result (radiative wall heat flux), using the tangent slab approach. The results showed a difference smaller than 1% for both capsules with the chemical composition B (with CH_4) and around 2% for the composition A (without CH_4), confirming the aforementioned assumption.

4.2.1 Computational Domain

The computational domain was extended beyond the end of the capsule's shoulder, to account for the hypothetical location of the trim tabs (considered for Test Case 2). Even though these cells at first sight could seem not useful for Test Case 1, they still have their usefulness. Since the Ray Tracing model computes the wall heat from all the visible rays, shortening the domain to the limit of the shoulder would underestimate the radiative wall heat in these last wall points since the downstream vicinity of these points would otherwise lie outside the computational domain.

Also, even though the cornering of the shoulder is not being considered for the solutions, this should not affect the results significantly as long as the sonic line reattaches to the body before the shoulder (which is the case for both capsule configurations for the Entry TP, shown in Figure 4.1). This makes the expansion modeling not required if one only cares for the body's front solution. This procedure avoids the huddles related to instabilities that would arise if the expansion in the shoulder was considered and computed. In this case, ignoring the strong flow expansion, the conical region may simply be extended with no impact on the forebody flowfield [53]. While doing so, one may use the same flowfield solution for the sweeping area beyond the shoulder for accounting, or not, the flap, and just ignore the part below the shoulder if the flap region is not being analyzed. However, for Aerocapture TP $\theta = 60^\circ$ this sonic line attachment does not occur and the results lose their validity. More details are presented in §4.4.2.2.

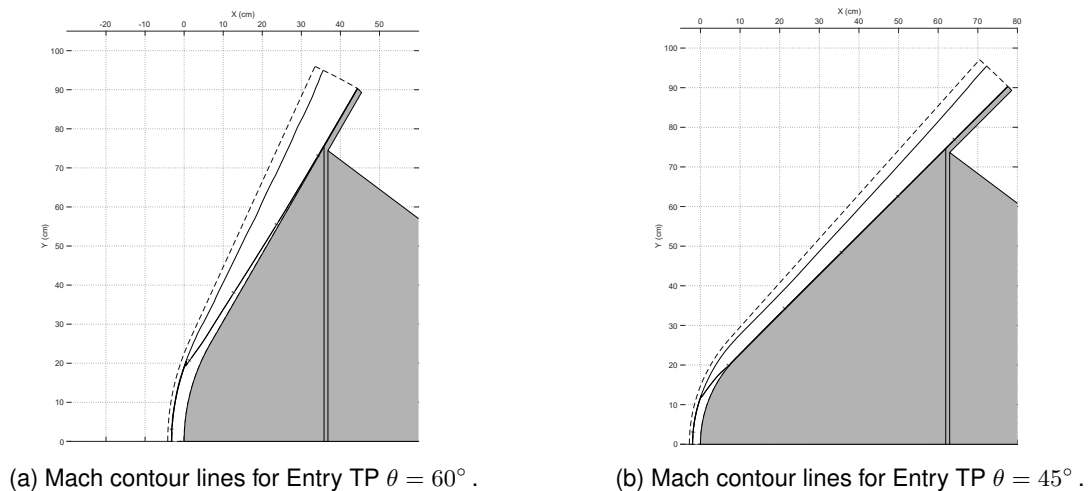
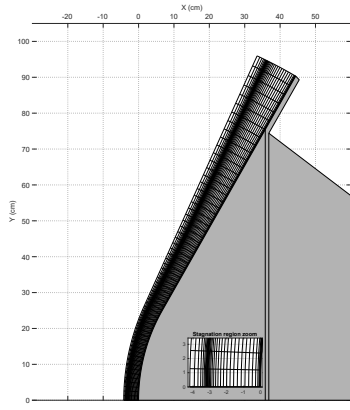
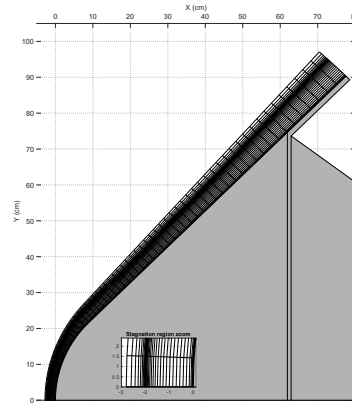


Figure 4.1: Sonic lines and shock line.

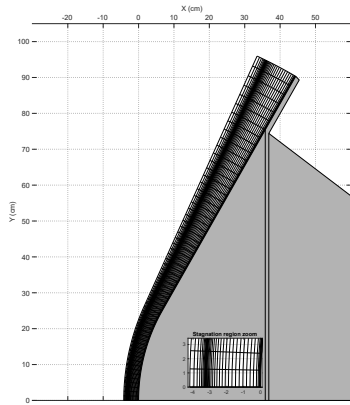
The domain covered by the meshes also varies for each case, since depending on the capsule geometry and the upstream conditions considered, the shock front will be located at different distances from the wall, as seen in Figure 4.2. This means that for each case, while computing the first solutions without refinement, one should overestimate the distance of the shock to the wall. After having an adequate estimation, right after the first refinement, the mesh was shortened to include less of the freestream region and thus allow for more efficient computation of the solutions.



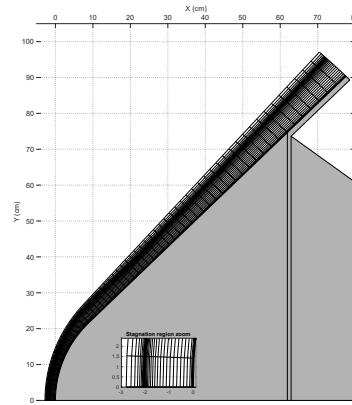
(a) Mesh for Entry TP $\theta = 60^\circ$ with CH_4 .



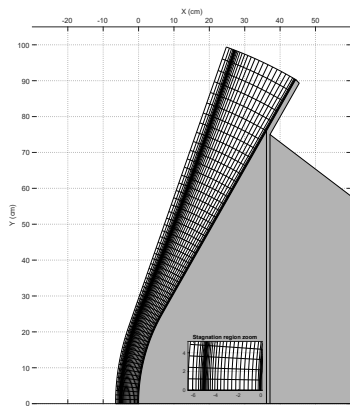
(b) Mesh for Entry TP $\theta = 45^\circ$ with CH_4 .



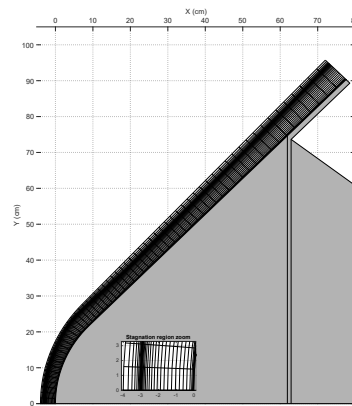
(c) Mesh for Entry TP $\theta = 60^\circ$ without CH_4 .



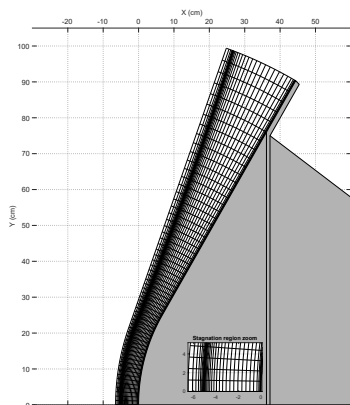
(d) Mesh for Entry TP $\theta = 45^\circ$ without CH_4 .



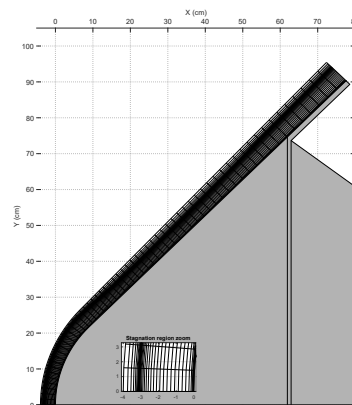
(e) Mesh for Aerocapture TP $\theta = 60^\circ$ with CH_4 .



(f) Mesh for Aerocapture TP $\theta = 45^\circ$ with CH_4 .



(g) Mesh for Aerocapture TP $\theta = 60^\circ$ without CH_4 .

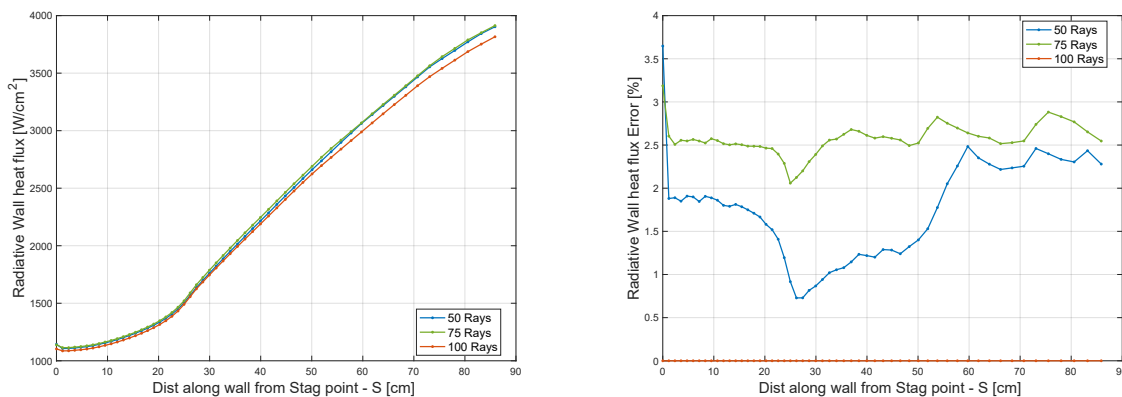


(h) Mesh for Aerocapture TP $\theta = 45^\circ$ without CH_4 .

Figure 4.2: Meshes for all cases.

4.2.2 Ray Tracing Convergence

Before choosing the number of rays per hemisphere used for the radiative analysis, some convergence tests (global and local) were carried out for a specific case using 50, 75 and 100 rays. For the global convergence the choice arbitrarily relied on the Entry TP for $\theta = 60^\circ$. As Figure 4.3 shows, there is a marginal difference when increasing the number of rays reaching a maximum error of 3.5% but having an average value below 2%. However, this increment adds a significant additional time for the Ray Tracing procedures computation as will be shown in Table 4.4. In view of this, remaining Ray Tracing procedures were performed with 50 rays per hemisphere.



(a) Radiative heat flux for different number of rays per hemisphere. (b) Error in radiative heat flux for different number of rays per hemisphere.

Figure 4.3: Convergence study on number of rays per hemisphere for Radiative Study - Entry TP for $\theta = 60^\circ$ with CH_4 .

Using another case that requires less computational times (Aerocapture TP $\theta = 45^\circ$ without CH_4 , for example), the convergence study was also performed locally, only analyzing the Radiative Heat in the Stagnation Point for a greater number of points. The results are presented in Table 4.3.

Table 4.3: Convergence Study for Ray Tracing for Stagnation Line - Error compared to 1500 rays case.

Number of Rays	50	75	100	150	200	250	500	750	1000	1500
Error [%]	2.36	3.31	-0.66	1.10	-0.03	0.23	0.58	0.33	-0.31	0.00

The analysis for these ray convergence studies leads to the following conclusions: one may assume that there is a low error when considering only 50 rays for the remaining radiative study, since these errors remain clearly below 4% over the whole domain (compared to 100 rays) and below 3% locally in the stagnation point (compared to 1500 rays).

4.3 Run Time Considerations

4.3.1 CFD Solver - SPARK

It is not easy to establish a time-frame for computing a final CFD solution since it is divided in many steps, varying from case to case. Starting from a non-refined mesh to a solution sufficiently accurate to allow the mesh refinement requires several hundreds of thousands iterations with typical CFL numbers varying between 0.01 and 5. After this mesh refinement, even with a restart from the previous field, a few hundreds of thousands iterations are again required. The most time/iterations consuming this convergence process occurs at the boundary layer level, in view of the low speeds in this region. The process is also slowed down since this boundary layer is not well enough defined in the first converged calculations where the mesh is too coarse before any refinement.

For some cases the mesh refinement needed to be adjusted (either to correct the boundary layer - first cell height - or the shock position) after the first try, which would require to perform another few hundreds of thousands of iterations to get the new field solution. Also, the cases could not be computed all at the same time, since it took a significant computational effort for each one of them, and the computer used for computations was being shared with other students.

For these reasons, it is hard to accurately estimate the time needed for a specific solution to be achieved.

4.3.2 Radiative Solver - SPARK LbL

The SPARK LbL procedures were approximately all the same regardless the case being computed. Some factors did influence the time needed to find a solution. These factors were either data size of a single cell (which could vary between 10MB and 40MB, resulting in a global radiative field between 50 to 90 GB) which would influence the time required for reading all cells' information; or the amount of threads available for the parallel runs on the Radiation Transfer Model. Clearly, radiative transfer routines are limited by I/O operations and the handling of large datasets.

Taking into consideration the Structure represented in Figure 3.1, we can summarize the time-frames as depicted in Table 4.4, considering the maximum time of each case - the worst case scenario.

Table 4.4: Run Time for the Radiative Solver for the different Modules for 50x60 Meshes and 50 rays (worst case scenario).

Chemical Composition	Excitation Module	Radiative Module	Radiation Transfer Module		
			No Interp.	Linear Interp.	
A (with CH ₄)	00h02m	31h10m	50 Rays :	01h50m	19h30
			75 Rays :	03h40m	—
			100 Rays :	04h50m	—
B (no CH ₄)	00h02m	05h10m	50 Rays :	01h50m	

4.4 Test Case 1

This test case's results were based on the radiative and convective heating at the wall for each of the 8 cases. After computing them, one can gather the results into different groups, analyzing individually either the capsule's design, the chemical composition or the trajectory point.

There is not much in the literature than may be found for comparison purposes, except for the capsule with $\theta = 60^\circ$ for the Entry TP and $\theta = 45^\circ$ for the Aerocapture TP. The similarity in the nose radius and in the freestream properties for these particular cases were similar to ESA's CDF Study for the first TP, and from Hollis *et al.* [10] and Park's studies ([5] and [6]) for the second one.

4.4.1 Entry Trajectory Point

4.4.1.1 Stagnation Line analysis

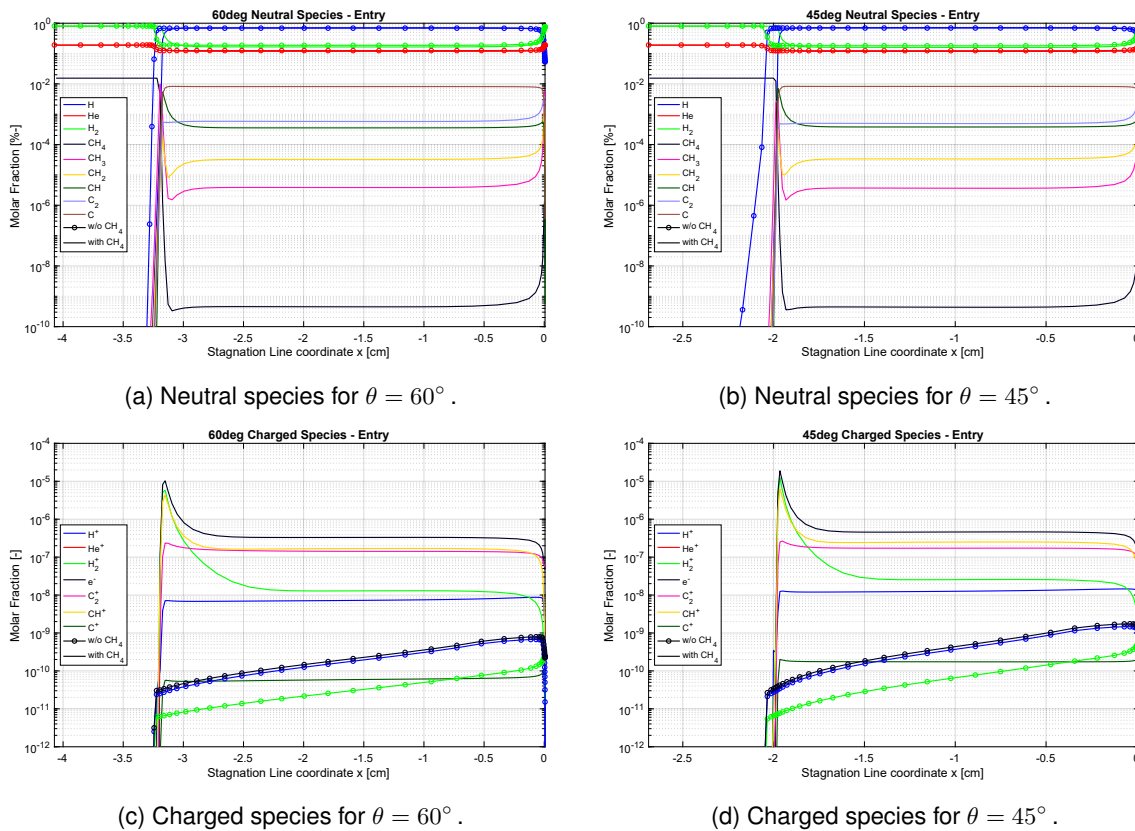


Figure 4.4: Chemical species along Stagnation Line for Entry TP.

Regarding the evolution of the species in the stagnation region, there are some expected behaviors depicted in Figure 4.4: For the chemical composition A (with CH_4) the formation of C, CH_2 and CH can be highlighted, with C reaching molar fractions in the same order of magnitude of CH_4 pre-shock. This formation of carbonaceous species results from the dissociation of CH_4 (and further dissociation of the dissociation's products) due to the high post-shock temperatures of particular importance is the steady state concentration of C_2 , which reaches $\sim 10^{-6}$. As we will see in the next section, this will significantly

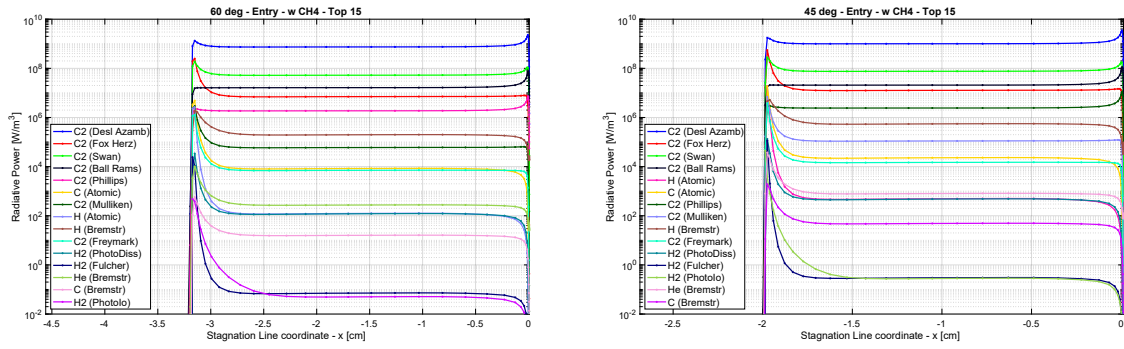
impact radiative heating for the flow. Also there is an peak in the concentration of electrons in the shock, also expected from this region's typically high temperatures, which allows ionization reactions to occur. These electrons will later interact with other species until equilibrium is reached. Finally, since the implemented wall boundary condition is a fully catalytic one, upon reaching the wall boundary, there is an increment on the molar fraction of the molecular neutral species, consequence of their recombination. This recombination is also enhanced by the temperature drop within the boundary layer that enhances the formation of the molecular species. The charged species also interact with the free-electrons in the field, allowing for recombination into neutral species (which is the case of He^+ , H^+ and H_2^+ which form He and H_2 ; for the composition A, there is also recombination of C_2 , CH_4 , CH_3 and CH_2).

In both configurations ($\theta = 60^\circ$ and $\theta = 45^\circ$) the chemical evolution is very similar, and the only significant differences are in the distance of the shock to the wall, around 3.4 cm and 2.0 cm respectively. this distance is related to the nose radius, which justifies these distinct values. There is however a shift on a few mm of the shock front comparing both compositions A (with CH_4) and B (without CH_4).

This evolution matches the one previously described roughly in section §1.2.

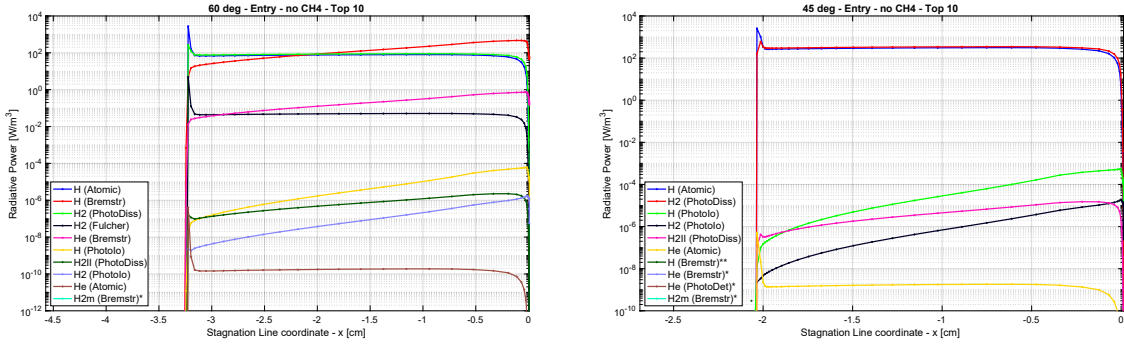
Giving attention to the radiative power of the different radiative systems (see Figure 4.5 which plots the emissivity of each radiative systems over the stagnation line), there is again a similarity between both capsule configurations, varying mostly in regards to the position of the shock only. Concerning the influence of the presence of CH_4 there is a significant change: the systems involving carbonaceous species (carbon molecular or carbon atomic) become the dominant systems, with radiative powers higher than those from He and hydrogenoid species by several orders of magnitude. Here the presence of C_2 at high temperature in the whole post-shock flow, significantly enhances molecular radiation. This is not surprising, since C_2 is known to be a strong radiator (like CN for Earth entries), and even the presence of trace amounts of C_2 will lead to noticeable radiation.

Regarding the temperature in the stagnation line, Figure 4.6, there is a larger shock when CH_4 is considered, with this phenomenon being present for both geometries. Also, there is a higher peak temperature in the shock, with a peak temperature increment in the order of 145% for both cases. For both capsule designs the peak temperature is very similar for both chemical compositions. Also, the temperature at which the flow reaches the equilibrium is also very similar between the 4 cases, although there is a small increment for $\theta = 45^\circ$, and also when considering CH_4 . The shock position can be defined as the position where the flow achieves peak temperature. When considering CH_4 , the distance between the shock and the wall is 3.15 cm and 1.96 cm for $\theta = 60^\circ$ and $\theta = 45^\circ$. Finally, there is a shift in the shock distance to the wall for both cases, even though the exact location of the wall is difficult to pinpoint since the shock is different for each chemical compositions. Considering the shock position as the location at peak temperature coordinate, the shock gets closer to the wall 0.07 cm and 0.08 cm respectively for $\theta = 60^\circ$ and $\theta = 45^\circ$.



(a) Top 15 radiative systems for $\theta = 60^\circ$ with CH_4 .

(b) Top 15 radiative systems for $\theta = 45^\circ$ with CH_4 .



(c) Top 10 radiative systems for $\theta = 60^\circ$ without CH_4 .

(d) Top 10 radiative systems for $\theta = 45^\circ$ without CH_4 .

Figure 4.5: Radiative Power along Stagnation Line for Entry TP.

* Not shown in the window at all

** Not shown in the window in the equilibrium region

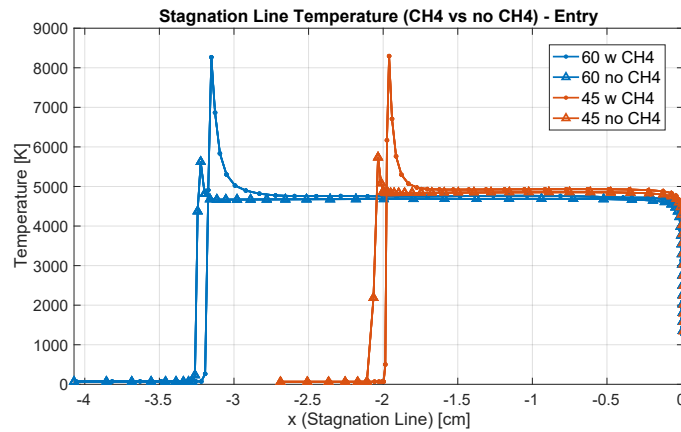


Figure 4.6: Stagnation Line Temperature - Entry TP.

4.4.2 Aerocapture Trajectory Point

4.4.2.1 Stagnation Line analysis

Globally, this trajectory point yields a similar chemistry to the one described earlier for the Entry TP. However, since the temperature increment in the shock is higher than the previous one, there are additional phenomena present, shown in Figure 4.7.

Starting with H_2 there is a significant increment of dissociation compared with the Entry TP. The equilibrium was previously achieved with a molar fraction of around 10^{-1} and now it is around 10^{-5} for both compositions (A and B). This is not surprising in the view of the higher temperatures. Molecular carbonaceous species display the same behavior, with a significant decrease in the molar fractions. Here however, there is a clearer peak in some molar fractions in the shock region particularly the C_2 molar fraction. This species previously did not present a significant peak, whereas here we achieve molar fraction values around 10^{-5} in the shock region, with steady-state concentrations around 10^{-9} . Helium also present a small reduction in the equilibrium molar fraction due to the higher temperatures felt for this trajectory point, which enhances the ionization degree of the flow occurring.

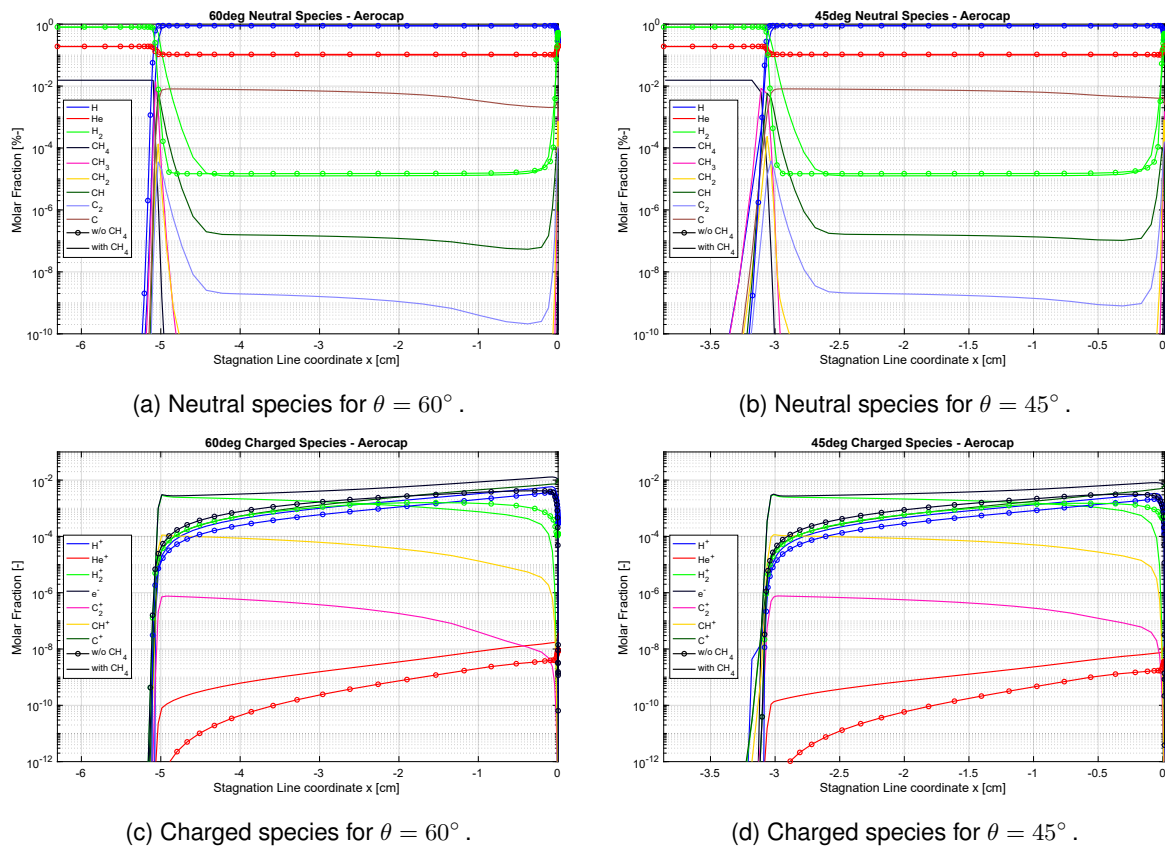
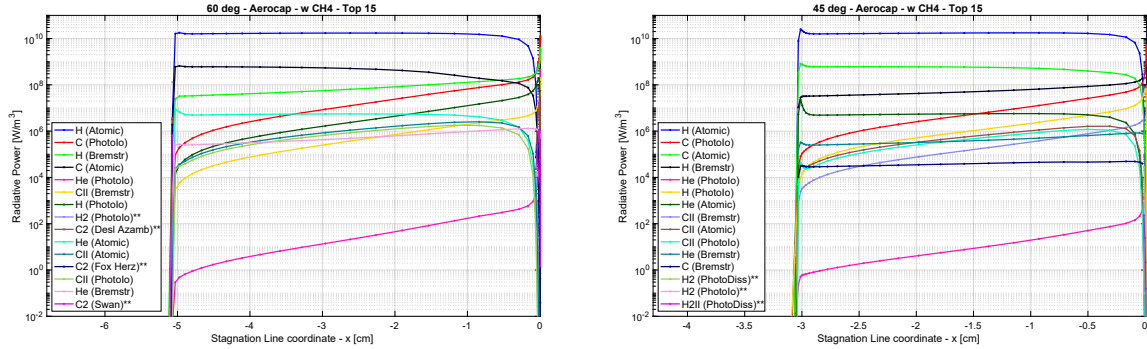


Figure 4.7: Chemical species along Stagnation Line for Aerocapture TP.

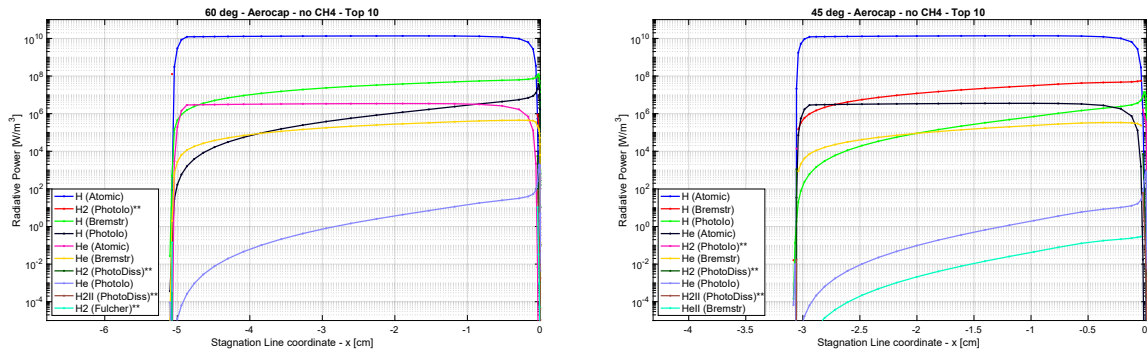
Looking now to the radiative power along the stagnation line, Figure 4.8, there are several differences that must be highlighted. The dominance of the C and C_2 radiative systems is no longer present, with the radiative system from H Atomic lines dominating along the stagnation line. Again, the increase in the temperature post-shock has a significant role in how the chemical species and consequently, the radiative systems evolve along this line. The influence of the carbonaceous species is no longer critical regarding radiation, since even for the composition B (without CH_4), there are several radiative systems from hydrogen that achieve radiative powers above 10^6 W/m^3 with the atomic lines reaching 10^8 W/m^3 for the majority of the post-shock region. For this trajectory point, Aerocapture TP, the composition B encompasses 5 radiative systems with radiative power above the 10^0 W/m^3 mark, with all of them achieving values higher than 10^5 until reaching the boundary layer, whereas in the Entry TP only two

radiative systems achieved values higher than 10^{-3} W/m^3 along the stagnation line, and none achieved the 10^4 W/m^3 mark. Even the radiative system from the He Atomic lines have now a significant influence, reaching values higher than 10^6 W/m^3 in the equilibrium region (previously, its influence was around 10^{-9} W/m^3 , with a peak value in the shock region below the 10^{-6} W/m^3 mark).



(a) Top 15 radiative systems for $\theta = 60^\circ$ with CH_4 .

(b) Top 15 radiative systems for $\theta = 45^\circ$ with CH_4 .



(c) Top 10 radiative systems for $\theta = 60^\circ$ without CH_4 .

(d) Top 10 radiative systems for $\theta = 45^\circ$ without CH_4 .

Figure 4.8: Radiative Power along Stagnation Line for Aerocapture TP.

* Not shown in the window at all

** Not shown in the window in the equilibrium region

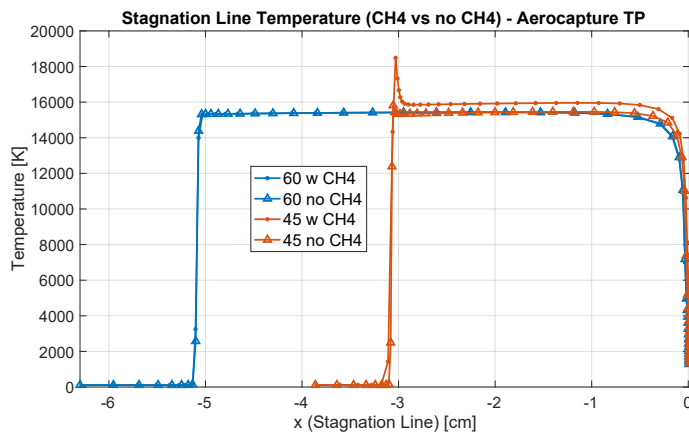


Figure 4.9: Stagnation Line Temperature - Aerocapture TP.

For the Aerocapture TP, there is a significant increase in the post-shock temperature, reaching values above 15,000K, see Figure 4.9. There is however no significant difference in these properties between

chemical compositions. For $\theta = 45^\circ$, there is a peak temperature in the shock, whereas for $\theta = 60^\circ$ it quickly reaches a steady state temperature, without the typical post-shock overshoot. A possible explanation is the lack of sufficient grid refinement in the shock region as a consequence of the considerably longer shock standoff.

There is also no significant changes regarding the shock position between the two chemical compositions with and without CH_4 .

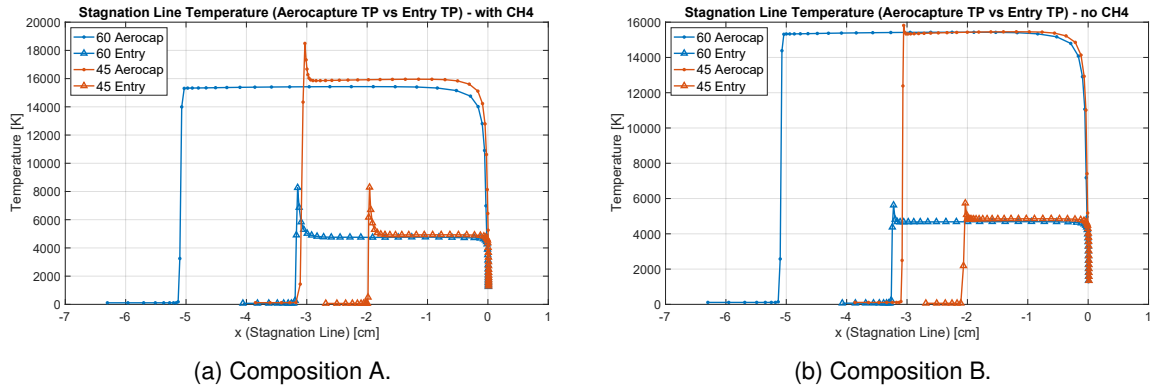


Figure 4.10: Comparison based on Trajectory Point - Stagnation Line Temperature.

Figure 4.10 allows for the comparison between both trajectory points. What is most evident is the difference between post-shock temperatures, with those in Entry TP being very lower than those in Aerocapture TP. This may be explained by the significant difference in the freestream velocity (from 18 km/s to 29 km/s) and consequently, the Mach Number (from 32 to 39) which in turn lead to significantly higher temperature ratios in the (approximated) normal shock in the stagnation region, as the shock is more intense for the Aerocapture TP.

We may also note the change in the shock position, with the shock locating itself farther from the wall for the Aerocapture TP, as the shock standoff increases by about 150% for $\theta = 45^\circ$ and around 166% for $\theta = 60^\circ$.

4.4.2.2 Sonic line transition

A unexpected result for the case of Aerocapture TP with $\theta = 60^\circ$ is reported. Focusing on the sonic line, there is an uneven shape for the flow (Figure 4.11a), with the sonic line going back to the shock region, without an attachment to the capsule before the shoulder, contrarily to what usually happens (this attachment is present on the Entry TP for $\theta = 60^\circ$ and for both TP for $\theta = 45^\circ$). There is now a wide subsonic region resulting in the shock being significantly farther to the wall comparing to the other cases, widening significantly the domain. Note that this happens for both chemical compositions, and thus, is not a predominantly chemically related problem.

Since the flow in the outlet is now subsonic, the assumptions made in §4.2.1 of not needing to compute the flow in the shoulder region are no longer applicable. There was not enough time to try to compute the solution considering the shoulder and its expansion, and from the work Fernandes [7, 53] we also know that this is an extremely difficult region to model with CFD owing to the abrupt expansion

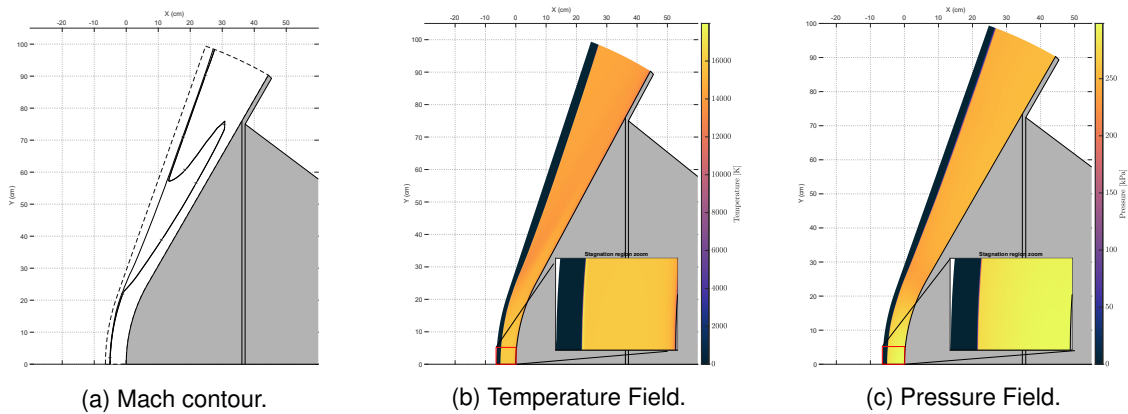


Figure 4.11: Abnormal results for Aerocapture TP $\theta = 60^\circ$ (with CH_4).

of the flow. Instead we focused on performing a series of sanity checks for this unexpected result.

Some of the attempts made to double check this result consisted on widening the computational domain, changing the points distribution in the tangential direction to the wall, increasing the imposed wall temperature (T_w), slightly changing the freestream pressure and density, and finally solving the Euler equations instead of the Navier-Stokes equations. Yet, in every one of these attempts, the same (or similar) result was achieved, even when starting from an "empty result" (instead of using a restart from a previous flow field).

With all the cross-checks terminated this result was no longer deemed a numerical error, and a further literature research was conducted to achieve some understanding for this phenomena. Gnoffo [54] performed a review of planetary entry gas dynamics for different missions and capsule shapes, and using the Mars Pathfinder mission as an example, similar phenomenon as the one aforementioned is reported. Increasing the cone angle θ_c more than a particular value θ_s (dependent on M_∞ and effective specific heat ratio $\gamma_{eff} - \gamma$ that recovers the density ratio across the shock) the sonic line attachment at the wall migrates from the nose region towards the shoulder region. South [55] studied this phenomena in 1968, and built relations to obtain θ_s as a function of γ and M_∞ . More recently, in 2019, Hornung *et al.* [56] also provided a study regarding this phenomenon.

For $\theta_c < \theta_s$, the sonic line sits over the nose, as is the case of $\theta = 45^\circ$ in this work for both TP, and the sonic line attaches to the body before the conical region (or in its early phase).

For $\theta_c > \theta_s$, the sonic line sits over the aft corner near the shoulder, as a consequence of the following compression located therein. In this work, the domain does not include the expansion in the shoulder region and this late attachment is not depicted, even for large θ_c . If this region was also included, the expansion of the flow would accelerate it, making the sonic line attach itself to the capsule body in the aft corner region.

For $\theta_c \approx \theta_s$, the sonic lines skirts with the outer edge of the boundary layer over most of the cone. This is what happens in this work for $\theta = 60^\circ$ in Entry TP, see, for example, Figure 4.1a.

South reports $\theta_s = 55^\circ$ for $\gamma=1.4$ (at large Mach numbers - $M_\infty > 10$). Nonetheless, the γ_{eff} is only equal to γ_∞ for a perfect gas. Checking Figure E.10 in Appendix E, a post-shock γ at the beginning of the conical shape may be approximated to 1.6 in the majority of the cases. Extrapolating from South

data (Figure E.11), this γ yields in $\theta_s \approx 48^\circ$. (This is a poor extrapolation, and the correct way would include solving the detailed equations described in [55, 56].)

To confirm this estimation, simulations for Aerocapture TP were performed with chemical composition B and without any type of mesh refinement (resulting in lower computational times) for θ_c varying from 45° to 61° , keeping the nose radius constant to the one used firstly for $\theta_c = 60^\circ$, $r_n=0.5\text{m}$. Figure 4.12 presents the different sonic lines for some of these cases (Figure E.9 in Appendix E present the results for all cases). The sonic line moves away from the wall at the nose region for $\theta_c \approx 50^\circ$, which is close from the first estimation made. However, at $\theta_c = 46^\circ$ the flow starts to evidence a small bubble that grows with θ_c until it reaches the sphere-cone interface (at $\theta_c = 50^\circ$). For larger angles, the sonic line is moving towards the shoulder until it fully detaches and joins the shock. Nevertheless, if sufficient refinement was included to properly capture the boundary layer, the sonic line would not join the wall but instead would merge into the boundary layer. Future work would ideally also include both this refinement to further describe this phenomenon in a more detailed manner.

This result presents some useful information also for Entry TP. For $\theta = 60^\circ$ in Entry TP, the flow is already experiencing this change in the sonic line attachment to the wall towards the shoulder. However, this did not reflect in differences as critical as for Aerocapture TP. Nevertheless, this deeper analysis helped identifying possible instabilities in this capsule geometry for both TP. Small changes in the angle of attack through the capsule trajectory may reflect in aerodynamic instabilities of the sonic line shifting from the shoulder to the nose cap and back again¹. This is reported in [54, 57] for the Mars Pathfinder configuration, which consisted in a 70° sphere-cone configuration.

The unusual sonic line shape presented in this work (see, for example, Figure 4.11a), may reflect a phenomenon similar to the one depicted in [54] where a type of bubble is shown as the sonic line transits from the nose towards the shoulder. This is reported here in Figure 4.13. For the cases studied in this subsection, the beginning of the sonic line transition is around $\theta_c = 48^\circ$ whereas the sonic line is fully established in the shock region for $\theta_c = 61^\circ$. However, these results might be slightly different, particularly the latter, if the aft corner was considered in these computations for the aforementioned reasons. The expected result would be something as the "corner" one described in Figure 4.13.

For the sake of completeness, the analysis for this case was kept in this work, even though several assumptions previously no longer stand under this unanticipated phenomenon. One such example is ignoring the expansion in the shoulder. Another one concerns the presence of the trim tab: as the flow starts to be subsonic in this region, there is a strong influence of the flow around the flaps towards upstream, which would significantly change all the results here presented, and as it stands, these are poorly physical. 3D simulations would need to be performed to correctly represent the phenomena here described as it influences the efficiency of the trim tab. Wider domains, including the aft corner should also be chosen.

¹Since changes in angle of attack are akin to an increase of the cone angle on one side and an identical decrease on the other side.

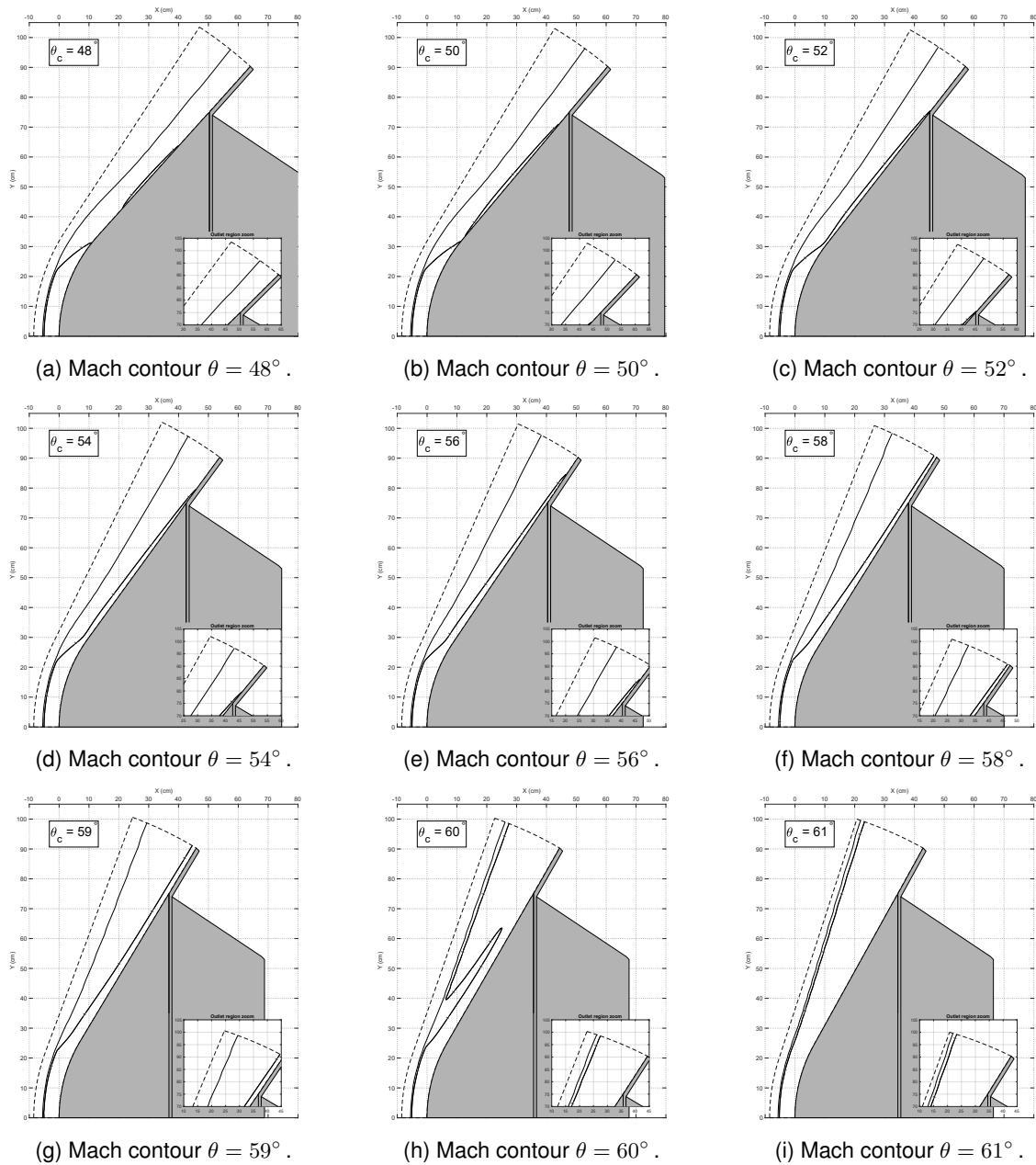


Figure 4.12: Sequential distancing of the sonic line from the nose cap towards the shoulder.

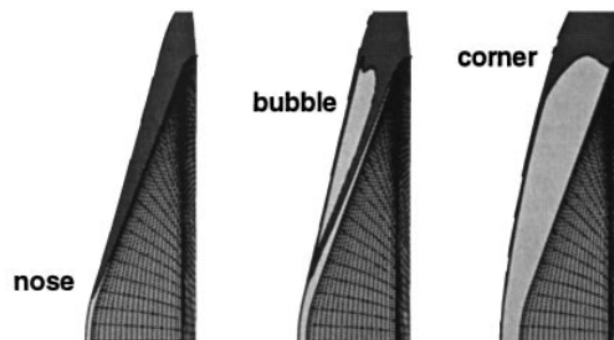


Figure 4.13: Mars Pathfinder Mach field from Gnoffo [54]. Darker regions are supersonic zones behind the bow shock.

4.4.3 Wall Heating

4.4.3.1 Convective Wall Heat Fluxes

This subsection analyses the computed wall heat fluxes.

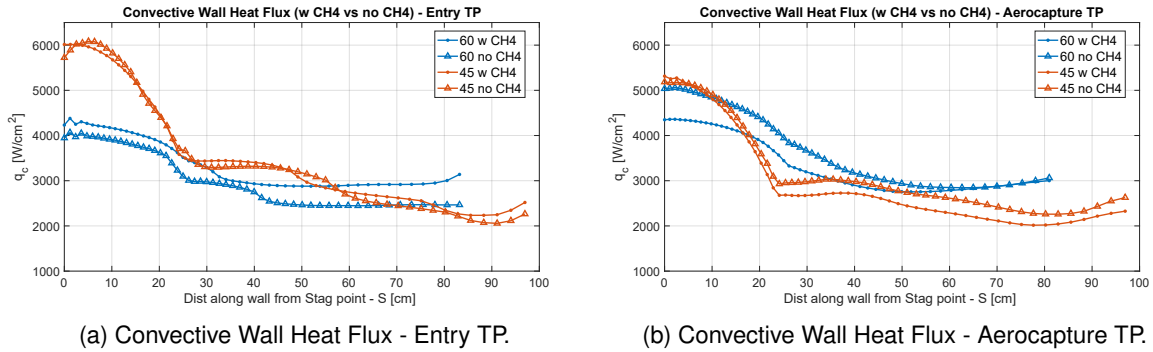


Figure 4.14: Comparison Convective Heat Flux based on Chemical Compositions.

Starting with the analysis for the Entry TP, the chemical composition does not change significantly the convective heat flux profiles in each capsule design, see Figure 4.14a, where is a good match for when comparing the heat flux profile for $\theta = 45^\circ$ with and without CH_4 . For $\theta = 60^\circ$ both results have a similar shape, but with a small shift for the case without CH_4 . Note also the fact that it seems to be presented some instabilities in the convective heat flux at the stagnation point region, possibly born due to very small carbuncles not identified in the flow field at the naked eye. The peak heat flux, occurring in the stagnation line, is significantly larger for the capsule with $\theta = 45^\circ$ with heat fluxes around 150% higher compared with $\theta = 60^\circ$. This is an anticipated result. For the conical shape (after the nose region, for $S > 0.3\text{m}$), the differences are less marked, with the heat fluxes for $\theta = 45^\circ$ being even smaller than $\theta = 60^\circ$ near the shoulder region.

For the Aerocapture TP, Figure 4.14b, there are again higher values of the wall hear flux for composition A, more significant for $\theta = 60^\circ$. For $\theta = 45^\circ$, this increase is not very significant, with the results presenting a very similar shape for both chemical compositions. The comment made previously regarding the heat flux being significantly higher in the nose region for $\theta = 45^\circ$ is no longer true, with $\theta = 60^\circ$ presenting similar values to $\theta = 45^\circ$ when CH_4 is considered.

We now compare the Entry TP and Aerocapture TP convective heat fluxes, for $\theta_c = 60^\circ$ and $\theta_c = 45^\circ$ capsules. Figure 4.15 provides the comparisons with CH_4 (left) and without CH_4 (right).

There is a very similar convective heat flux profile in both trajectory points. For the Entry TP, the heat flux profile presents higher values in the order of 700 W/cm^2 in the nose region compared with Aerocapture TP. The heat fluxes shape is mostly similar among both TP, with the exception of the end of the conical shape, right before the shoulder, where there is a small decrease followed by an increase of the convective heat flux in the Entry TP. The Aerocapture TP only shows the latter increment, with no sudden decrease in the convective heat flux.

Regarding $\theta = 60^\circ$, there are different behaviors on the heat profile between Trajectory Points depending on the chemical composition. With CH_4 , there is almost a perfect match, with the convective

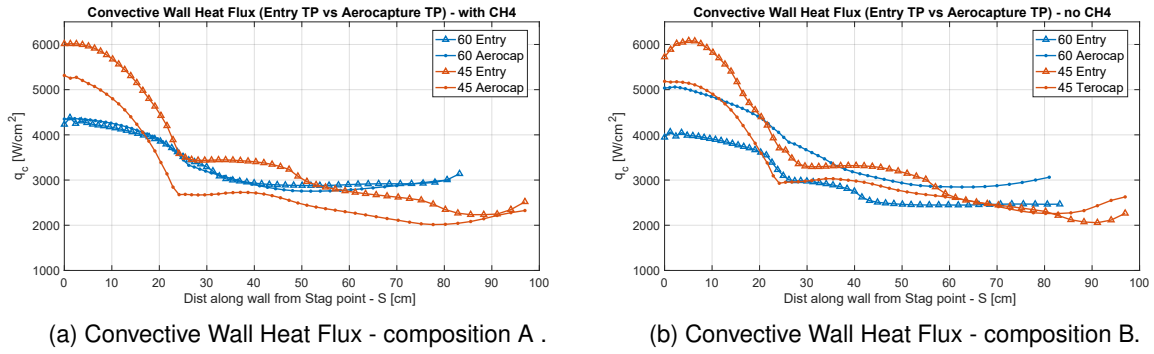


Figure 4.15: Comparison Convective Heat Flux based on Trajectory Point.

heat fluxes presenting very similar results for both TP's. On the other hand, without CH_4 , both TP's convective heat fluxes present significantly different results, with the Aerocapture TP heat flux values being around 1000 W/cm^2 higher (corresponding to 125% increment) near the stagnation region. However, as we get farther from the stagnation region, the shape remains similar between both TP, with the differences stabilizing around 120% through the conical part of the capsule.

One may note that the abrupt changes in the convective heat located near $S=0.25\text{m}$ for both capsules coincides with the transition from the spherical-shape to the conical-shape. As discussed in Chapter 3, the mesh generator used does not implement the continuity of the second derivative of the capsule's shape in this region, which is why these results may present these irregularities.

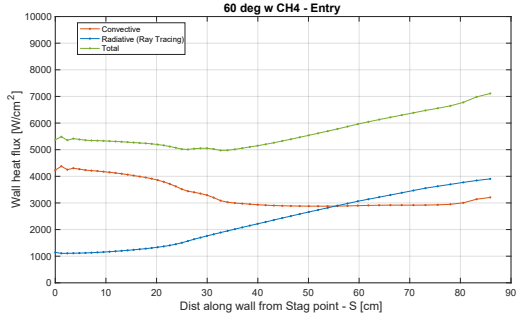
4.4.3.2 Total Wall Heat Fluxes

Here we present the global (convective + radiative) heat fluxes profiles along the capsule's wall for all cases taking into account radiative heating.

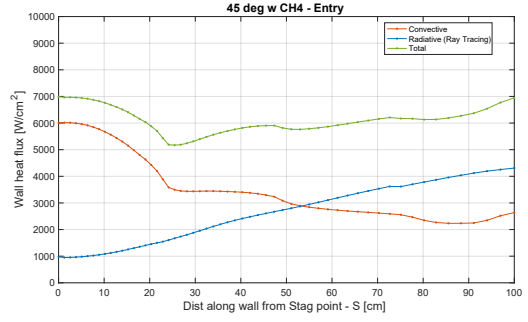
For the Entry TP with chemical composition A (with CH_4), the radiative heat flux near the stagnation point have a relative low value (only about 20% and 15% of the total heat flux for $\theta = 60^\circ$ and $\theta = 45^\circ$ respectively) but grows along the wall and reaches values around 60% of the total heat flux in the shoulder region (Figure 4.16a and Figure 4.16b). For the same trajectory but without considering CH_4 (composition B), the radiative heat flux is completely negligible for both capsule configurations. The radiative heat fluxes results are around the order of $\times 10^{-5}\%$ of the total heat flux for both capsules. This comes as no surprise since, as referred in §4.4.1.1, the radiative power along the stagnation line present values notable smaller for the chemical composition B. Figure E.1a also represents this phenomenon with the total radiative power differing from a several orders of magnitude.

Another interesting phenomenon with the evolution of the radiative heating along the wall is presented in Figures 4.16a, 4.16b, 4.17a and 4.17b. For the same chemical composition, A (with CH_4), the Entry TP shows a sequential growth of the radiative heating along the wall from the stagnation line towards the shoulder, whereas for the Aerocapture TP there is a initial peak in the nose region followed by a decrease of the radiative heating into the shoulder.

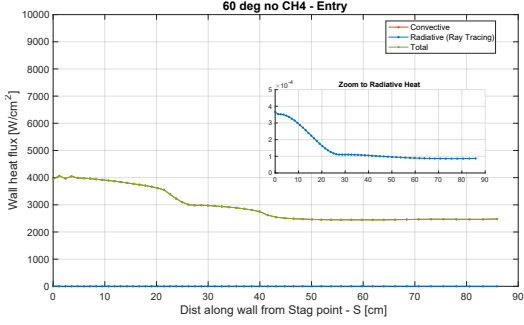
A detailed discussion of the radiative heating shape is presented next, with primary focus on the capsule design with $\theta = 45^\circ$:



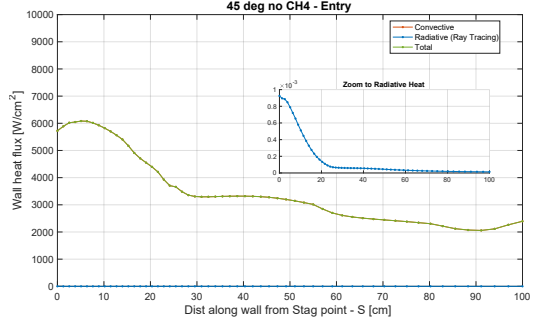
(a) $\theta = 60^\circ$ with CH_4 .



(b) $\theta = 45^\circ$ with CH_4 .

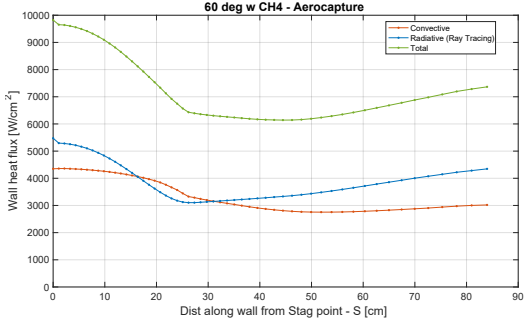


(c) $\theta = 60^\circ$ without CH_4 .

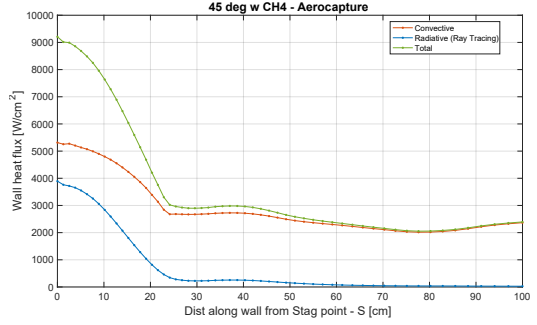


(d) $\theta = 45^\circ$ without CH_4 .

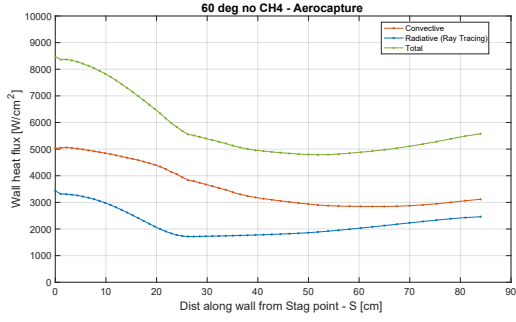
Figure 4.16: Radiative and Convective Wall Heating for Entry TP.



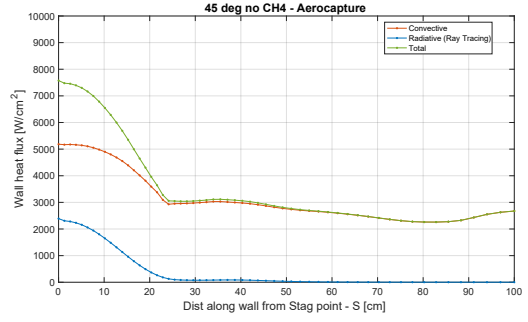
(a) $\theta = 60^\circ$ with CH_4 .



(b) $\theta = 45^\circ$ with CH_4 .



(c) $\theta = 60^\circ$ without CH_4 .



(d) $\theta = 45^\circ$ without CH_4 .

Figure 4.17: Radiative and Convective Wall Heating for Aerocapture TP.

For the Entry TP, based on the Stagnation Line evolution (Figure 4.5b), considering a chemical composition A (with CH_4), the most dominant radiative transitions belong to the C_2 species, (the top 5 systems). This species is present throughout the whole domain, with particular growth in molar fractions

as we get farther from the stagnation region (see Figure 4.19a), which yields additional radiative emissivity in this spatial region (see Figure 4.18). Figure 4.20 confirms this line of thought, with the significant contribution to the cumulative heat flux (during the spectral integration) coming from wavelengths correspondent to C_2 radiative systems. Without CH_4 (composition B), the most dominant radiative transitions come from H (Atomic). Contrarily to the C_2 for the composition A, the atomic hydrogen distribution is higher on the stagnation region, see Figure 4.19c. Figure 4.21 confirms this, with the significant contribution to the cumulative heat flux (during the spectral integration) coming from wavelengths correspondent to H atomic lines, and being more significant in the stagnation region.

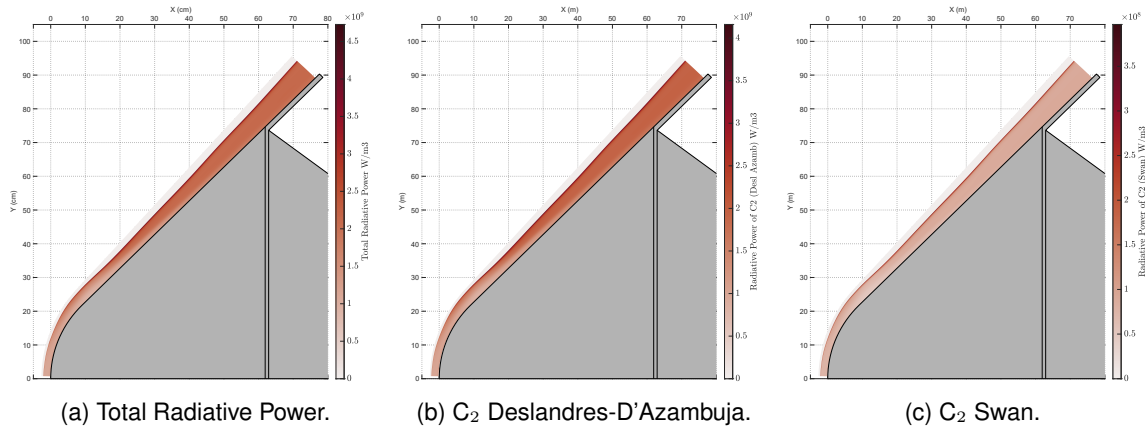


Figure 4.18: Radiative Powers for Entry TP ($\theta = 45^\circ$ with CH_4) - Total and 2 most dominant.

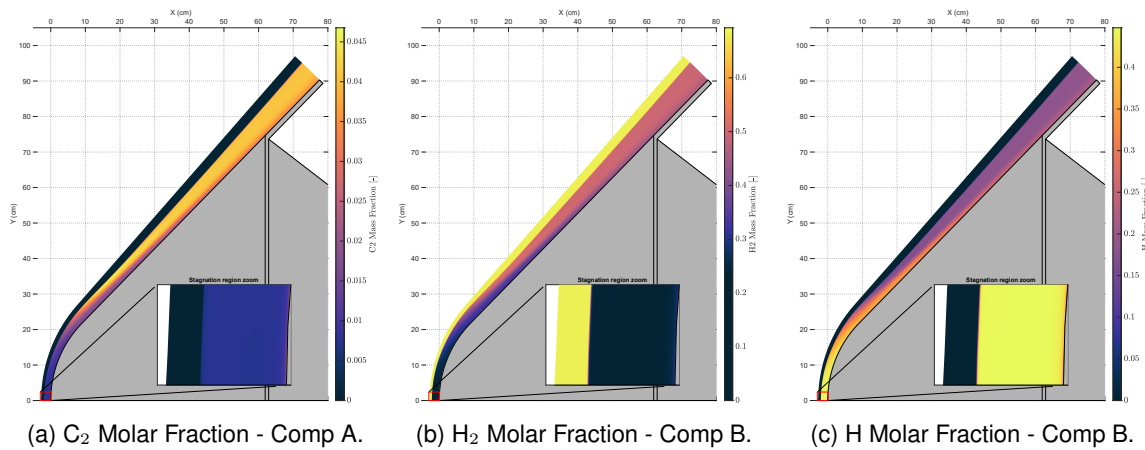


Figure 4.19: Molar Fraction of C_2 , H_2 and H for Entry TP ($\theta = 45^\circ$) in different chemical compositions.

This justifies the different shape (ignoring the difference in the magnitude) of the radiative heat flux profiles for this trajectory point for the different chemical compositions, whereas for the composition B there are larger values of radiative heating in the stagnation region.

For the Aerocapture TP, the dominant radiative systems are from H and C atomic lines, Figure 4.8b. In this trajectory point, the higher temperatures preclude the significant presence of molecules such as C_2 which is why this species is no longer dominant in the radiation. Also, as we get farther from the stagnation region, even though there is no significant change in the species molar fractions (as there was for the C_2 in the previous TP), there is a significant change in the temperature field. With the higher velocity

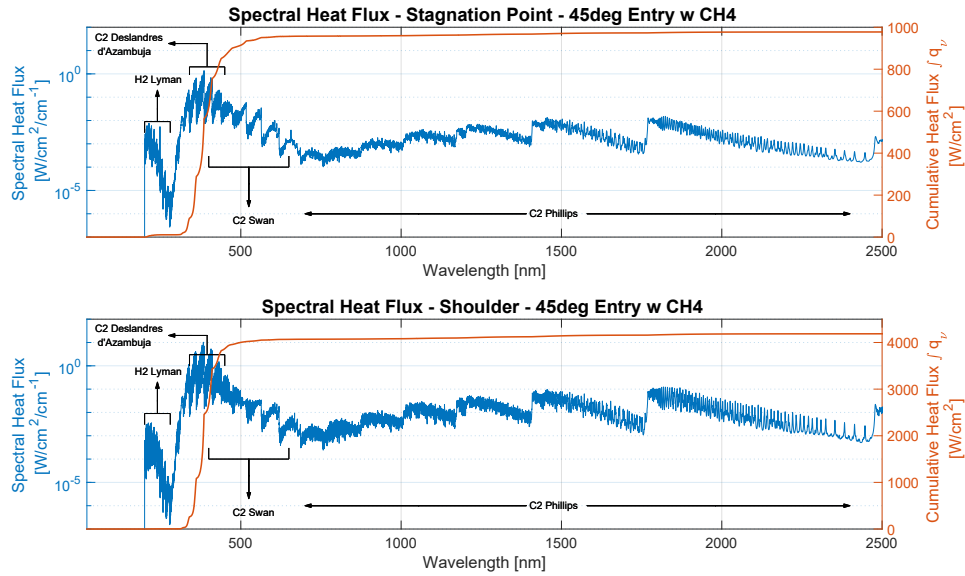


Figure 4.20: Spectral Radiative Heating for Entry TP ($\theta = 45^\circ$ with CH_4) - Stagnation Point and Shoulder.

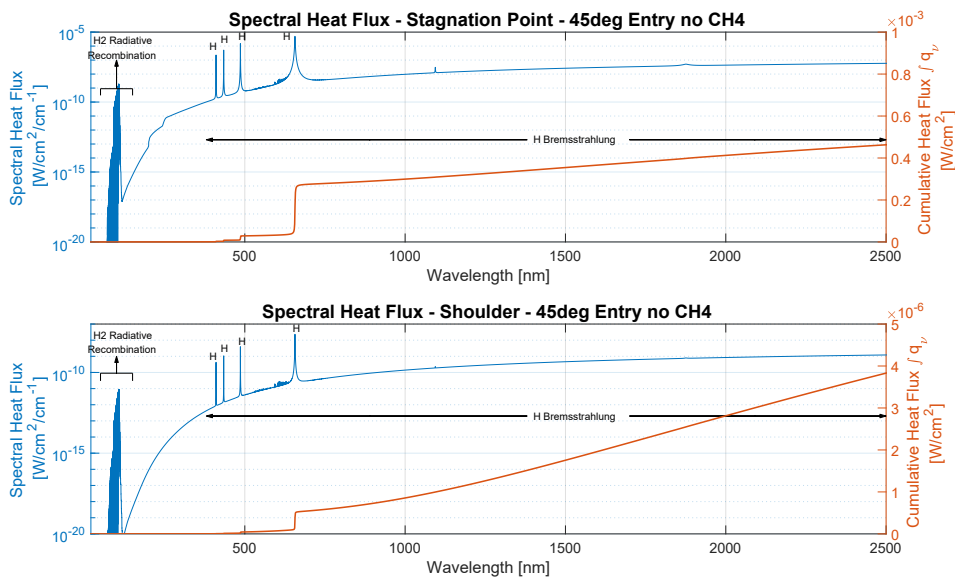


Figure 4.21: Spectral Radiative Heating for Entry TP ($\theta = 45^\circ$ no CH_4) - Stagnation Point and Shoulder.

from this trajectory point, the difference between the oblique shock and a normal shock is more crucial, which reflects in significant changes in the post-shock temperatures of the stagnation region (where the shock is close to a normal shock) and the conical part of the capsule (where the shock is closer to an oblique shock). Higher the temperature, higher the radiative power of H and C atomic radiative systems. For this reason, in the stagnation region, the radiative power will be higher, reflecting in higher radiative heat fluxes in this region. Figure 4.24 confirms this train of thought, with the significant contribution to the cumulative heat flux (during the spectral integration) coming from wavelengths correspondent to H and C Atomic Lines radiative systems. This contribution is higher in the stagnation region, where these species are at a higher temperatures, and emit more radiation. In this trajectory point, since the dominant radiative systems are from H and H_2 , there are no significant changes when considering the two

different chemical compositions (A and B) as these species are present in both of them. Figure 4.25 shows a significant difference in the spectral heat flux component (blue) compared to Figure 4.24. Most of the lines disappear since most of them corresponded to C Atomic Lines.

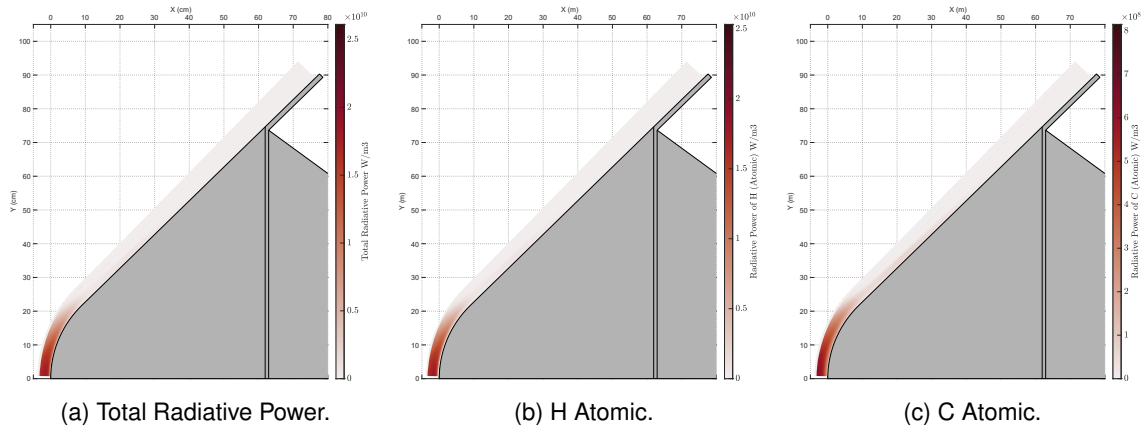


Figure 4.22: Radiative Powers for Aerocapture TP ($\theta = 45^\circ$ with CH_4) - Total and 2 most dominants.

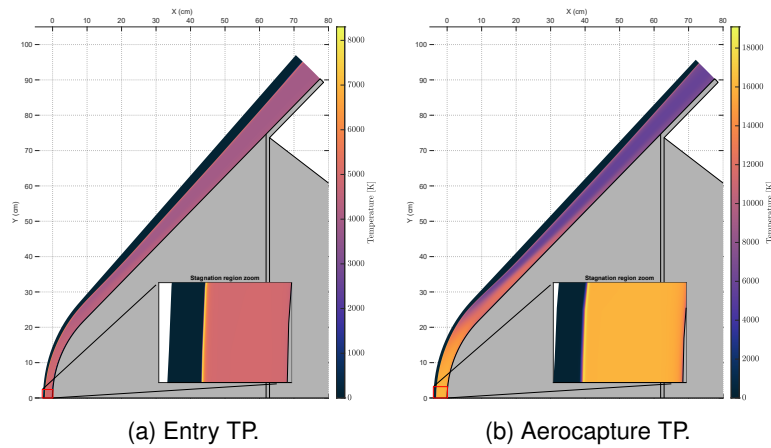


Figure 4.23: Temperature Fields for $\theta = 45^\circ$ with CH_4 .

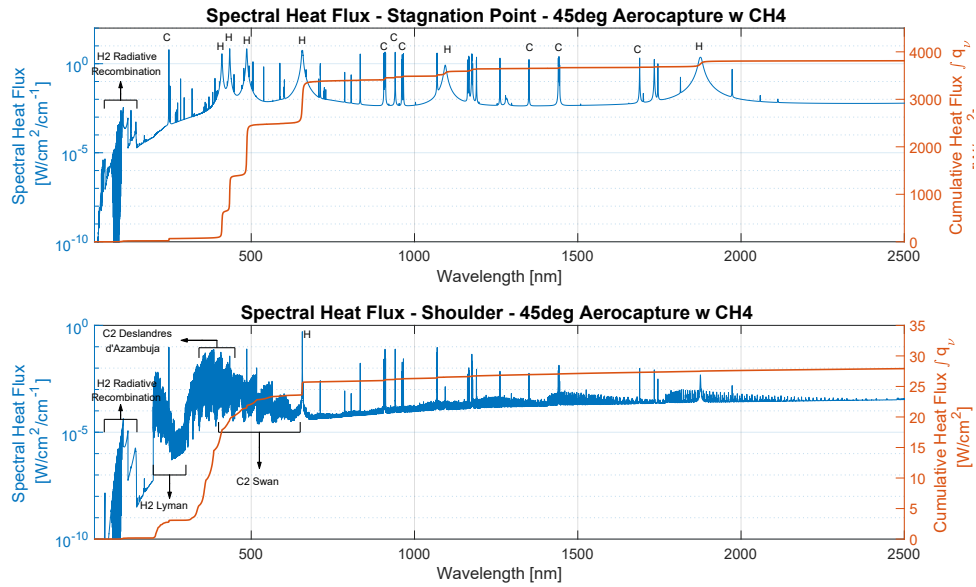


Figure 4.24: Spectral Radiative Heating for Aerocapture TP ($\theta = 45^\circ$ w CH_4) - Stagnation Point and Shoulder.

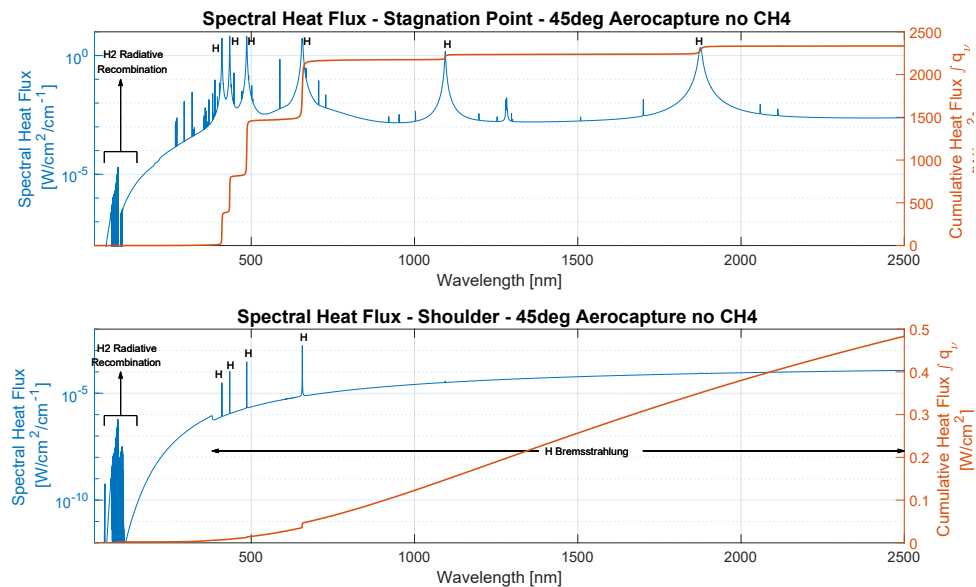


Figure 4.25: Spectral Radiative Heating for Aerocapture TP ($\theta = 45^\circ$ no CH_4) - Stagnation Point and Shoulder.

Summarily, the radiative heat flux profile's shape for both trajectory points differ because two main reasons: Temperature field and dominant species spatial distribution.

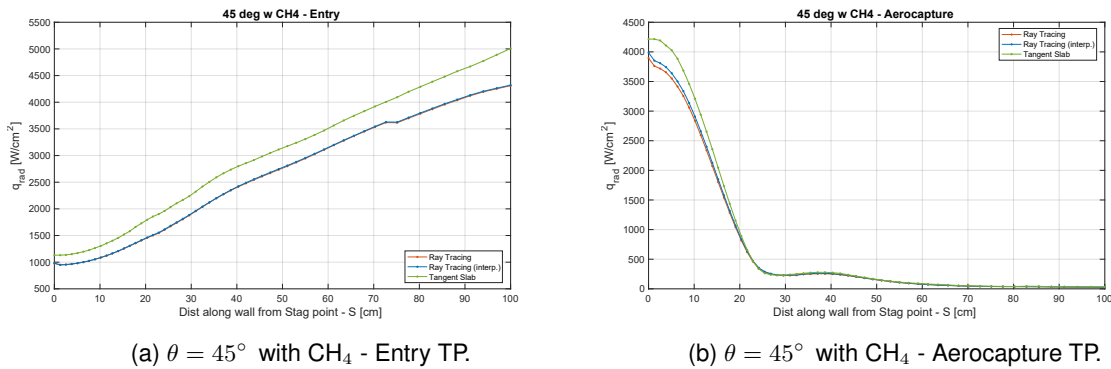
In the Entry TP the difference between post shock temperatures of the stagnation region and the shoulder region is in the order of 1,000K, whereas in the Aerocapture TP this difference is in the order of 10,000K (Figures 4.23a and 4.23b).

The dominant radiative systems for the Entry TP come from C_2 species, and this species concentration evidence significant growth along the path from the stagnation region to the shoulder region. For the

Aerocapture TP, there is no significant change in the dominant species' distribution and the decrease of the radiative heat flux comes mainly from the significant decrease of the temperature.

4.4.3.3 Radiative Model Influence

A check was made to evaluate the use of the linear interpolation in the Ray Tracing method through the cell as discussed in §2.3.2.2. However, this process was only performed for 2 cases ($\theta = 45^\circ$ with CH₄ Entry TP and Aerocapture TP), since there was a significant computational cost for doing it, with run times increasing by almost a factor of 10. This difference also relies on the fact that there were some limitations regarding the RAM memory of the computer being used, and these were more important on this case, since the spectral properties for all cells crossed by a single ray needs to be stored in the memory RAM. This was an handicap when selecting the maximum threads used in the parallel runs of the code, as each parallel run would perform computation on different rays, and thus, each parallel run would require a particular amount of memory to store the intersected cells' (and their neighbors') information.



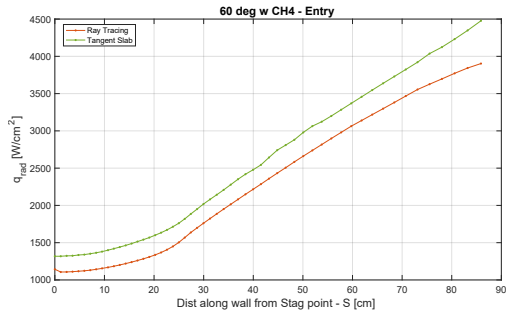
(a) $\theta = 45^\circ$ with CH₄ - Entry TP.

(b) $\theta = 45^\circ$ with CH₄ - Aerocapture TP.

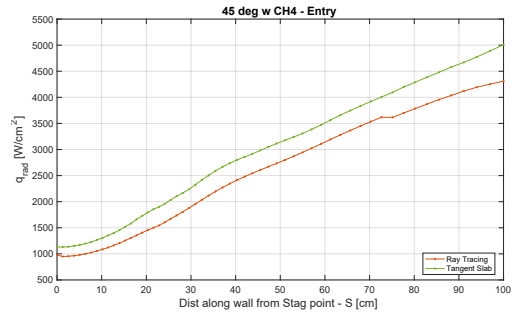
Figure 4.26: Radiative Model Analysis - Linear Interpolation - $\theta = 45^\circ$ with CH₄.

Figure 4.26 show that the error of ignoring this linear interpolation and considering the coefficients as a constant in all cell does not compromise significantly the results with errors below 0.5% for Entry TP and in the order of only 2.5% for Aerocapture TP. For this reason, this linear interpolation method was not used for the remaining cases since the increase in the computational costs did not yield in a significant increment in the accuracy of the results.

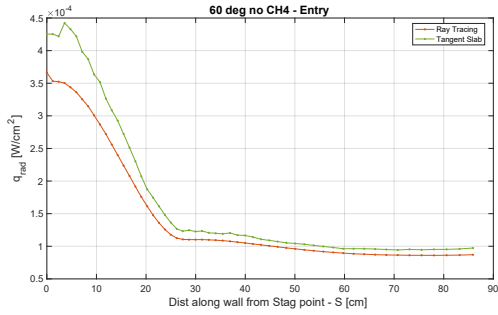
For all the remaining cases, the radiative analysis was performed using both radiative models: Ray Tracing (without linear interpolation) and Tangent Slab, see Figures 4.27 and 4.28 . As mentioned in §2.3.2.1 and §2.3.2.2, the Tangent Slab model overpredicts the radiative wall heat fluxes. This overprediction is almost always between 5-20 % for the majority of the cases. This means that the tangent slab approach could still be applied with modest loss of accuracy and some gains in computational time. However since most of the calculations time is spent computing each cell radiative properties, this gain in computation time becomes diluted. In practice, there is no compelling reason not to resort to the ray-tracing approach.



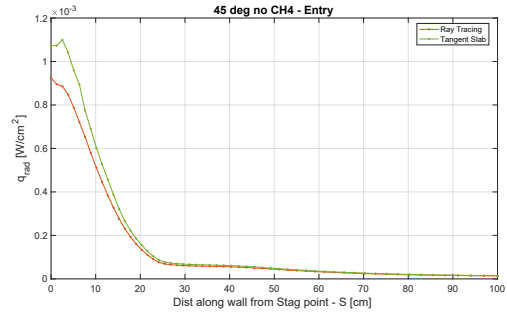
(a) $\theta = 60^\circ$ with CH_4 .



(b) $\theta = 45^\circ$ with CH_4 .

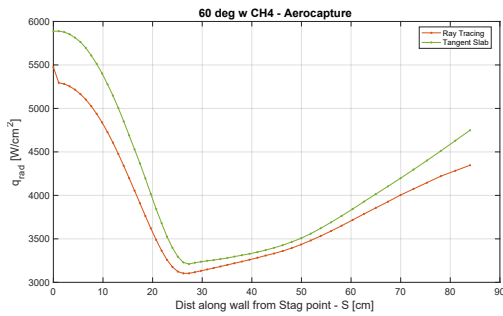


(c) $\theta = 60^\circ$ without CH_4 .

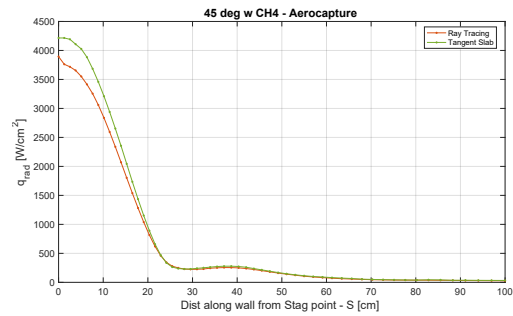


(d) $\theta = 45^\circ$ without CH_4 .

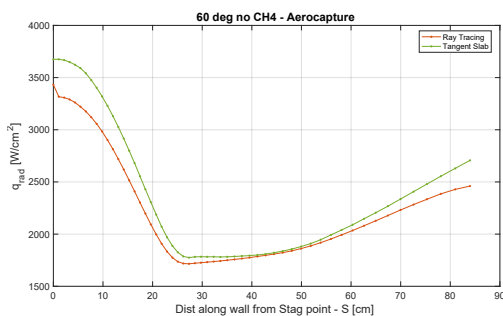
Figure 4.27: Radiative Model influence in Entry TP.



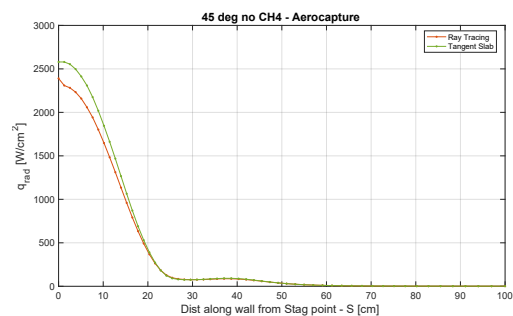
(a) $\theta = 60^\circ$ with CH_4 .



(b) $\theta = 45^\circ$ with CH_4 .



(c) $\theta = 60^\circ$ without CH_4 .



(d) $\theta = 45^\circ$ without CH_4 .

Figure 4.28: Radiative Model influence in Aerocapture TP.

4.4.3.4 Literature Comparison

For both Trajectory points, a few studies were used as comparison. However, a straight forward comparison is not possible since the conditions used in this work were not the same as the ones being compared. These comparisons were made just for cross-checking our results to those independently

obtained by other authors.

Entry Trajectory Point

For the Entry TP, the ESA's CDF Study were considered for comparison. This study was made for several design configurations, but the closest to the ones from this project was a capsule with a nose radius of 0.370m, compared to the nose radius of the capsule with $\theta = 45^\circ$ used in this work ($r_n=0.308$ m). For this reason, the only comparison was done just for this capsule configuration.

It should be mentioned that this study's results for the convective and radiative heat fluxes did not take into account any CFD simulations and were computed only from correlations based on Simmonds and Moss's simulations [58]:

$$q_C = 9.08 \sqrt{\frac{1}{2r_n}} \rho^{0.419778} \left(\frac{V_\infty}{1000} \right)^{2.67892} \quad q_R = 0.091 r_n \rho^{1.3344555} \left(\frac{V_\infty}{1000} \right)^{6.75706138}$$

Table 4.5: Comparison with the literature for Entry TP $\theta = 45^\circ$.

	q_C [W/cm ²]	q_R [W/cm ²]	h [km]	V_∞ [km/s]	p_∞ [Pa]	r_n [m]
ESA's CDF Study [2]	3801	965	112.1	18.77	276	0.370
45 Entry	no CH ₄	~ 0	77.3	18.27	892	0.308
	w CH ₄	6014				

In ESA's CDF study, the results are merely indicative since not only they were achieved using the correlations mentioned before, but also there were significant discrepancies in the freestream properties (particularly in the pressure). Even though the convective heat fluxes differ significantly, the radiative heat fluxes are very similar for the composition A (with CH₄). This is likely purely coincidental.

With this study, discrepancies would be expected between radiative heat fluxes results since these depend on the radiative systems being considered, and ones used in the correlation of Simmonds and Moss are not identical to those in this work.

There is not a significant scattering of the results represented in Table 4.5, proving them not to be unreasonable for the simulations performed.

Aerocapture Trajectory Point

For the Aerocapture TP, the only available literature data comes from the work of Park in [5] and [6], and Hollis *et al.* [10]. These papers presented an analysis of the flow around a body with freestream properties similar to those used in this work for the Aerocapture TP. Also, in these works designs considered a nose radius of 0.5m, similar to the nose radius of the capsule with $\theta = 60^\circ$ used in this work. For this reason, only a comparison was done just for this capsule configuration is conducted since the case of $\theta = 45^\circ$ has a significant difference in the nose radius.

Again, this comparison will be done just to check the scattering (or lack of) the results achieved in the present work. Park's papers present results based on Viscous Shock Layer (VSL) simulations, considering a constant pressure. This method only yields data for the stagnation line. Instead, our work

considers 2D Axisymmetric simulations. Park do not use a true nose radius of 0.5m in the computations, but instead adapted this parameter to achieve a similar shock standoff as the one from Hollis *et al.* (2.8 cm). This is a known limitation of stagnation line CFD models (such as VSL method).

Hollis *et al.* [10] perform 3D simulations for a spacecraft with a significant different shape as the one used in this work, which also makes it inadequate to do straightforward comparisons.

Comparing the stagnation line chemical species evolution with Park's work [6] (Figure 4.29) could be done accurately in qualitative way but not quantitative way since the chemical reactions (and even some chemical species) considered are also different from this work. Nevertheless, even in Park's chemical evolution there is also an increment of H atom mole fraction to close to 8.9×10^{-1} as well as H_2 dissociation making its molar fraction dropping to values around 10^{-5} . The evolution of CH_4 is also similar, with a significant drop below 10^{-10} post-shock, but with an increment of molar fraction into the 10^{-3} mark inside the boundary layer, consequence of the recombination processes and low temperatures. The molar fraction of C_2 is also similar among both works, being around 10^{-8} - 10^{-9} for Park and our work. This give us a good confidence in our kinetic model and on the importance of the minor CH_4 atmospheric concentration in terms of radiative heating processes.

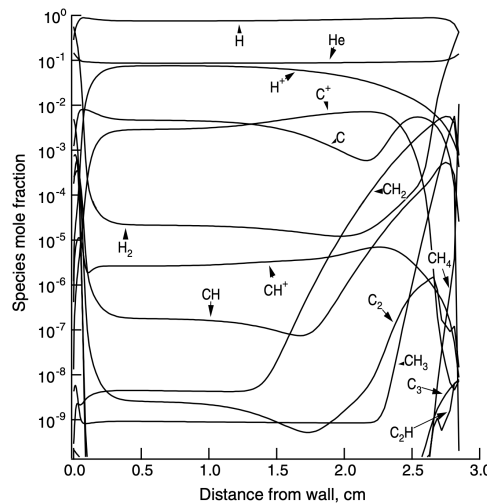


Figure 4.29: Chemical evolution in Stagnation Line from Park [6].

Table 4.6: Comparison with the literature for Aerocapture TP $\theta = 45^\circ$.

	q_C	q_R	V_∞	ρ_∞	T_∞	r_n	x_{shock}
	[W/cm ²]	[W/cm ²]	[km/s]	[g/m ³]	[K]	[m]	[cm]
Hollis <i>et al.</i> [10]	3833	1300	27.7	0.159	103	0.5	2.8
Park (viscous) [6]	N/A	3215	27.7	0.159	103	0.5*	2.8
Park (inviscid) [5]	N/A	2800	27.7	0.159	103	0.5	N/A
60 Aerocap	no CH_4	5036	29	0.378	130	0.5	5.1
	w CH_4	4349	5295	29	0.378	130	0.5

The overall values presented in Table 4.6 differ significantly from the ones from this work. Particularly comparing the shock distance, the values differ to almost 100%. Also, it should not be forgotten that even the freestream properties differ significantly between these different cases. However, as mentioned before, the results present the same order of magnitude, and do not get unreasonable far from the ones in the literature. Further, the differences follow the adequate trends (higher velocities and freestream densities in our case translate in higher convective and radiative heat fluxes).

4.5 Test Case 2

This test case was firstly intended to evaluate the different shapes considered with different cone angles θ_c and sweep angles η , and check which one is more adequate for an aerocapture maneuver. As discussed in §1.3.2.1, an aerocapture maneuver is a lifting entry maneuver and requires an angle of attack. However, our results are obtained with a zero-angle of attack, due to CFD code limitations, and so, these results are merely indicative.

Also, as already mentioned in §4.4.2.2, the results for $\theta = 60^\circ$ lead to subsonic flow speeds in the shoulder region, making our trim tab modeling approach ill-suited in this case. Nevertheless, for the sake of completeness, they will still be presented here.

The influence of the sweep angle η is analyzed, and for each case, the frontal area of the flap is kept constant as 5% of the main body's frontal area.

4.5.1 Aerodynamic coefficients

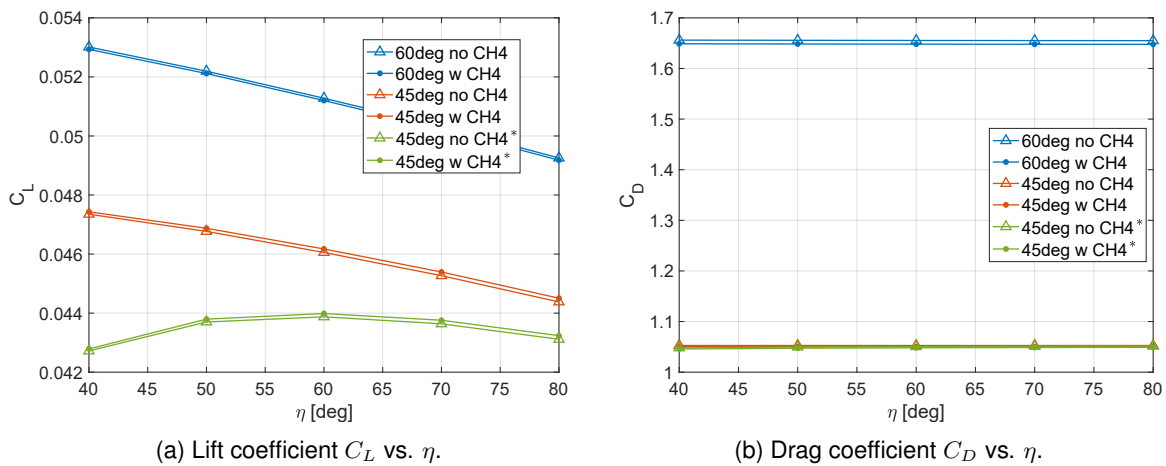


Figure 4.30: Aerodynamic Coefficients for different Sweep Angles η for zero angle of attack.

Analyzing Figure 4.30, C_D is lower for $\theta = 45^\circ$ compared to $\theta = 60^\circ$. Intuitively this makes sense since, for the $\theta = 45^\circ$ capsule, the flow experiences less deflection, or, in other terms, the capsule shape is more aerodynamic.

For $\theta = 45^\circ$ a test was made to test the pressure correction function introduced in §A - see result in Figure 4.30. The Mach considered for these corrections was $M=3.5$, which was the corresponding Mach outside the boundary layer in the flap region. For $\theta = 60^\circ$, the correction was not used since the flow in this region is not supersonic, making this procedure pointless. When the correction is ignored, for lower η values, the C_L is higher.

For more slender flaps (i.e. with small sweep angles) the pressure correction will extend from the trim tab tips to majority of the trim tab (or even the whole trim tab). Since the pressure correction leads to decreased pressure, the overall force on the trim tab will be much smaller than without the corrections. For higher η values, the % of the control surface in these area influenced by the tip is lower, which reflect

in results closer to the ones when the correction is ignored. In other terms, for larger η means that a large portion of the trim tab is not affected by pressure corrections.

The C_D has a low sensibility to the sweep angle η . This is somehow expected since the only difference will be related to the flap since the remaining component from the main body is constant for all cases. The frontal area of the flap is kept constant at a value of 5% of the main body's frontal area. Thus, the projection of the forces in the flap region multiplied by the area will produce always the same force in the x direction, and will result in the same drag, as the pressure in the flap region is almost constant. This projection is independent of the sweep angle and is only dependent on the angle θ_c , Figure 4.31a.

Regarding lift, the scenario is different, as the projection of the forces in the y direction will depend not only on θ_c (Figure 4.31b) but also on ϕ (Figure 4.31c), and consequently η .

For the C_D , the influence of the pressure correction is very low, since just a small portion of the drag comes from the flap, and thus, the influence of this correcting function (only applied to the flap) will be marginal.

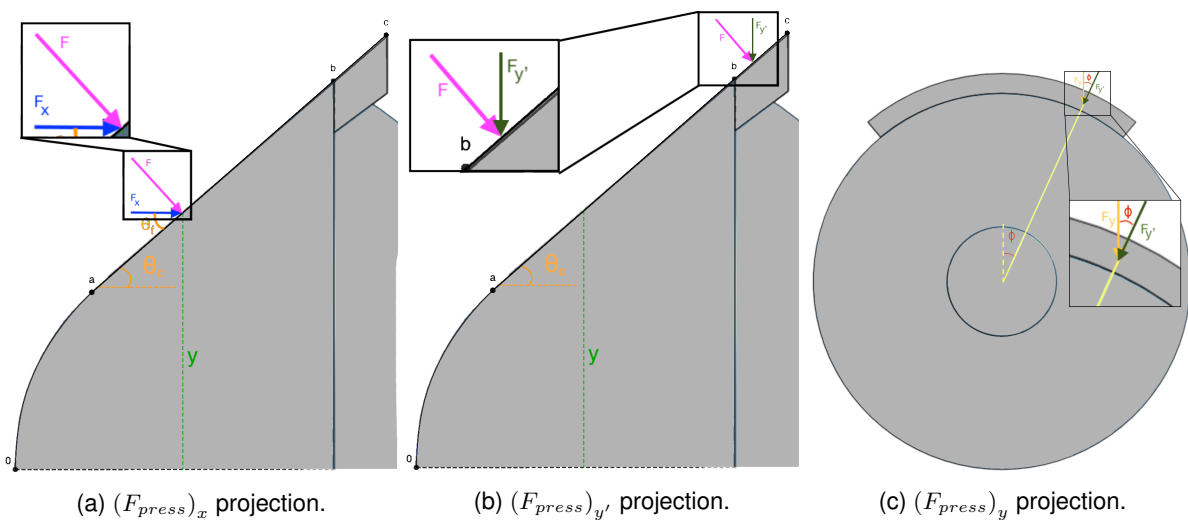


Figure 4.31: Pressure forces projections example.

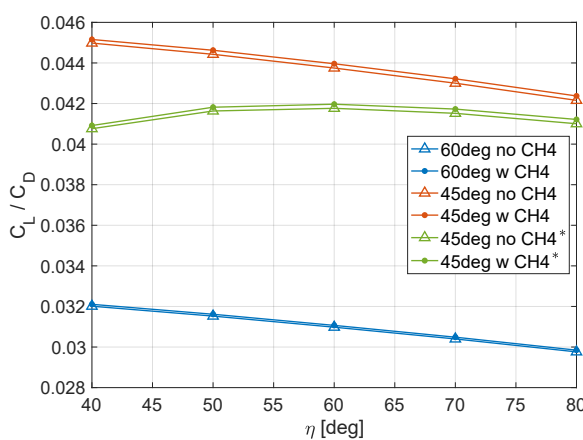


Figure 4.32: Aerodynamic efficiency C_L/C_D vs. η .

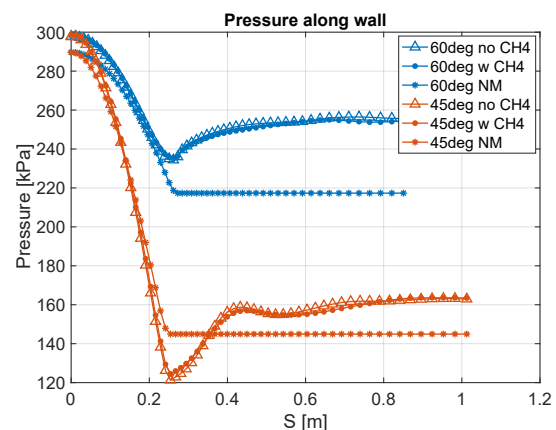


Figure 4.33: Pressure distribution computed in CFD vs Modified Newtonian theory (NM).

Figure 4.32 shows the aerodynamic efficiency for both cases. This efficiency hits a maximum of

0.042 for $\theta = 45^\circ$ for $\eta = 60^\circ$ for the realistic case which considers the pressure correction. This is a low value but is expected since this type of capsule is widely in use for atmospheric entries, and thus, the main goal is have a high drag, to slow down the spacecraft. In this case, the study focused on evaluating the addition of trim tab to this common shape to access the feasibility of designs like this.

In an aerocapture mission, the design of the spacecraft would be significantly different, as it would have to be designed to also generate significant lift. Also, in a real mission design, zero-angle of attack simulations would not be sufficient to evaluate the design, and 3D CFD simulations would also be advised.

Even though viscous forces were considered, the pressure forces are the dominant ones, with the viscous influence being only a fraction around 0.0001% of the total forces.

The higher values of C_D for $\theta = 60^\circ$ are expected as there is a significant increase in the wall pressure in the conical part of the capsule for this capsule design.

Figure 4.33 presents the surface pressure profiles and also compares these with simple Modified Newtonian theory [34] results. This model describes the C_p distribution as a function of $C_{p,stag}$ and the flow impact angle, θ . $C_{p,stag}$ is computed directly from normal shock relations for a perfect gas. This approximation is most accurate for very thin shock layers and is most reliable for C_D estimations and less so for C_L and moment coefficient C_m . The shear forces are neglected in this approach, as usually done for blunt bodies with low to moderate lift-to-drag ratios ($L/D < 1.5$) for hypersonic, continuum flow regimes [54], such as the one considered here. This method considers only the capsule shape and the upstream conditions (for computing $C_{p,stag}$). Even though this is a very simplistic approach, without any considerations about kinetic schemes for example, the results are not completely unreasonable, and present similar results, at least in the same order of magnitude. Therefore, this method may be used for achieving preliminary results with reasonable accuracy.

However, as expected, the bigger discrepancies between CFD results and Newtonian theory are for $\theta = 60^\circ$. This is a consequence of the results not being completely correct (as the shoulder expansion is not implemented), but also since this Newtonian theory loses some of its accuracy when $\theta_c > \theta_s$ (check §4.4.2.2).

Another fact that should be highlighted is the low influence of the chemical composition in the results. This is somehow expected since the chemistry will have more impact in the boundary layer kinetics, and the wall pressure is not as sensible to the kinetic phenomena happening in this layer as the temperature, where chemistry effects have a strong impact. Hence, regarding only the study of aerodynamic properties (with no regard with the aerothermodynamic analysis of the design), future simulations may be performed with the simplest (and quickest to perform) chemical composition - without CH_4 .

Chapter 5

Conclusions

5.1 Achievements

The major achievements of this work are the identification on how the low percentage of CH_4 in Neptune's atmosphere ($\approx 1.5\%$) significantly enhances the radiation of the flow. As a reminder, shock tube experiments for similar chemical compositions (Jovian atmosphere with 89% H_2 /11 % He) show that radiance for these flows only becomes apparent above 25 km/s. Our numerical results confirm this finding (in the absence of CH_4) since radiative heating is negligible for Entry TP at 18 km/s, but noticeable for the Aerocapture TP at 29 km/s. Once the small fraction of CH_4 is accounted for, the results change dramatically. CH_4 dissociates in the shock layer leading to the formation of hot C and C_2 which strongly radiate in the whole domain. Radiative heating becomes comparable to convective heating even for the Entry TP at 18 km/s, and the Aerocapture TP is impacted as well.

Following these interesting results, sensibility studies regarding the kinetics (considering more complex chemical kinetics databases), the chemical composition (slight changes to the free-stream species molar fractions) and Neptune's atmospheric models (other than Neptune GRAM used here) as well as further experimental studies (shock tube testing now accounting for the small percentage of CH_4) should be carried out to better understand these phenomena and define appropriate design margins for a future mission to Neptune.

This work also provides some insight on the stability for two popular capsule geometric configurations, $\theta_c = 60^\circ$ and $\theta_c = 45^\circ$ sphere-cone.

In terms of total wall heat fluxes for the Entry TP, both designs are more or less equivalent as the 60° geometry minimizes convective heating but maximizes radiative heating, and the opposite for 45° configuration. Since both heat fluxes have the same order of magnitude, no clear advantage for a specific geometry may be found in this case. For the Aerocapture TP, the situation is different, as the flow remains subsonic in the shock layer, with an increased shock standoff. This is detrimental in terms of radiative heating, a non local phenomena: a larger volume of the shock layer translates in larger heat fluxes for the 60° geometry. Here the results show that the 45° configuration is clearly superior in these terms.

In terms of stability, the 45° configuration should be in general more favorable since it is easier to bring the aerodynamic center behind the center of gravity. In addition to this, and owing to the chemical composition of Neptune, the high post-shock γ for the flow adds to the possible instabilities for the 60° configuration. It was found that cone angles larger than 46° , a transition of the sonic line from the nose cap (in the spherical part of the capsule) towards the shoulder was evidenced numerically. The successful use of control surfaces, such as the trim tab mentioned in this work, become even more difficult to achieve for larger angles. 3D simulations should be performed to better analyze these events.

Regarding the use of the trim tab, the aerodynamic analysis concluded that low lift coefficients C_L are achieved, compared to the drag coefficient C_D . However, even with this value being relatively low, it may be enough for generating enough moments since this lifting force will have a corresponding significant moment arms (since the trim tab is located in the border of the capsule) and will achieve what is desired: rotate the capsule for achieving an angle of attack without the need for ballast or RCS and their associated mass.

5.2 Future Work

A few straight forward ideas for future developments include:

- Test different trajectory points, trying to simulate a full mission trajectory, and using intermediate results of the aerodynamic coefficients as inputs to find the next trajectory point for CFD solution;
- Introducing more chemical species, for example the ones mentioned in [6] (C_2H and C_3), to confirm their low influence on the flow field (assuming no ablation);
- Perform the analysis using meshes with more cells, and introduce the continuity on the second order derivative of the capsule's shape;
- Study the cant angle influence, keeping the same sweep angle, or even study different locations of the trim tab(s).

Some more challenging developments would include:

- Radiation coupling in the flow, which will be possible in the future as the computational tools' performance increase;
- Introducing ablation phenomena at the wall;
- Test the influence of turbulence by adding a simplified turbulence model;
- Perform the simulation considering all the domain around the body, and not only the frontal part;
- Perform studies to account for angle of attack, and evaluate the phenomena of the sonic line transition;
- Perform simulations with different capsule's shapes, particularly for aerocapture maneuver, where the sphere-cone is not an usual choice.

Bibliography

- [1] NASA. Neptune Lithograph - Our Solar System, 2013. URL https://www.nasa.gov/sites/default/files/files/Neptune_Lithograph.pdf. Last accessed 20 December 2020
- [2] S. Bayon and M. Bandecchi. CDF Study Report Ice Giants A Mission to the Ice Giants – Neptune and Uranus. Technical report, ESA, 2019.
- [3] J. Bertin. *Hypersonic Aerothermodynamics*. 1994. doi: 10.2514/4.470363.
- [4] J. D. Anderson Jr. *Hypersonic and High-Temperature Gas Dynamics, Second Edition*. 2006. doi: 10.2514/4.861956.
- [5] C. Park. Nonequilibrium Chemistry and Radiation for Neptune Entry. *Journal of Spacecraft and Rockets*, 48(6):897–903, 2011. doi: 10.2514/1.51810.
- [6] C. Park. Viscous Shock-layer Calculation of Stagnation-region Heating Environment in Neptune Aerocapture. *Journal of Spacecraft and Rockets*, 51(2):635–639, 2014. doi: 10.2514/1.A32591.
- [7] L. Santos Fernandes. *Computational Fluid Radiative Dynamics of The Galileo Jupiter Entry at 47.5 km/s*. Master’s thesis, Instituto Superior Técnico, 2019.
- [8] D. F. Potter. *Modelling of Radiating Shock Layers for Atmospheric Entry at Earth and Mars*. Phd thesis, University of Queensland, Australia, 2011.
- [9] R. Jits, M. Wright, and Y. K. Chen. Closed-loop Trajectory Simulation for Thermal Protection System Design for Neptune Aerocapture. *Journal of Spacecraft and Rockets*, 42(6):1025–1034, 2005. doi: 10.2514/1.13428.
- [10] B. R. Hollis, M. J. Wright, J. Olejniczak, N. Takashima, K. Sutton, and D. Prabhu. Preliminary Convective-Radiative Heating Environments for a Neptune Aerocapture Mission. *Collection of Technical Papers - AIAA Atmospheric Flight Mechanics Conference*, 2(August):1040–1051, 2004. doi: 10.2514/6.2004-5177.
- [11] NASA. 10 Things to know about the Kuiper Belt, 2018. URL <https://solarsystem.nasa.gov/news/792/10-things-to-know-about-the-kuiper-belt/>. Last accessed 20 December 2020
- [12] M. Lockwood. Neptune Aerocapture Systems Analysis. Technical report, NASA Langley Research Center, 2006.

- [13] M. M. Munk and S. Moon. Aerocapture Technology Development Overview. *IEEE Aerospace Conference Proceedings*, 2008. doi: 10.1109/AERO.2008.4526545.
- [14] M. S. Martin, G. F. Mendeck, P. B. Brugarolas, G. Singh, F. Serricchio, S. W. Lee, E. C. Wong, and J. C. Essmiller. In-flight experience of the Mars Science Laboratory Guidance, Navigation, and Control system for Entry, Descent, and Landing. *CEAS Space Journal*, 7(2):119–142, 2015. doi: 10.1007/s12567-015-0091-3.
- [15] S. V. Perino, J. Bayandor, S. C. Armand, and J. A. Samareh. Structural Concept Study for Planetary Probes and Sample Return vehicles. *Journal of Spacecraft and Rockets*, 52(5):1320–1330, 2015. doi: 10.2514/1.A33050.
- [16] M. Tauber, P. Wercinski, W. Heniine, L. Yang, and J. Paterson. Uranus and Neptune Atmospheric Entry Probe Study. *Flight Simulation and Technologies*, 1993, 31(5):799–805, 1994. doi: 10.2514/3.26515.
- [17] J. E. Johnson, M. J. Lewis, and R. P. Starkey. Multiobjective Optimization of Earth-entry Vehicle Heat Shields. *Journal of Spacecraft and Rockets*, 49(1):38–50, 2012. doi: 10.2514/1.42565.
- [18] A. Korzun, K. Murphy, and K. Edquist. Supersonic Aerodynamic Characteristics of Blunt Body Trim Tab Configurations. Technical report, AIAA, jun 2013.
- [19] C. Park and W. Griffith. Nonequilibrium Hypersonic Aerothermodynamics. *Physics Today*, 1991. doi: 10.1063/1.2809999.
- [20] C. R. Wilke. A Viscosity Equation for Gas Mixtures. *The Journal of Chemical Physics*, 1950. doi: 10.1063/1.1747673.
- [21] F. G. Blottner, M. Johnson, and M. Ellis. Chemically Reacting Viscous Flow Program for Multi-component Gas Mixture. *Tech. Rep. SC-RR-70-754, Sandia Labs, Albuquerque, N. Mex. USA*, 1971. doi: 10.2172/4658539.
- [22] G. Palmer and M. J. Wright. A Comparison of Methods to Compute High Temperature Gas Thermal Conductivity. In *36th AIAA Thermophysics Conference*, 2003. doi: 10.2514/6.2003-3913.
- [23] D. D. Loureiro. *High-temperature Modeling of Transport Properties in Hypersonic Flows*. Master's thesis, Instituto Superior Técnico, 2015.
- [24] G. E. Palmer and M. J. Wright. Comparison of methods to compute high-temperature gas viscosity. *Journal of Thermophysics and Heat Transfer*, 2003. ISSN 15336808. doi: 10.2514/2.6756.
- [25] R. N. Gupta and M. J. Yos. A review of reaction rates and thermodynamic and transport properties for an 11-species Air model for chemical and thermal nonequilibrium calculations to 30,000 K, 1990. URL <https://ntrs.nasa.gov/citations/19900017748>. Last accessed 29 December 2020
- [26] M. J. Yos. Approximate Equations for the Viscosity and Translational Thermal Conductivity of gas mixtures. *Tech. Rep. AVSSD-0112-67-RM, Avco Corporation, Wilmington, Massachusetts*, 1967.

- [27] J. D. Ramshaw and C. H. Chang. Ambipolar Diffusion in Two-temperature Multicomponent Plasmas. *Plasma Chemistry and Plasma Processing*, 1993. doi: 10.1007/BF01465878.
- [28] F. F. Chen. *Introduction to Plasma Physics and Controlled Fusion*. 1984. doi: 10.1007/978-1-4757-5595-4.
- [29] J. H. Lee. Basic Governing Equations for the Flight Regimes of aeroassisted orbital transfer vehicles. In *AIAA Paper*, 1984. doi: 10.2514/6.1984-1729.
- [30] W. G. Vincenti, C. H. Kruger, and T. Teichmann. Introduction to Physical Gas Dynamics. *Physics Today*, 1966. doi: 10.1063/1.3047788.
- [31] Y. B. Zel'dovich, Y. P. Raizer, W. D. Hayes, R. F. Probstein, and S. P. Gill. Physics of Shock Waves and High-Temperature Hydrodynamic Phenomena. *Journal of Applied Mechanics*, 1, 1967. doi: 10.1115/1.3607836.
- [32] M. F. Modest. Radiative Heat Transfer. *Radiative Heat Transfer*, 2013. doi: 10.1016/C2010-0-65874-3.
- [33] H. R. Griem. *Principles of Plasma Spectroscopy*. 1997. doi: 10.1017/cbo9780511524578.
- [34] B. Andersen and S. Whitmore. Aerodynamic Control on a Lunar Return Capsule using Trim-Flaps. In *45th AIAA Aerospace Sciences Meeting and Exhibit*. American Institute of Aeronautics and Astronautics, 2007. doi: 10.2514/6.2007-855.
- [35] B. Lopez and M. Lino da Silva. SPARK: A Software Package for Aerodynamics, Radiation and Kinetics. *46th AIAA Thermophysics Conference*, pages 13–17, 2016. doi: 10.2514/6.2016-4025.
- [36] D. A. Andrienko. *Non-Equilibrium Models for High Temperature Gas Flows*. Phd thesis, Wright State University, 2014.
- [37] M. Lino da Silva, S. Espinho, and B. Lopez. SPARTAN 2.6 User's Manual, 2016.
- [38] Á. González. Measurement of Areas on a Sphere Using Fibonacci and Latitude-Longitude Lattices. *Mathematical Geosciences*, 2010. doi: 10.1007/s11004-009-9257-x.
- [39] J. I. Lunine. Atmospheres of Uranus and Neptune. *Annual Rev. Astron. Astrophys.*, 31:217–263, 1993. doi: 10.1146/annurev.aa.31.090193.001245.
- [40] G. Palmer, D. Prabhu, and B. A. Cruden. Uncertainty determination for aeroheating in Uranus and Saturn probe entries by the Monte Carlo method. In *44th AIAA Thermophysics Conference*, 2013. doi: 10.2514/6.2013-2776.
- [41] L. P. Leibowitz and T.-j. Kuo. Ionizational Nonequilibrium Heating During Outer Planetary Entries. *AIAA Journal*, 14(9):1324–1329. doi: 10.2514/3.61465.
- [42] B. A. Cruden and D. W. Bogdanoff. Shock radiation tests for saturn and uranus entry probes. *Journal of Spacecraft and Rockets*, 2017. doi: 10.2514/1.A33891.

- [43] M. L. Silva, D. Tsyhanou, V. Guerra, and J. Loureiro. A Physically-Consistent Chemical Dataset for the Simulation of N₂ – CH₄ Shocked Flows Up to T = 100000 K. Technical report, 2011.
- [44] T. Gökçen. N₂ - CH₄ - Ar chemical kinetic model for simulations of titan atmospheric entry. *Journal of Thermophysics and Heat Transfer*, 2007. doi: 10.2514/1.22095.
- [45] H. F. Nelson, C. Park, and E. E. Whiting. Titan atmospheric composition by hypervelocity shock-layer analysis. *Journal of Thermophysics and Heat Transfer*, 1991. doi: 10.2514/3.243.
- [46] D. Bruno, C. Catalfamo, M. Capitelli, G. Colonna, O. De Pascale, P. Diomedea, C. Gorse, A. Laricchiuta, S. Longo, D. Giordano, and F. Pirani. Transport properties of high-temperature Jupiter atmosphere components. *Physics of Plasmas*, 2010. doi: 10.1063/1.3495980.
- [47] D. K. Prabhu and D. A. Saunders. On heatshield shapes for Mars entry capsules. In *50th AIAA Aerospace Sciences Meeting Including the New Horizons Forum and Aerospace Exposition*, 2012. doi: 10.2514/6.2012-399.
- [48] T. W. Rees, P. J. Bruce, and J. A. Merrifield. The effect of reynolds number on the hypersonic flow around faceted shapes. *22nd AIAA International Space Planes and Hypersonics Systems and Technologies Conference*, (September), 2018. doi: 10.2514/6.2018-5197.
- [49] P. Subrahmanyam. Development of an Interactive Hypersonic Flow Solver Framework for Aerothermodynamic Analysis. *Engineering Applications of Computational Fluid Mechanics*, 2(4):436–455, 2008. doi: 10.1080/19942060.2008.11015243.
- [50] R. A. Thompson and P. A. Gnoffo. Application of the LAURA code for slender-vehicle aerothermodynamics. *Journal of Spacecraft and Rockets*, 29(1):16–23, 1992. doi: 10.2514/3.26309.
- [51] R. W. MacCormack. Carbuncle computational fluid dynamics problem for blunt-body flows. *Journal of Aerospace Information Systems*, 10(5):229–239, 2013. doi: 10.2514/1.53684.
- [52] M. Pandolfi and D. D’Ambrosio. Numerical Instabilities in Upwind Methods: Analysis and Cures for the “Carbuncle” Phenomenon. *Journal of Computational Physics*, 166(2):271–301, 2001. doi: 10.1006/jcph.2000.6652.
- [53] L. Santos Fernandes, B. Lopez, and M. Lino da Silva. Computational fluid radiative dynamics of the Galileo Jupiter entry. *Physics of Fluids*, 31(10):106104, oct 2019. doi: 10.1063/1.5115264.
- [54] P. A. Gnoffo. Planetary-entry gas dynamics, 1999.
- [55] J. C. South. Calculation of axisymmetric supersonic flow past blunt bodies with sonic corners, including a program description and listing. *NASA Technical Note*, 1968.
- [56] H. G. Hornung, J. Martinez Schramm, and K. Hannemann. Hypersonic flow over spherically blunted cone capsules for atmospheric entry. Part 1. The sharp cone and the sphere. *Journal of Fluid Mechanics*, 2019. doi: 10.1017/jfm.2019.342.

- [57] P. A. Gnoffo, K. James Weilmuenster, R. D. Braun, and C. I. Cruz. Effects of sonic line transition on aerothermodynamics of the mars pathfinder probe. In *13th Applied Aerodynamics Conference*, 1995. doi: 10.2514/6.1995-1825.
- [58] J. Moss and A. Simmonds. Galileo probe forebody flowfield predictions during Jupiter entry. page 874. 3rd Joint Thermophysics, Fluids, Plasma and Heat Transfer Conference, 1982. doi: 10.2514/6.1982-874.
- [59] J. C. F. Pereira. *Aerodinâmica Compressível - Sebenta de Aerodinâmica II*. AEIST - Instituto Superior Técnico, 2018.
- [60] M. Matos. *Aerothermodynamic Properties of an Upper Stage Rocket Equipped with Control Surfaces*. Master's thesis, Instituto Superior Técnico, 2019.

Appendix A

Forces on the capsule

The aerodynamic forces exerted on an entry capsule are of twofold: pressure forces, normal to the surface, and viscous forces, tangential to the surface.

$$dF^P = -(p - p_\infty)\hat{\mathbf{n}} \cdot dS \quad (\text{A.1})$$

$$dF^V = \boldsymbol{\tau} \cdot dS \quad (\text{A.2})$$

$$\boldsymbol{\tau} = \tau \hat{\mathbf{t}} = \mu_w \left(\frac{\partial U}{\partial y} \right)_w \hat{\mathbf{t}} \quad (\text{A.3})$$

Generally, for a sphere-cone capsule configuration as the one discussed on this work, we may divide the integration in two parts (actually, since we are also considering the effect of the trim-tab/flap, we may divide it into three; however, the flap part is very similar to the conical part, except for the pressure correction related to the 3D influence of the flap tips).

We consider here the point a as the point that connects the spherical part and the conical part, the point b the point that connects the end of the forebody with the flap, and the point c the edge of the flap. η is the sweep angle covered by the trim tab/flap.

$$F^P = F^P_{sph} + F^P_{con} + F^P_{flap} \quad (\text{A.4})$$

$$F^V = F^V_{sph} + F^V_{con} + F^V_{flap} \quad (\text{A.5})$$

A.1 Pressure Forces

Starting with the spherical part, and taking into account that in the y and z directions the forces would cancel each other since the pressure would have symmetrical components in this direction along the sweep angle ϕ :

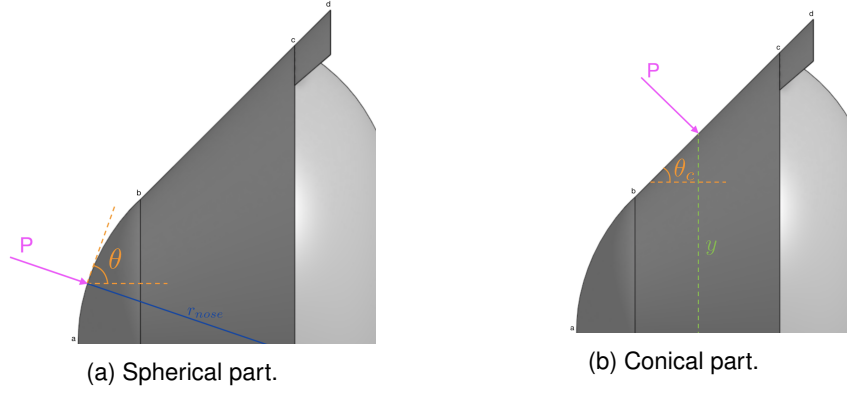


Figure A.1: Pressure Forces.

$$\begin{aligned}
 F^P_{sph} &= \int_0^{2\pi} \int_{\frac{\pi}{2}}^{\theta} (p - p_{\infty}) \cdot R d\theta d\phi \\
 (F_x)^P_{sph} &= 2\pi R \int_{\frac{\pi}{2}}^{\theta} (p - p_{\infty}) \sin \theta d\theta = 2\pi R \sum_{i=0}^a (p_i - p_{\infty}) \sin \theta_i \Delta\theta_i
 \end{aligned} \tag{A.6}$$

For the conical part (the same applies to the forces in the y and z directions as before):

$$\begin{aligned}
 F^P_{con} &= \int \int (p - p_{\infty}) \cdot dl \cdot y \cdot d\phi = \int_0^{2\pi} \int_{x_a}^{x_b} (p - p_{\infty}) \cdot \frac{dx}{\cos \theta_f} \cdot y \cdot d\phi \\
 (F_x)^P_{con} &= 2\pi \frac{\sin \theta_f}{\cos \theta_f} \int_{x_a}^{x_b} (p - p_{\infty}) \cdot y \cdot dx = 2\pi \tan \theta_f \sum_{i=a}^b (p_i - p_{\infty}) \cdot y_i \Delta x_i \\
 (F_x)^P_{con} &= 2\pi \sum_{i=a}^b (p_i - p_{\infty}) \cdot y_i \Delta y_i
 \end{aligned} \tag{A.7}$$

Finally, for the flap part, we need to consider a correction function $K(\bar{t})$ (see Figure A.4), as discussed in [59]. This pressure correction takes into account the 3D effects of the flow near the trim tab tips, which generate a disturbed area. Outside that area, there is no influence of the 3D flow, and the flow properties do not need any correction. That area is calculated in an approximate fashion, considering the geometry near the tip as almost rectangular, which makes it possible for this correction being performed this way. The disturbed area is calculated knowing the Mach angle μ (Figure A.2) which allows us to calculate at each mesh point the distance d from the tip to the undisturbed area (Figure A.5). \bar{t} is the circumferential distance to the flap tip. D is the total width of the trim tab with constant distance l to the beginning on the flap.

Now the forces in the y direction will not be canceled out since the flap only sweeps a certain angle. However, in the z direction the same applies as before, since we can consider the flap being located symmetrically to the plan xy .

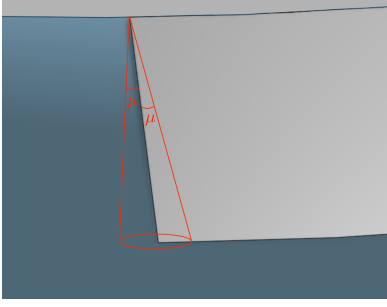


Figure A.2: Disturbed zone on trim tab lateral edge with Mach angle μ .

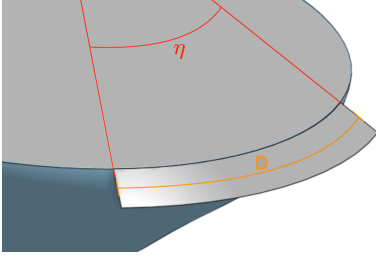


Figure A.3: Trim tab width - distance D

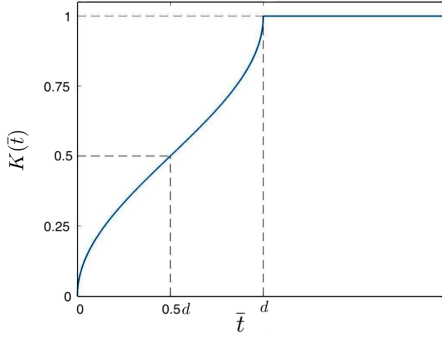


Figure A.4: Pressure correction function. Adapted from [60].

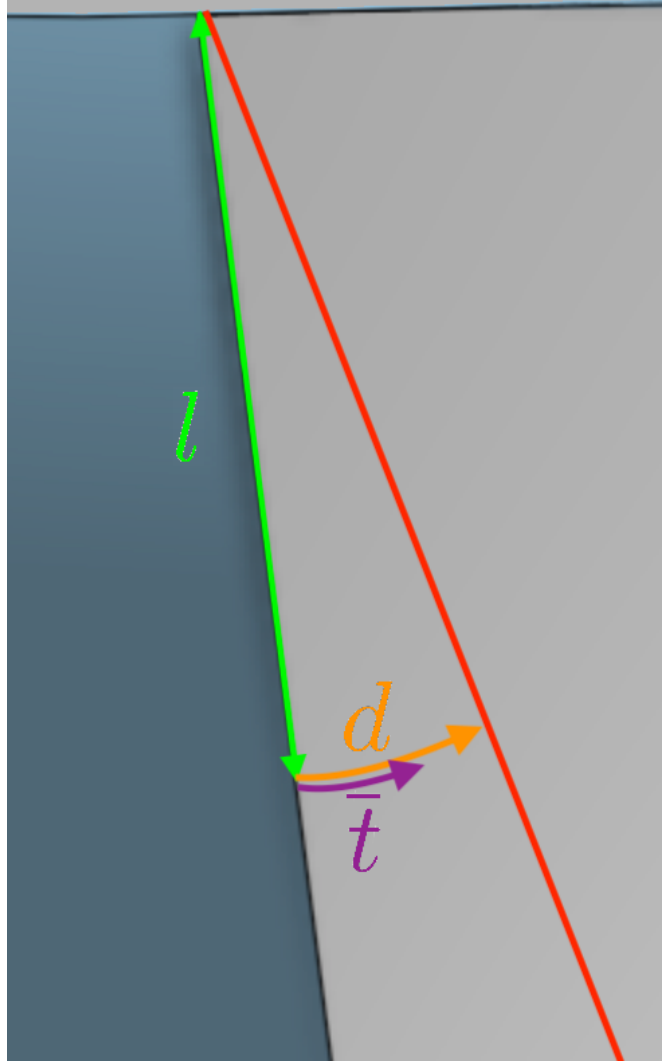


Figure A.5: Distances l , \bar{t} and d .

Now, the forces in the y direction will not be canceled out since the flap only sweeps over a certain angle. However, the same applies as before in the z direction, since we can consider the flap being located symmetrically to the plan xy .

$$K = \begin{cases} \frac{2}{\pi} \arcsin \sqrt{\frac{\bar{t}}{d}} & \bar{t} < d \\ 1 & \bar{t} \geq d \end{cases} \quad (\text{A.8})$$

$$F^P_{flap} = 2 \int_0^{\frac{\eta}{2}} \int_{x_b}^{x_c} (p - p_\infty) \cdot K \cdot dl \cdot y \cdot d\phi \quad , \quad yd\phi = d\bar{t} \quad (\text{A.9})$$

$$\begin{aligned} &= 2 \int_0^{\frac{D}{2}} \int_{x_b}^{x_c} (p - p_\infty) \cdot K(\bar{t}) \frac{dx}{\cos \theta_f} d\bar{t} \quad (\text{A.10}) \\ \int_0^{\frac{D}{2}} K(\bar{t}) d\bar{t} &= \int_0^d \frac{2}{\pi} \arcsin \left(\sqrt{\bar{t}/d} \right) d\bar{t} + \int_d^{\frac{D}{2}} 1 \cdot d\bar{t} \\ &= \frac{D-d}{2} \end{aligned}$$

$$\text{with} \quad D = \eta \cdot y \quad d = l \cdot \tan(\mu) \quad \mu = \arcsin \left(\frac{1}{M} \right)$$

And back to (A.10) yields:

$$\begin{aligned}
 F^P_{flap} &= 2 \int_{x_b}^{x_c} (p - p_\infty) \cdot \frac{D - d}{2} \frac{dx}{\cos \theta_f} \\
 &= \frac{1}{\cos \theta_f} \int_{x_b}^{x_c} (p - p_\infty) \cdot [\eta \cdot y - l \cdot \tan(\mu)] dx \\
 &= \frac{1}{\cos \theta_f} \sum_{i=b}^c (p_i - p_\infty) \cdot [\eta \cdot y_i - l_i \cdot \tan(\mu)] \Delta x_i
 \end{aligned} \tag{A.11}$$

$$(F_x)^P_{flap} = F^P_{flap} \cdot \sin \theta_f = \tan \theta_f \sum_{i=b}^c (p_i - p_\infty) \cdot [\eta \cdot y_i - l_i \cdot \tan(\mu)] \Delta x_i \tag{A.12}$$

$$(F_{y'})^P_{flap} = F^P_{flap} \cdot \cos \theta_f = \sum_{i=b}^c (p_i - p_\infty) \cdot [\eta \cdot y_i - l_i \cdot \tan(\mu)] \Delta x_i \tag{A.13}$$

A final note should be made, informing that the pressure correction was only performed for $\theta = 45^\circ$ since at the trajectory point where this was implemented, the results for $\theta = 60^\circ$ were poorly physical and the flow near the flap is subsonic, and using this approximation does not make sense.

A.2 Viscous Forces

The same may be done for the viscous forces but this time the flap does not need any correction.

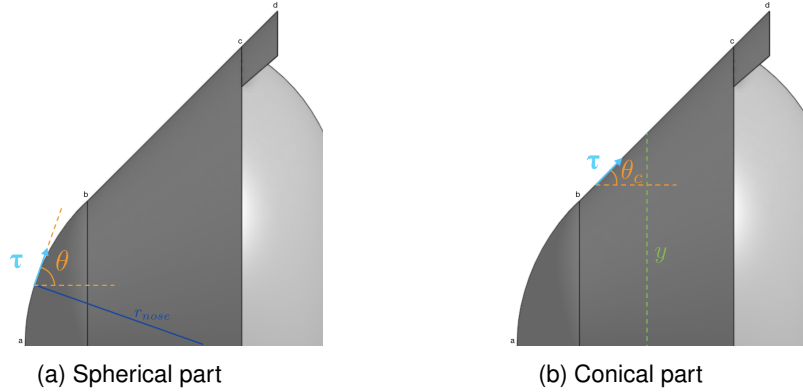


Figure A.6: Viscous Forces.

$$\begin{aligned}
 F^V_{sph} &= \int_0^{2\pi} \int_{\frac{\pi}{2}}^{\theta} \tau \cdot R d\theta d\phi = \\
 (F_x)^V_{sph} &= 2\pi R \int_{\frac{\pi}{2}}^{\theta} \tau \cos \theta d\theta = \sum_{i=0}^a (\tau)_i \cos \theta_i \cdot \Delta \theta_i
 \end{aligned}$$

$$F^V_{con} = \int \int \tau \cdot dl \cdot y \cdot d\phi = \int_0^{2\pi} \int_{x_a}^{x_b} \tau \cdot \frac{dx}{\cos \theta_f} \cdot y \cdot d\phi$$

$$(F_x)^V_{con} = 2\pi \frac{\cos \theta_f}{\cos \theta_f} \int_{x_a}^{x_b} \tau \cdot y \cdot dx = 2\pi \sum_{i=a}^b (\tau)_i \cdot y_i \cdot \Delta x_i$$

$$(F_x)^V_{flap} = \eta \frac{\cos \theta_f}{\cos \theta_f} \int_{x_b}^{x_c} \tau \cdot y \cdot dx = \eta \sum_{i=b}^c (\tau)_i \cdot y_i \cdot \Delta x_i$$

$$(F_{y'})^V_{flap} = \eta \frac{\sin \theta_f}{\cos \theta_f} \int_{x_b}^{x_c} \tau \cdot y \cdot dx = \eta \tan \theta_f \sum_{i=b}^c (\tau)_i \cdot y_i \cdot \Delta x_i$$

Appendix B

Chemical Dataset

Table B.1: Chemical Dataset; $K_f = A \cdot T^n \cdot \exp(-\theta_R/T)$ [$\text{cm}^3\text{mol}^{-1}\text{s}^{-1}$]

	Comp.		Reaction	A	n	θ_R [K]	Ref.
	A	B					
R1	•	•	H + H \rightleftharpoons H ⁺ + e ⁻ + H	6.17×10^{10}	+0.50	116000	[41]
R2	•	•	H + He \rightleftharpoons H ⁺ + e ⁻ + He	4.88×10^{08}	+0.50	116000	[41]
R3	•	•	H ₂ + M \rightleftharpoons H + H + M	2.23×10^{14}	+0.00	48350	[43]
R4	•		CH ₄ + M \rightleftharpoons CH ₃ + H + M	1.06×10^{22}	-1.46	49900	[43]
R5	•		CH ₃ + M \rightleftharpoons CH ₂ + H + M	2.82×10^{14}	+0.00	42460	[43]
R6	•		CH ₃ + M \rightleftharpoons CH + H ₂ + M	5.00×10^{15}	+0.00	42800	[43]
R7	•		CH ₂ + M \rightleftharpoons CH + H + M	4.00×10^{15}	+0.00	41800	[43]
R8	•		CH ₂ + M \rightleftharpoons C + H ₂ + M	1.30×10^{14}	+0.00	29700	[43]
R9	•		CH + M \rightleftharpoons C + H + M	1.90×10^{14}	+0.00	33700	[43]
R10	•		C ₂ + M \rightleftharpoons C + C + M	3.72×10^{14}	+0.00	69800	[43]
R11	•		CH ₃ + H \rightleftharpoons CH ₂ + H ₂	6.03×10^{13}	+0.00	7600	[43]
R12	•		CH ₂ + H \rightleftharpoons CH + H ₂	4.21×10^{09}	-0.09	-1560	[43]
R13	•		CH + C \rightleftharpoons C ₂ + H	2.00×10^{14}	+0.00	0	[43]
R14	•		C + H ₂ \rightleftharpoons CH + H	4.00×10^{14}	+0.00	11700	[43]
R15	•		H + CH ₄ \rightleftharpoons CH ₃ + H ₂	1.54×10^{20}	+0.00	6874	[43]
R16	•	•	H + H \rightleftharpoons H ₂ ⁺⁺ + e ⁻	1.13×10^{15}	-0.06	129060	[43]
R17	•		C + H \rightleftharpoons CH ⁺ + e ⁻	9.95×10^{11}	+0.52	84830	[43]
R18	•		C + C \rightleftharpoons C ₂ ⁺ + e ⁻	3.19×10^{14}	-0.24	70690	[43]
R19	•	•	H + e ⁻ \rightleftharpoons H ⁺ + e ⁻ + e ⁻	2.28×10^{13}	+0.50	157800	[41]
R20	•	•	He + e ⁻ \rightleftharpoons He ⁺ + e ⁻ + e ⁻	1.33×10^{13}	+0.50	285200	[41]
R21	•		C + e ⁻ \rightleftharpoons C ⁺ + e ⁻ + e ⁻	1.24×10^{15}	+0.28	142700	[43]
R22	•	•	H ₂ + e ⁻ \rightleftharpoons H ₂ ⁺ + e ⁻ + e ⁻	4.05×10^{13}	+0.52	180767	[43]
R23	•		CH + e ⁻ \rightleftharpoons CH ⁺ + e ⁻ + e ⁻	1.15×10^{12}	+0.87	123430	[43]
R24	•		CH ⁺ + e ⁻ \rightleftharpoons C ⁺ + H + e ⁻	4.05×10^{13}	+0.52	180767	[43]
R25	•		CH ⁺ + e ⁻ \rightleftharpoons C + H ⁺ + e ⁻	8.53×10^{09}	+1.23	51400	[43]
R26	•		C ₂ + e ⁻ \rightleftharpoons C ₂ ⁺ + e ⁻ + e ⁻	1.83×10^{13}	+0.68	151119	[43]
R27	•	•	H ₂ ⁺ + e ⁻ \rightleftharpoons H ⁺ + H ⁺ + e ⁻ + e ⁻	2.28×10^{15}	+0.03	335960	[43]
R28	•		CH ⁺ + e ⁻ \rightleftharpoons C ⁺ + H ⁺ + e ⁻ + e ⁻	3.92×10^{09}	+1.30	247590	[43]
R29	•	•	H ₂ ⁺ + e ⁻ \rightleftharpoons H + H	7.08×10^{14}	-0.40	0	[41]

M = (CH₄, CH₃, CH₂, CH, C₂, H₂, C, H, He, C⁺, H⁺, He⁺, e⁻) *

* - carbonaceous species only apply to chemical composition A

Appendix C

Database from NASA's Neptune GRAM

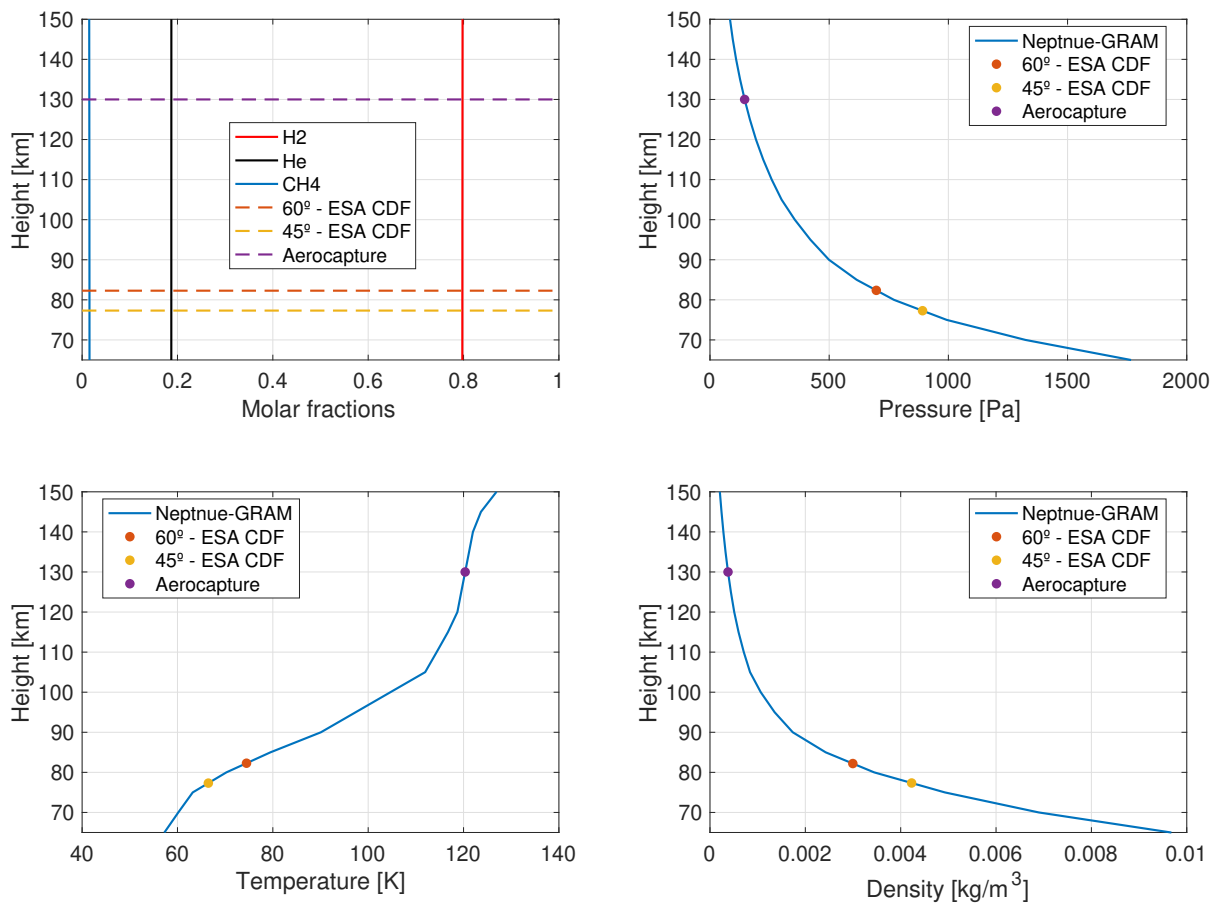
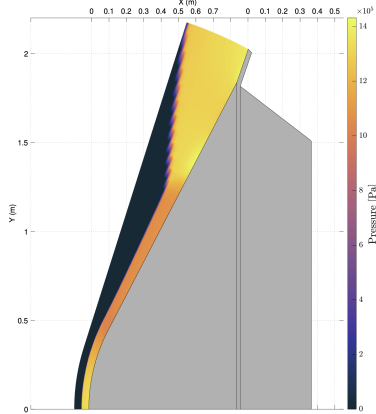


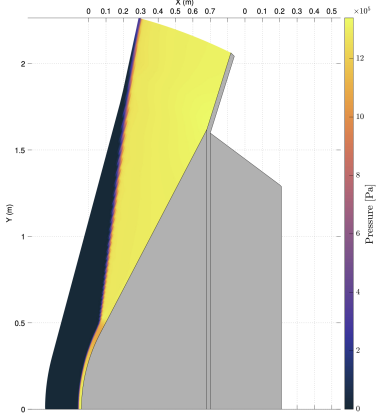
Figure C.1: Atmospheric properties from NASA's Neptune GRAM and equivalent points for entry trajectory point from ESA's CDF Study data as well as Aerocapture trajectory point.

Appendix D

Numerical Problems



(a) Cant angle test with shorter flap.

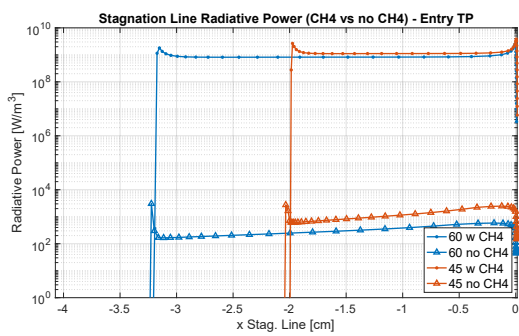


(b) Cant angle test with longer flap.

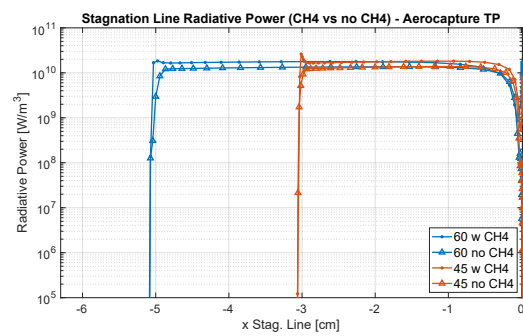
Figure D.1: Cant angle configurations with non physical solutions (Pressure field).

Appendix E

Results Aerothermodynamic Analysis

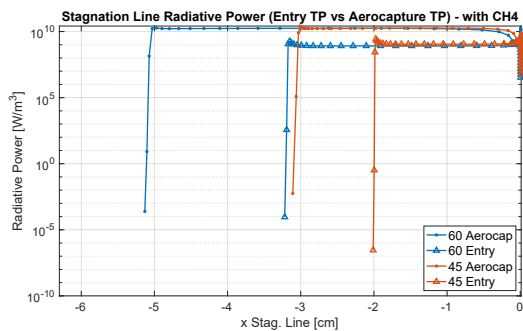


(a) Entry TP.

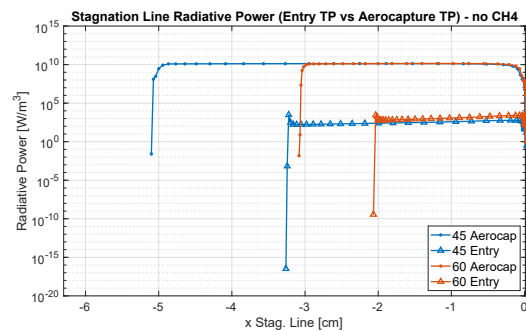


(b) Aerocapture TP.

Figure E.1: Total Radiative Power Comparison along Stagnation Line based on Chemical Composition.



(a) Composition A.



(b) Composition B.

Figure E.2: Total Radiative Power Comparison along Stagnation Line based on Trajectory Point.

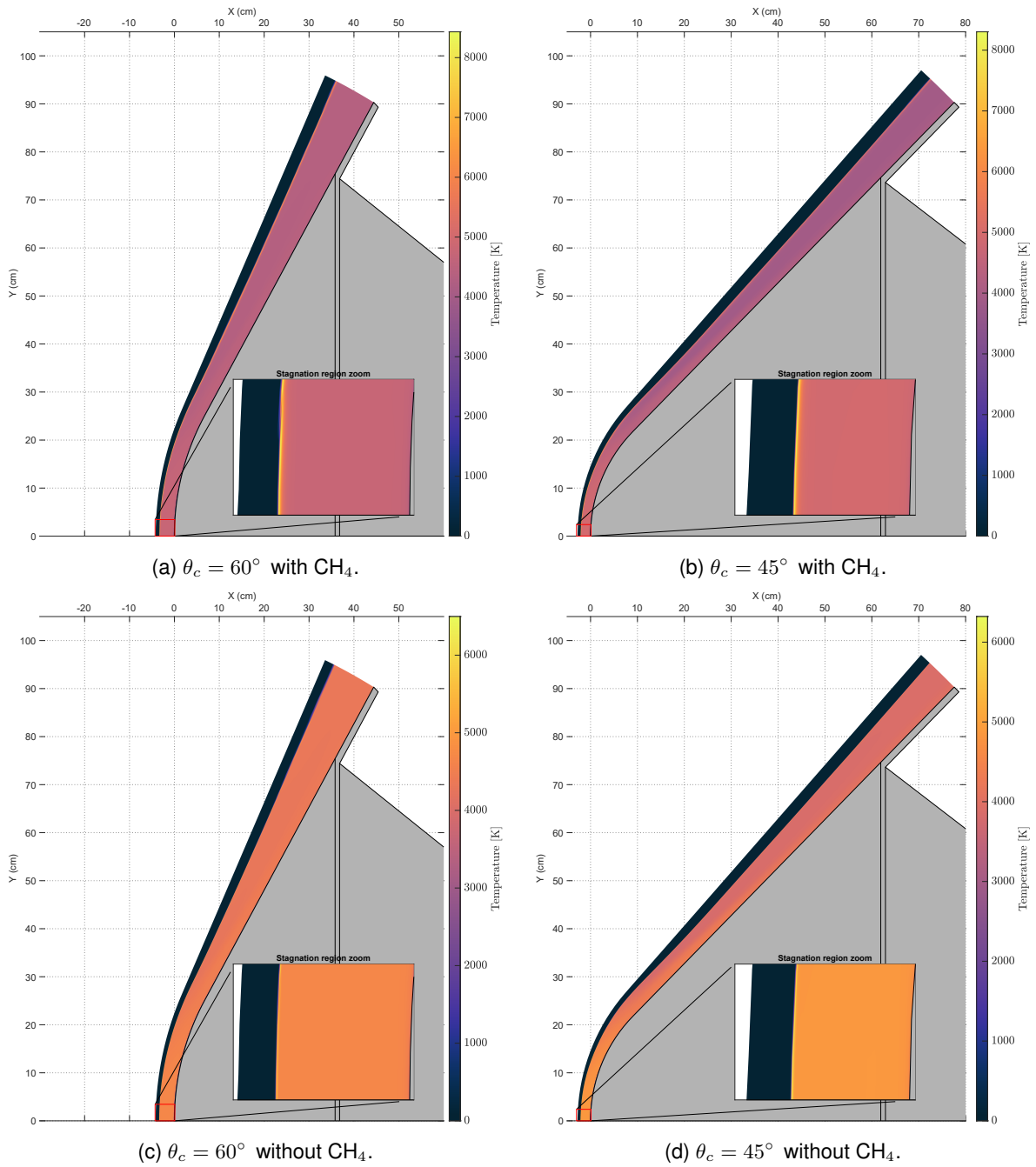
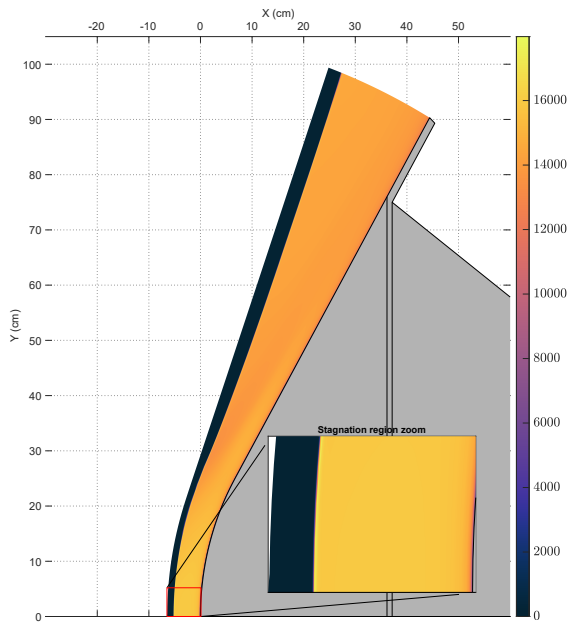
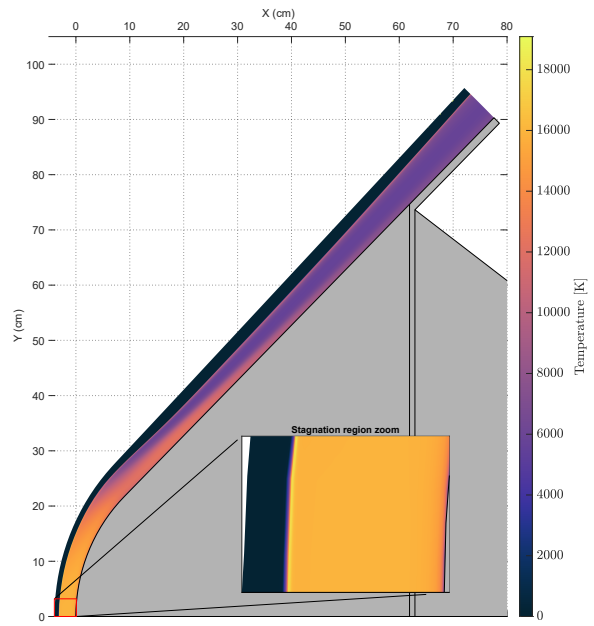


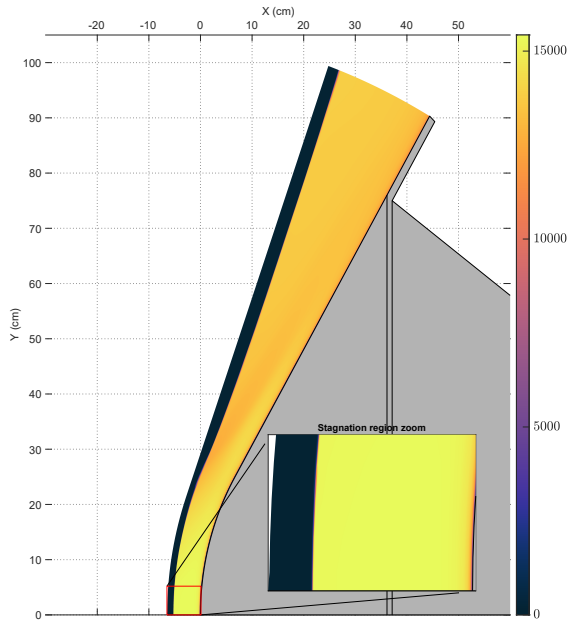
Figure E.3: Temperature fields for Entry TP.



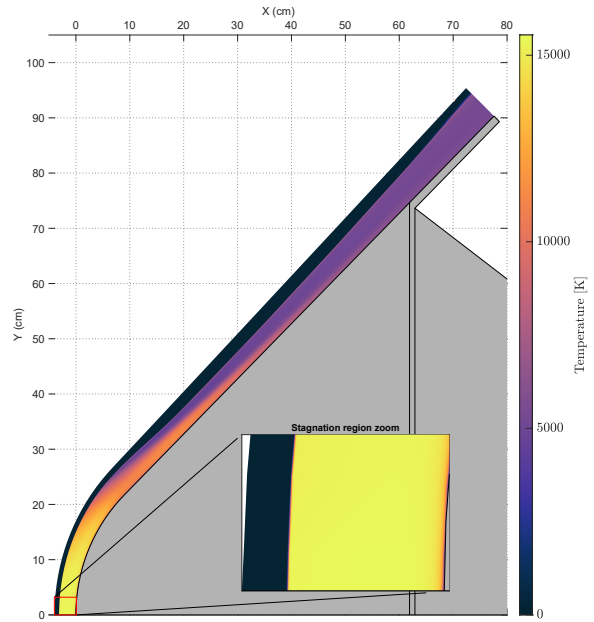
(a) $\theta_c = 60^\circ$ with CH_4 .



(b) $\theta_c = 45^\circ$ with CH_4 .

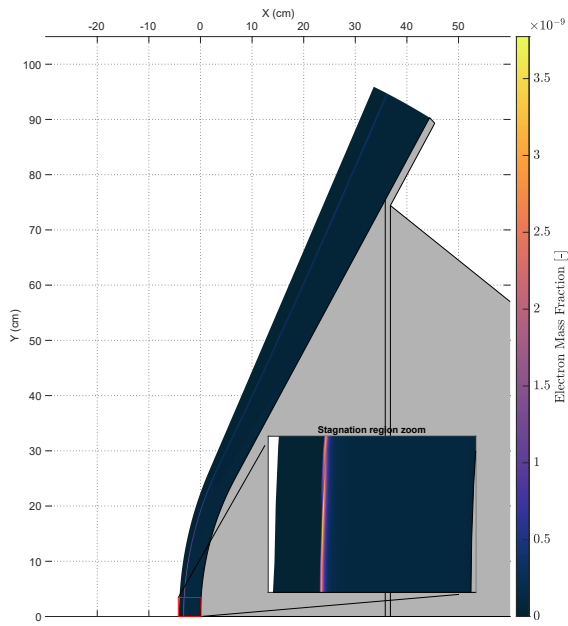


(c) $\theta_c = 60^\circ$ without CH_4 .

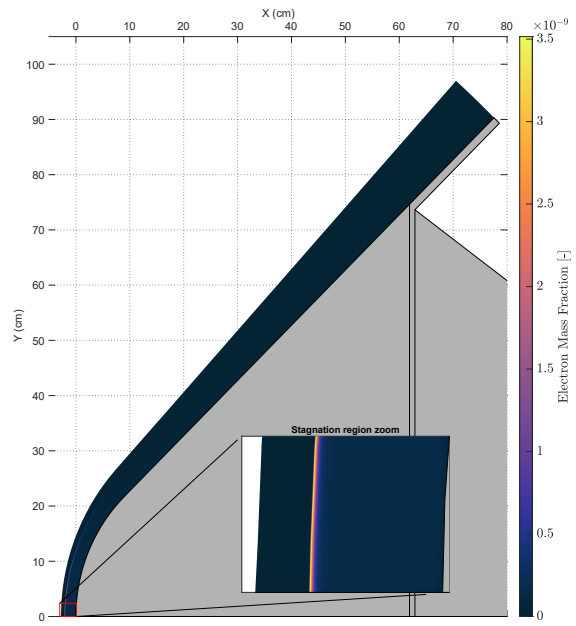


(d) $\theta_c = 45^\circ$ without CH_4 .

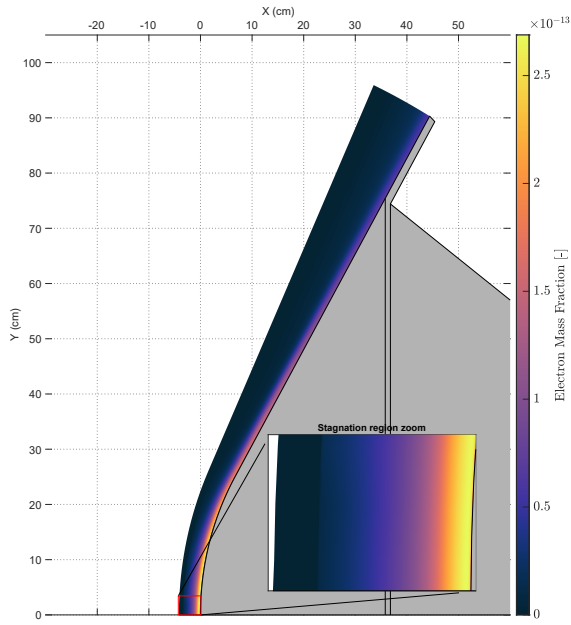
Figure E.4: Temperature fields for Aerocapture TP.



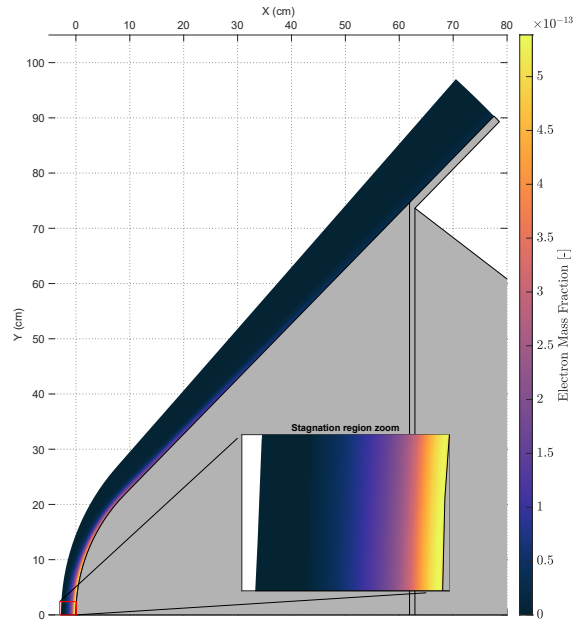
(a) $\theta_c = 60^\circ$ with CH_4 .



(b) $\theta_c = 45^\circ$ with CH_4 .

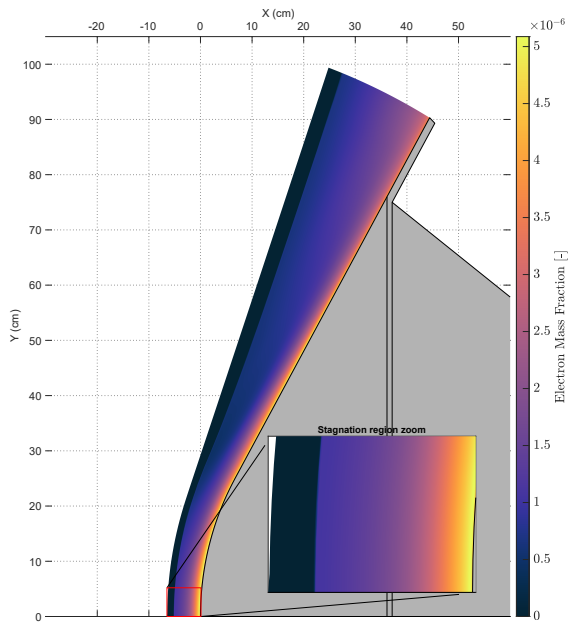


(c) $\theta_c = 60^\circ$ without CH_4 .

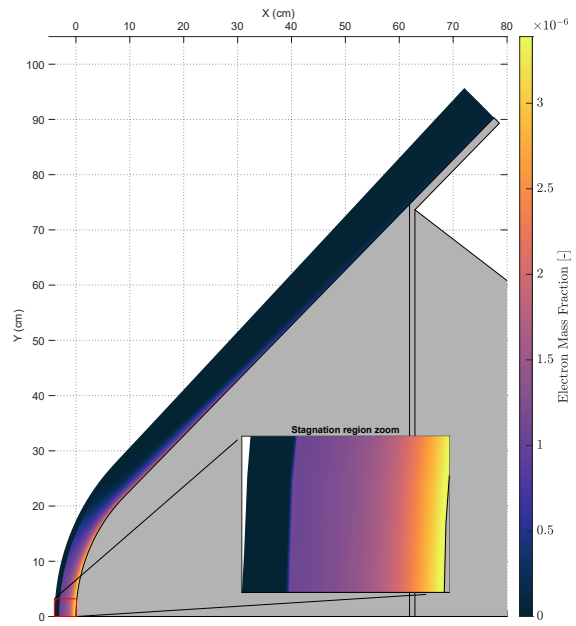


(d) $\theta_c = 45^\circ$ without CH_4 .

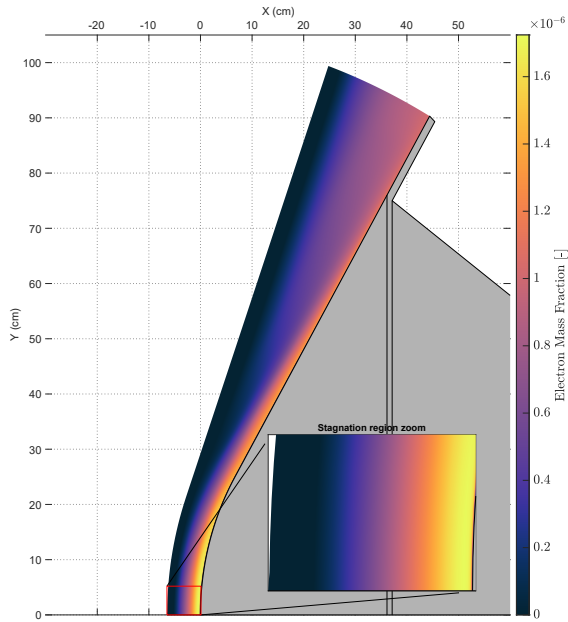
Figure E.5: Electron mass fraction fields for Entry TP.



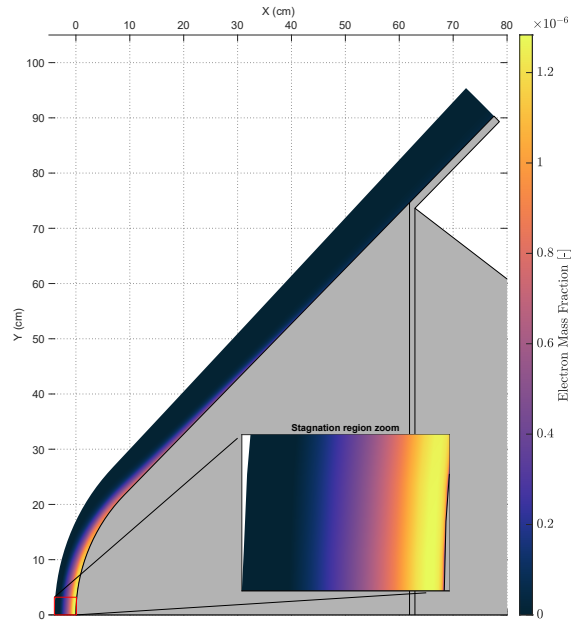
(a) $\theta_c = 60^\circ$ with CH_4 .



(b) $\theta_c = 45^\circ$ with CH_4 .

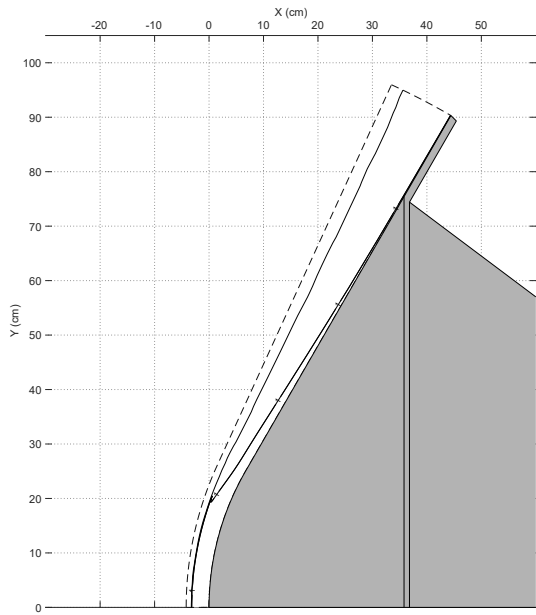


(c) $\theta_c = 60^\circ$ without CH_4 .

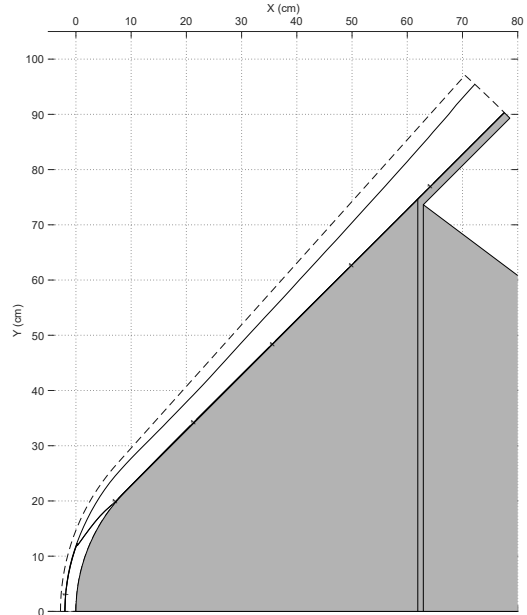


(d) $\theta_c = 45^\circ$ without CH_4 .

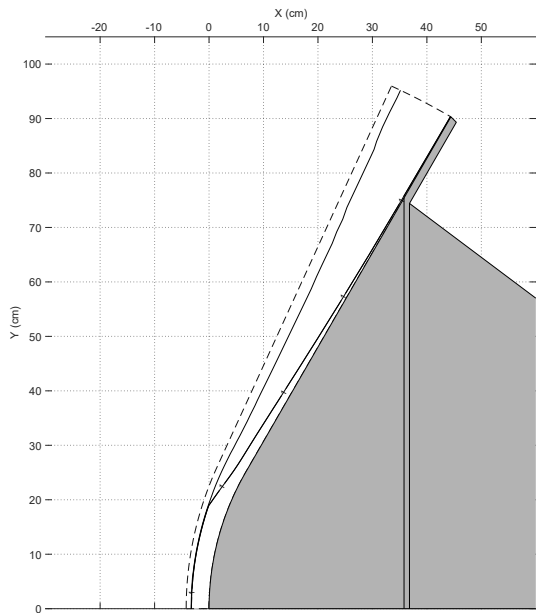
Figure E.6: Electron mass fraction fields for Aerocapture TP.



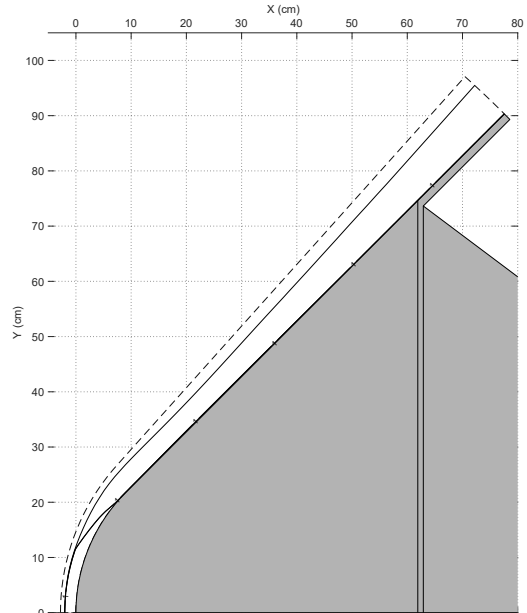
(a) $\theta_c = 60^\circ$ with CH_4 .



(b) $\theta_c = 45^\circ$ with CH_4 .

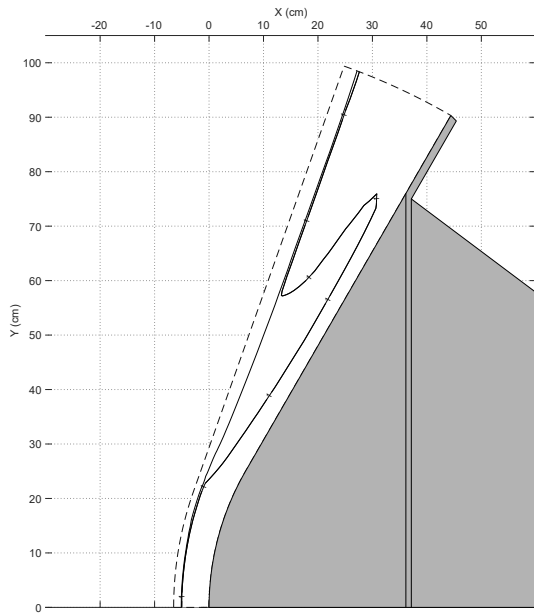


(c) $\theta_c = 60^\circ$ without CH_4 .

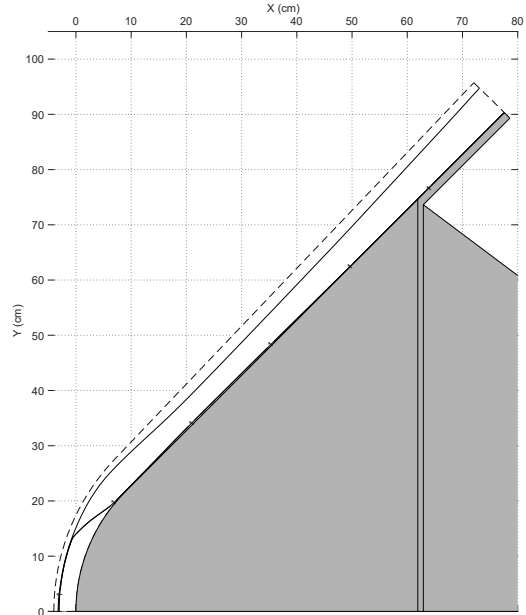


(d) $\theta_c = 45^\circ$ without CH_4 .

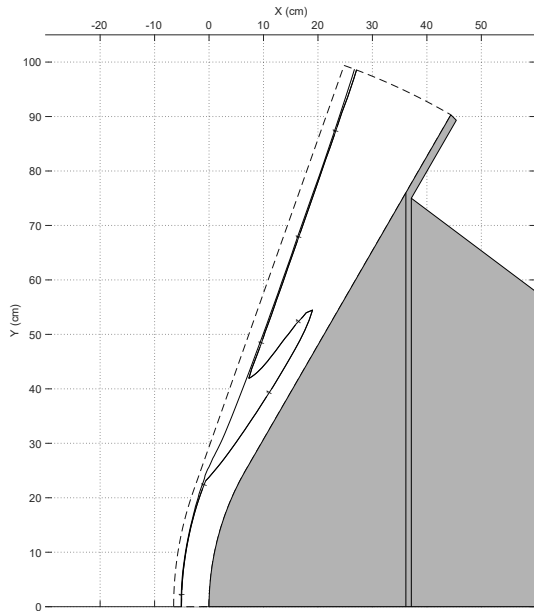
Figure E.7: Sonic Line for Entry TP.



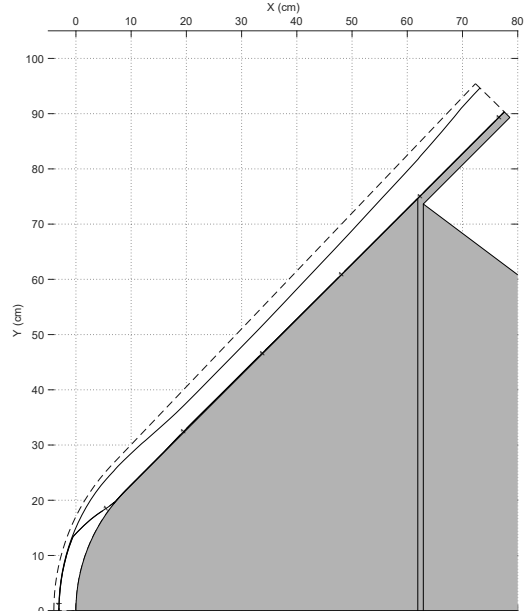
(a) $\theta_c = 60^\circ$ with CH_4 .



(b) $\theta_c = 45^\circ$ with CH_4 .



(c) $\theta_c = 60^\circ$ without CH_4 .



(d) $\theta_c = 45^\circ$ without CH_4 .

Figure E.8: Sonic Line for Aerocapture TP.

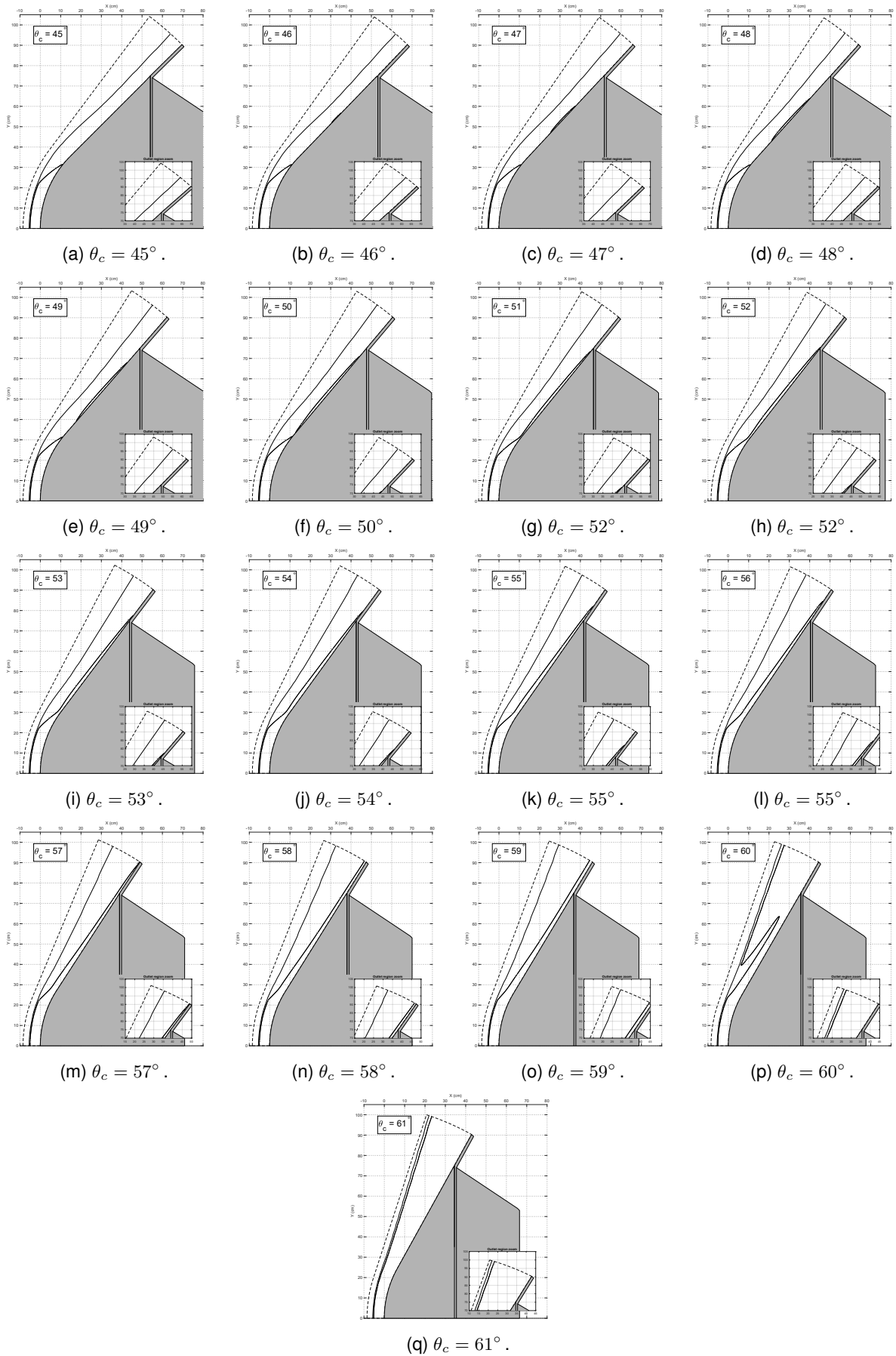


Figure E.9: Sonic Lines for Aerocapture TP Study from §4.4.2.2.

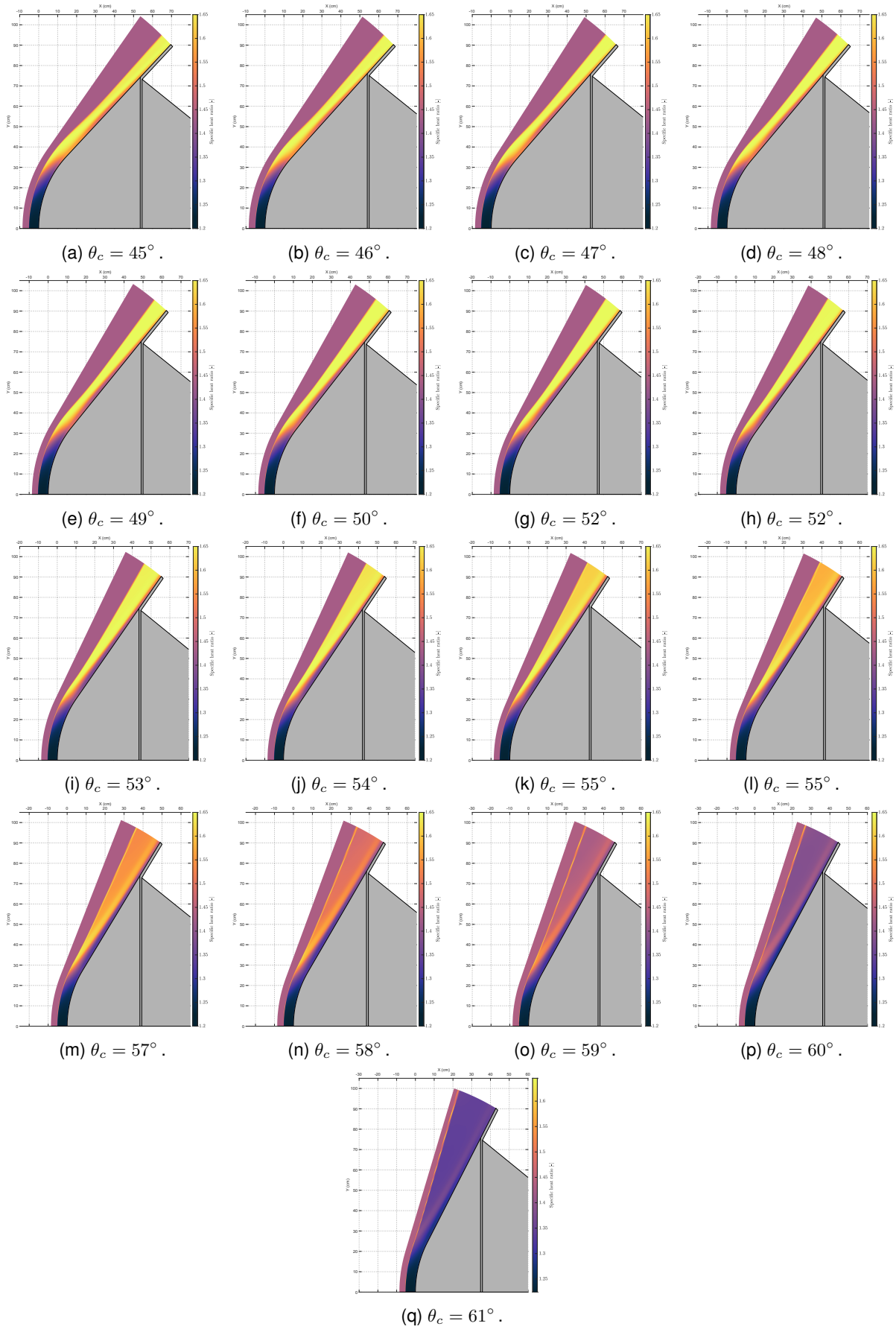


Figure E.10: Specific Heat Ratios for Aerocapture TP Study from §4.4.2.2.

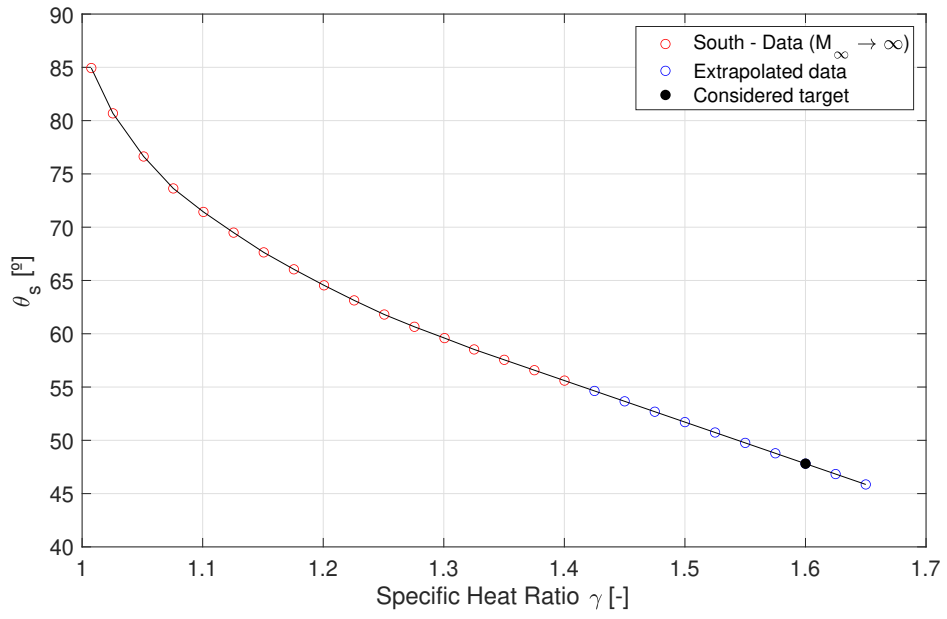


Figure E.11: Extrapolation values for θ_s from South [55].

